AN INVESTIGATION OF DISCONTINUOUS GLASS FIBER MANUFACTURING

by

Riccardo James Tresso

A thesis submitted to the Faculty and Board of Trustees of the Colorado School of Mines in partial fulfillment of the requirements for the degree of Doctor of Philosophy (Engineering Systems).

Golden, Colorado

Date April 2, 2001

Signed: Riccardo James Tresso

Riccardo James Tresso

Approved: David R. Munoz

Dr. David Munoz

Thesis Advisor

Golden, Colorado

Date April 2, 2001

Robert H King

Dr. Robert H. King

Department Head

Division of Engineering

ABSTRACT

The critical shear air/fiber interaction, which is the primary mechanism attributed to fiber attenuation within discontinuous rotary spinning processes, has been examined and characterized through detailed experimental drag force measurements and computational fluid dynamic model simulations.

The experimental measurements were performed using a piezoelectric force sensor which was designed, developed and implemented to measure the fluctuating drag force on a discrete glass microfiber within a well-characterized turbulent air flow. The novel force sensor possesses a fundamental frequency of 950 Hz with a resolution of approximately 10^{-4} N. The drag coefficient as a function of Reynolds number has been determined and is similar in form but differing in slope and intercept than that published for continuous fibers. Although the driving frequency of the turbulence was underestimated, which resulted in limited use of the sensor for fine scale forces, the sensor provided a necessary measurement of the average microfiber drag force.

The numerical portion of the research focused on the development of a computational fluid dynamic flow model which is capable of simulating the localized shear interaction between a molten glass filament and a high-speed air jet similar to that which occurs in industrial rotary spinning processes. The numerical model, Vi^3S-FLOW (Variable, Incompressible, Interface, Instability, Shear, Flow) is the first computational fluid dynamic model that enables industrial practitioners to examine on a micro-scale the air/glass interaction that is the primary mechanism attributed to fiber attenuation and formation. Vi^3S-FLOW is program for modeling transient, two-dimensional, incompressible, two fluid flows with density and viscosity ratios approaching 20:000:1 and 25:1, respectively. The volume-of-fluid code includes a piece-wise linear interface tracking algorithm, a robust continuum surface force model that includes harmonic averaging of the fluid viscosity, a 9-point stencil used by the incomplete Cholesky conjugate gradient method to solve the pressure Poisson equation and an energy equation model that incorporates conduction, convection and radiation heat transfer.

The development of the numerical model, Vi^3S-FLOW, along with experimental drag force measurements, represents the most comprehensive study into the shear air/fiber interaction completed to date. Vi^3S-FLOW used in conjunction with experimental results is a first step toward gaining the fundamental insight needed to obtain better control of fiber diameter and length during production. Thus, improving the quality and performance of discontinuous glass fibers produced from rotary spinning processes.

TABLE OF CONTENTS

Page

ABSTRACT iii

LIST OF FIGURES viii

LIST OF TABLES xii

ACKNOWLEDGEMENTS xiii

NOMENCLATURE xv

CHAPTER ONE INTRODUCTION 1

1.1 Rationale 4
1.2 Problem to be Solved 5
1.3 Objective 6

CHAPTER TWO BACKGROUND 8

CHAPTER THREE FORCE TRANSDUCER 19

3.1 Grid Generated Turbulence 19
3.2 Friction Drag Coefficient 22
3.3 Dynamic Force Sensor 24
3.4 Sensor Calibration 33
3.5 Data Reduction Procedure 38

CHAPTER FOUR EXPERIMENTAL RESULTS 41

CHAPTER FIVE NUMERICAL MODIFICATIONS 51

5.1 Interface Tracking Development 58

5.1.1 Piece-wise Constant Volume Tracking Method 61

Page

5.1.2 Fluid Volume Equations 63
5.1.3 PLIC Method of Solution....64
5.1.4 Reconstructing the Interface 66
5.1.5 Material Volume Fluxes 68
5.1.6 Time integration....73

5.2 Two Fluid Development 75

5.3 Continuum Surface Force Development....78

5.3.1 Viscous Stress Tensor Development 79
5.3.2 Smoothing Kernel Development....84

5.4 Pressure Poisson Equation Development....86
5.5 Energy Equation Development....96

CHAPTER SIX NUMERICAL RESULTS 108

6.1 PLIC Test Cases....108

6.1.1 Solid Body Rotation....109
6.1.2 Capillary Jet Break-Up 111

6.2 Rayleigh-Taylor Test Case 118
6.3 Pipe Flow Test Case 124
6.4 Static Droplet Test Case....127
6.5 Heat Transfer Test Cases 130

6.5.1 The Rectangular Plate....130
6.5.2 The Glass Fiber....132

6.6 Industrial Process Simulations....135

6.6.1 Industrial Process Test Case 140
6.6.2 Test Case A....145
6.6.3 Test Case B 151
6.6.4 Test Case C 154
6.6.5 Test Case D....157
6.6.6 Test Case E 160

Page

6.6.7 Test Case F....................163
6.6.8 Discussion of Results....................165

CHAPTER SEVEN CONCLUSION AND RECOMMENDATIONS....................169

7.1 Conclusions....................169
7.2 Suggestions for Future Research....................173

REFERENCES....................176

APPENDIX A THE NUMERICAL SCHEME....................183

A.1 Governing Equations....................184
A.2 Finite Difference Scheme....................187
A.3 Two Step Projection Method....................189
A.4 Time Integration....................191
A.5 Momentum Advection....................191
A.6 Viscous Stress Tensor....................192
A.7 Pressure Poisson Equation....................193
A.8 Free Surface....................194
A.9 Surface Tension....................195

APPENDIX B ERROR ANALYSIS....................201

B.1 Experimental Error....................201
B.2 Numerical Error....................202

APPENDIX C TWO FLUID PIPE FLOW TEST CASE....................206

LIST OF FIGURES

Figure Page

Figure 2.1 Wheel centrifugal spinning process....10

Figure 2.2 Air turbulence interaction....12

Figure 2.3 Rotary Spinning Process....13

Figure 3.1 Illustration of regions previously identified in grid generated turbulence....20

Figure 3.2 Principal velocity components....21

Figure 3.3 Force transducer development....26

Figure 3.4 Cross section of the 63-3018 NACA airfoil and sensor apparatus....27

Figure 3.5 SDOF Spring/Mass/Damper system....30

Figure 3.6 Piezoelectric film calibration....34

Figure 3.7 Piezoelectric Film Damping Coefficient....35

Figure 3.8 Force transducer frequency response curves....37

Figure 3.9 Force transducer phase response curves....38

Figure 4.1 Autocorrelation time scale determination....43

Figure 4.2 Driving frequency comparison....44

Figure 4.3 Amplitude correction factor....45

Figure 4.4 Glass and polymer fiber amplitude summary....46

Figure 4.5 Fiber drag force summary as a function of Reynolds number....47

Figure 4.6 Fiber drag force summary as a function a mean axial velocity....47

Page

Figure 4.7 Friction drag coefficient summary 49

Figure 4.8 Friction drag coefficient condensation summary 49

Figure 5.1 Rotary spinner critical zone cross section 52

Figure 5.2 Extrusion of a molten glass filament 56

Figure 5.3 Geometric toolbox representation 66

Figure 5.4 Face volume fluxes 69

Figure 5.5 Split material volume flux 71

Figure 5.6 Split material volume flux corner correction 72

Figure 5.7 Harmonic average for the cell edge (i+1/2, j+1/2) on a standard computational mesh 81

Figure 5.8 CSF Smoothing Kernal 85

Figure 5.9 Computational pressure cell template 90

Figure 5.10 Temperature dependent dynamic viscosity 98

Figure 5.11 Hypothetical temperature contour 100

Figure 5.12 Infinite cylinder axial temperature profile approximation 101

Figure 6.1 PLIC Test Case 110

Figure 6.2 Capillary jet break-up 112

Figure 6.3 PLIC vs. SLIC comparison 114

Figure 6.4 PLIC vs. SLIC comparison summary 117

Page

Figure 6.5 Rayleigh-Taylor Instability 119

Figure 6.6 Rayleigh-Taylor Instability Test Case....................122

Figure 6.7 Theoretical vs. numerical instability growth rate comparison 123

Figure 6.8 Two fluid pipe flow free-slip boundary test case....................125

Figure 6.9 Two-fluid, variable viscosity static droplet test 128

Figure 6.10 Growth of TKE versus time for a static droplet....................129

Figure 6.11 Johnson (2001) analytical and numerical nickel plate temperature contour test case results 132

Figure 6.12 Glass fiber test case boundary and initial conditions 134

Figure 6.13 Glass fiber thermal test case results....................135

Figure 6.14 Rotary spinning process 136

Figure 6.15 Air/glass simulation input boundary conditions....................139

Figure 6.16 Temperature dependent glass kinematic viscosity 140

Figure 6.17 Kelvin-Helmholtz instability....................143

Figure 6.18 Industrial Process air/glass simulation results....................145

Figure 6.19 Test Case A air/glass simulation results....................148

Figure 6.20 Test Case A air/glass temperature contour....................151

Figure 6.21 Test Case B air/glass simulation results 153

Figure 6.22 Test Case C air/glass simulation results 155

Figure 6.23 Test Case D air/glass simulation results....................160

Page

Figure 6.24 Test Case E air/glass simulation results 163

Figure 6.25 Test Case F air/glass simulation results...165

Figure A.1 Force Balance about fluid interface element (dA).......................................185

Figure A.2 RIPPLE computational mesh for cell (i,j) and (i+1,j) 188

Figure A.3 Transition region between fluids c1 and c2..197

Figure A.4 Determination of the body force derived from the surface curvature (κ)......199

Figure C.1 Illustration of the variable viscosity pipe flow test case...............................208

Figure C.2 Analytical vs. numerical velocity profiles..209

Figure C.3 Two fluid velocity profile results...212

Figure C.4 Two fluid pipe flow mass flowrate summary..213

Figure C.5 One fluid pipe flow test case velocity profile comparison 214

LIST OF TABLES

Table Page

Table 2.1. Experimental Air Drag Characteristic Summary 16

Table 3.1 Piezoelectric Force Sensor Critical Dimensions 25

Table 3.2. Piezoelectric Film Stiffness Calibration 35

Table 6.1. Capillary Jet Break up and Run Time Summary 115

Table 6.2. Satellite Size Comparison Summary 116

Table 6.3 Industrial Process Input Parameters 142

Table 6.4 Test Case A Input Parameters 146

Table 6.5 Test Case B Input Parameters 152

Table 6.6 Test Case C Input Parameters 154

Table 6.7 Test Case D Input Parameters 159

Table 6.8 Test Case E Input Parameters 162

Table 6.9 Test Case F Input Parameters 164

Table B.1. Uncertainty Analysis Parameters 201

ACKNOWLEDGEMENTS

The author wishes to express his appreciation to the following committee members.

Dr. David Munoz, for his encouragement, support and mentoring throughout my graduate career.

Dr. Jean-Pierre Delplanque, for his extraordinary insight into the field of computational fluid dynamics.

Dr. Gene Woolsey, for showing me that life is often ruled by perception and not necessarily by truth.

Dr. Ivar Reimanis, for his guidance and tutelage.

Dr. Ronald Miller, for his guidance and support.

The author would also like to thank...

National Science Foundation on contract DMI-9634828 for supporting the research.

Dr. Joan Gosink, for providing the National Science Foundation Traineeship Award that made it possible to continue the project research as well as my education.

Dr. Douglas Kothe, for his enthusiasm, encouragement and guidance throughout the numerical development.

Los Alamos National Laboratory, for providing the software and support that made a large portion of this research possible.

Johns Manville for critical input data, research suggestions and monetary support.

Dedicated to my family, specifically…

my Mother and Father. Thank you for always supporting me as I pursued my goals,
without you I never would have made it this far. Thank you
for teaching me to reach for the stars.

my Grandmother. Thank you for giving me a perfect childhood and a foundation
to build upon. I will cherish those memories forever.

my Aunts. Thank you for the support, encouragement and prayer.

Katie. Thank you for seeing beyond my shortcomings, for showing me the true meaning
of courage and the will to overcome tremendous obstacles.
Thank you for making me a better person.

NOMENCLATURE

A -------------- displacement amplitude (m)

A_s -------------- surface area (m^2)

A_t -------------- Atwood number (dimensionless)

C_p -------------- specific heat (J/kg-K)

C_f ------------- friction drag coefficient (dimensionless)

C --------------- damping factor (dimensionless)

d --------------- fiber diameter (μm)

F ----------------force (N)

F_d -------------- drag force (N)

F_o ------------- force amplitude (N)

f(t) ------------ external forcing function

h --------------- enthalpy per unit volume (J/m^3), film coefficient (W/m^2-K), smoothing length (meter)

I-----------------instability parameter (dimensionless)

i --------------- computational index (dimensionless)

J ----------------Jacobian

j --------------- computational index (dimensionless)

K -------------- stiffness (N/m)

k -------------- material indicator (dimensionless), thermal conductivity (J/m-s-K)

k -------------- coefficient (dimensionless)

L ------------- fiber length (m), latent heat (J/kg)

L_{grid} ---------- characteristic grid length scale (m)

L_t ------------- turbulent length scale (meters)

M ------------- geometric coefficient matrix (dimensionless)

m ------------- mass (kg), experimental constant (dimensionless), slope (dimensionless)

mg ----------- gravitational force (N)

Nu ----------- Nusselt number (dimensionless)

n -------------- exponential coefficient (dimensionless)

n -------------- normal line vector (dimensionless)

p -------------- pressure (Pa)

q -------------- heat flux (W/m^2)

R ------------- autocorrelation coefficient (dimensionless)

Re_{Mu} ---------- Reynolds number based on meshlength (dimensionless)

Re_{Dh} ---------- Reynolds number based on hydraulic diameter (dimensionless)

Re_d ----------- Reynolds number based on fiber diameter (dimensionless)

r -------------- number of cycles (dimensionless)

T ------------- temperature (K)

T_{air} ----------- air temperature (K)

T_{glass} ---------- glass temperature (K)

T_{in} ------------- inlet temperature (K)

T_{out} ----------- outlet temperature (K)

T_m ------------- melt temperature (K)

T_s ------------- surface temperature (K)

T_{surr} ---------- surrounding temperature (K)

T_t -------------- characteristic time scale (sec)

t --------------- time (sec)

U, V, W------- air mean velocities (m/sec)

u', v', w' ------ air fluctuating velocities (m/sec)

V -------------- volume (m^3)

x/Mu ---------- meshlength (dimensionless)

x --------------- principal direction of motion

x, y ------------ Cartesian coordinates

α -------------- geometric coefficient, thermal diffusivity (m^2/sec)

α_k ------------- indicator function (dimensionless)

β -------------- geometric coefficient

δ --------------- velocity boundary layer thickness(m)

ε --------------- emissivity (dimensionless), dissipation of turbulent kinetic energy (cm^2/sec^3), volume-of-fluid error term (dimensionless)

γ --------------- geometric coefficient

η --------------- boundary layer depth ratio (dimensionless)

κ --------------- interface curvature (meter^{-1})

ϕ_o -------------- phase angle (degrees)

ζ --------------- damping coefficient (dimensionless)

μ -------------- dynamic viscosity (N-sec/m^2)

ν -------------- kinematic viscosity ($\text{m}^2\text{/sec}$)

ρ --------------- air density (kg/m^3), autocorrelation coefficient function ($\text{sec}^2\text{/m}^2$)
line constant (dimensionless)

σ --------------- standard deviation of the fluctuating velocity components (m/sec), surface tension coefficient (N/m), Stefan-Boltzmann constant ($\text{W/m}^2\text{-K}^4$)

τ --------------- time lag (sec), shear stress (Pa)

ω -------------- frequency (Hz)

ω_n ------------- natural frequency (Hz)

Δt ------------- time increment (seconds)

δV ------------- material volume flux (m)

CHAPTER ONE

INTRODUCTION

Rapid growth and recent technological advances throughout the fiber industry have brought about the need for developing an intimate understanding of the physical phenomenon involved in the process of discontinuous fiber spinning. Companies that produce thermal insulation, made from discontinuous glass fibers, for automobiles, aircraft, residential and commercial buildings, are continually striving to improve the thermal characteristics of their products by utilizing microfibers, which provide improved thermal conductivity. The need for small fibers is becoming more widespread and has renewed interest in improving control of fiber diameter and length during production. Currently, discontinuous fibers are being produced from years of empirical knowledge and experience, with a limited understanding of the mechanisms attributed to fiber attenuation and formation. In the process of discontinuous fiber manufacturing, turbulent air and combustion products are used to attenuate the fiber while in its molten state, thereby contributing to the control of fiber diameter and length. One critical aspect of fiber spinning that is believed to play a significant role in fiber attenuation and formation is the air/fiber interaction that occurs during fiberization (Steve Gross, 1997). Analyzing and characterizing the critical air/fiber interaction forms the basis of the research presented herein.

Current research is focusing on the many complex issues of discontinuous fiber manufacturing. However, few researchers have examined fiber dynamics during formation, including air turbulence interactions, believed to play a critical role in achieving specific fiber diameter and length. Fibers that are smaller than 3μm in diameter and approximately 200μm in length that are inhaled deeply into the lung cannot be dislodged and cleaned by natural processes (Silverman *et. al.*, 1971). Small diameter fibers in service that fracture and become airborne may represent a potential health problem for maintenance workers (DuPont and Morrill, 1989). However, small diameter (>10μm) fibers result in improved thermal insulation characteristics (Pelanne *et al.*, 1981). Therefore, fiber manufacturers are extremely interested in controlling fiber diameter and length in industrial fiberization processes, not only to address health concerns, but also to improve the performance of the fibers produced.

Mixing conditions within the industrial fiberizing process can be emulated by implementing grid generated turbulence (GGT), within a laboratory wind tunnel. Previous GGT studies within low speed laboratory wind tunnels provide the basis to experimentally investigate the air/fiber interaction, or more specifically the effect of air drag on fiber formation (Mohamed and LaRue, 1990, and Tresso and Munoz 2000). A dynamic force transducer (see Section 3.3) was positioned within the wind tunnel test section, that measured drag force fluctuations on discontinuous glass and polymer fibers.

The fluctuating drag force data provided the basis to accurately determine friction drag coefficients for various turbulent flow conditions and fiber sizes.

Unlike past research that examined drag coefficients experimentally or theoretically during and/or for the continuous fiber spinning process (Sakiadis, 1961, Matsui, 1976 and Shimizu and Okui, 1983), presented herein is the fiber friction drag coefficient for a discrete fiber within a well-controlled laboratory wind tunnel. The fiber fluctuations were recorded using a specially-designed piezoelectric force sensor. The dynamic response of the fiber was examined through the use of high-speed video to determine its fundamental frequency and subsequent vibration modes. The measured dynamic fiber tensile force was integrated into the calculation of fluctuating drag force and the determination of a friction drag coefficient. The drag coefficient relationship of equation 1.1 provides the basis of the experimental study.

$$C_f = k\,\mathrm{Re}_d^{-n} \tag{1.1}$$

In addition to the experimental investigation, a "localized" numerical simulation of fiber attenuation and necking has been completed. RIPPLE, a free surface volume-of-fluid (VOF) code developed by Los Alamos National Laboratory to simulate two-dimensional, free surface flows in a micro-gravity environment, was modified to simulate the critical interactions of discontinuous fiber manufacturing. The numerical approach provides a critical micro-scale insight into the formation of discontinuous glass fibers, which to date has not been successfully completed.

1.1 Rationale

The rapid growth of the fiber industry in recent years has brought about the need for developing a deeper understanding of the physical phenomenon involved in the process of discontinuous fiber spinning. Presently, most discontinuous fibers are being manufactured on the basis of empirical experience and knowledge (Ziabicki, 1976). However, recent technological advances in the materials industry have occurred because of the need for increased fiber quality. Consequently, an improved understanding of the fundamental air/fiber interaction during fiberization is required to further improve the quality and quantity of fiber produced.

Progress is being made with an attempt to systematically analyze various interactions occurring during fiberization. One such phenomenon, which is believed to play a critical role in discontinuous fiber formation, is the interaction between turbulent air flow and the glass fiber during formation. It is believed this fundamental interaction causes the fiber to attenuate thereby affecting fiber length and diameter. The goal of the research was to address the fundamental problem of characterizing the air/fiber interaction through experimental drag force measurements and numerical model simulations.

An attempt has been made to exhaustively research all published work in this area. The findings are extremely limited. There has been little or no previously published work in this area, or at least none available to the general public. As a result, there has been no known experimental or numerical research conducted to examine the effects of aerodynamic drag on fiber formation.

1.2 Problem to be Solved

In most discontinuous fiber manufacturing processes, air, combustion products or both are used to attenuate the fiber while in its molten state, thereby contributing to the control of fiber diameter and length. To date there is not a complete understanding of the gas/fiber interaction and no known studies have been completed in industrial pilot plant environments to better characterize the air/fiber interaction. This study focuses on providing an improved understanding of fundamental air/fiber characteristics through carefully designed wind tunnel experiments and numerical simulations modeled from the industrial process.

The fiberizing process has been well established for many years producing products in various industries, however there is little or no background to the basic fundamental understanding of fiber production at the intimate level of fiber interaction with the surrounding turbulent air flow. The goal of the research presented herein was to develop a well-defined study, comprised of a set of experiments, conducted in a well-characterized turbulent airflow integrated with a numerical simulation to achieve an improved understanding of the flow phenomenon and fiber attenuation within the industrial process. This study represents the first step toward investigating the air/fiber interaction during discontinuous fiberization.

1.3 Objective

The air/fiber interaction, which occurs during discontinuous fiber manufacturing, must be well understood before control of fiber length and diameter can be improved and optimized. A specially designed force transducer placed within a well-characterized flow region has enabled fiber fluctuating tensile force measurements to be recorded for various fiber aspect ratios and turbulent flow conditions. Using the experimental force measurements, drag coefficients for a discrete fiber have been determined and compared to published results. Drag force is an important, but little understood component of fiber spinning. The drag coefficients developed from measurements taken in an environment similar to that of an industrial rotary spinner will ensure the validity and accuracy of drag force coefficients used in numerical models.

Until recently there has been little effort to fully model, using a computational fluid dynamic (CFD) approach, the process of discontinuous fiber spinning. Most of the research conducted has focused on continuous filament spinning. Certain effort has been devoted to applying commercially available CFD computer codes to validate experimental measurements, in addition to estimating process limitations. Accurately combining critical process parameters such as melt temperature, air temperature, melt viscosity, air speed and process geometries has not been successfully integrated into a complete model due to the complexity of the spinning process and computational limitations. Simplified, one fluid, two-dimensional models have been developed to examine fiber stretching, however controlling fiber diameter and length requires a more precise understanding of a multidimensional, two-phase fluid/thermal flow model that incorporates the air/fiber interaction. Commercially available software packages that include two-phase flow models use particles to track fluid motion, but the particles do not represent a continuous phase, which is needed to accurately simulate shear air/fiber interaction critical to fiber formation.

In summary the objectives of the research are listed below.

1. Design and development of a dynamic force transducer capable of measuring the fluctuating tensile force on a single glass fiber placed within a well-characterized turbulent flow field representative of industrial rotary spinning processes.
2. Develop experimental drag force coefficients for various fiber lengths, diameters and flow conditions.
3. Provide a numerical tool to analyze critical process interactions.
4. Provide a numerical tool that will be used to predict "localized" fiber attenuation.
5. Initiate the development of a complete and comprehensive fiberizing model that may be used as a versatile CFD code to build and expand upon.

CHAPTER TWO

BACKGROUND

Ross and Klingenberg (1997) developed a particle-level simulation to examine the dynamics of flowing suspensions of rigid and flexible fibers. The discrete fibers are modeled as chains of spheroids connected through ball and socket joints. By varying the resistance of the joints, both flexible and rigid fibers may be dynamically modeled, however the fluid/fiber interaction was disregarded. Skjetne *et. al.* (1997) also modeled fiber motion using a series of rigid spheres connected by ball joints. Both spheroid models simulate a discrete fiber tumbling end over end through space, unlike the fiber formation zone of the rotary spinning process where molten filaments are extruded through small holes of a spinning disk. The filaments likely move with one end fixed to the spinning disk until the tensile force exceeds the attachment strength at which point the fibers break free from the spinning disk.

The phenomenon of nonlinear waves in an absolutely flexible fiber has been examined by Ridel and Il'gamov (1997). The researchers studied longitudinal oscillations of a previously extended, viscoelastic fiber whose one end is immovable and the other is free to vibrate along the fiber by a harmonic forcing function. Modeling a discontinuous fiber, Burget and Advani (1994) studied fiber motion near a solid boundary but the flows were creeping ($Re << 0.05$, based on the fiber diameter), simulating conditions between the flowing epoxy and fiber matrix during composite material manufacturing. Wu and Shambaugh (1992) used a laser doppler velocimeter (LDV) to measure the velocity, diameter and orientation of polypropylene fibers formed using a continuous melt blown process. Information from this study was used to estimate the fiber mass flux and orientation, however no attempts were made to understand the importance of the air turbulence interacting with the fiber during formation. Ziabicki *et. al.* (1998) examined the dynamics of continuous melt spinning to determine the essential effects in modeling of the process. The researchers developed dynamic formulations of the melt spinning process including viscoelastic effects, crystallization, heat production and deformation, however again no attempts were made to investigate the air turbulence interaction.

Additional research in the area of discontinuous fiber manufacturing has examined dynamic bifurcations of the ring-spinning balloon (Stump and Fraser, 1995), one dimensional isothermal spinning models for liquid crystalline polymer fibers (Forest *et. al.*, 1997) and modeling continuous and discrete systems of the spinning process (Akatsuka and Furumatsu, 1996). However, all research was based on a single die, yarn-spinning device and take-up reel that is unlike the process encountered in this study. Past research in similar areas has consisted of modeling fiber formation during the centrifugal fiber spinning process. The main focus of this work was the prediction of fiber diameter, length and production rate knowing the surface tension and viscosity of glycerin used to experimentally model industrial flows of molten glass as it was thrown from the circumference of a spinning disk, shown in Figure 2.1.

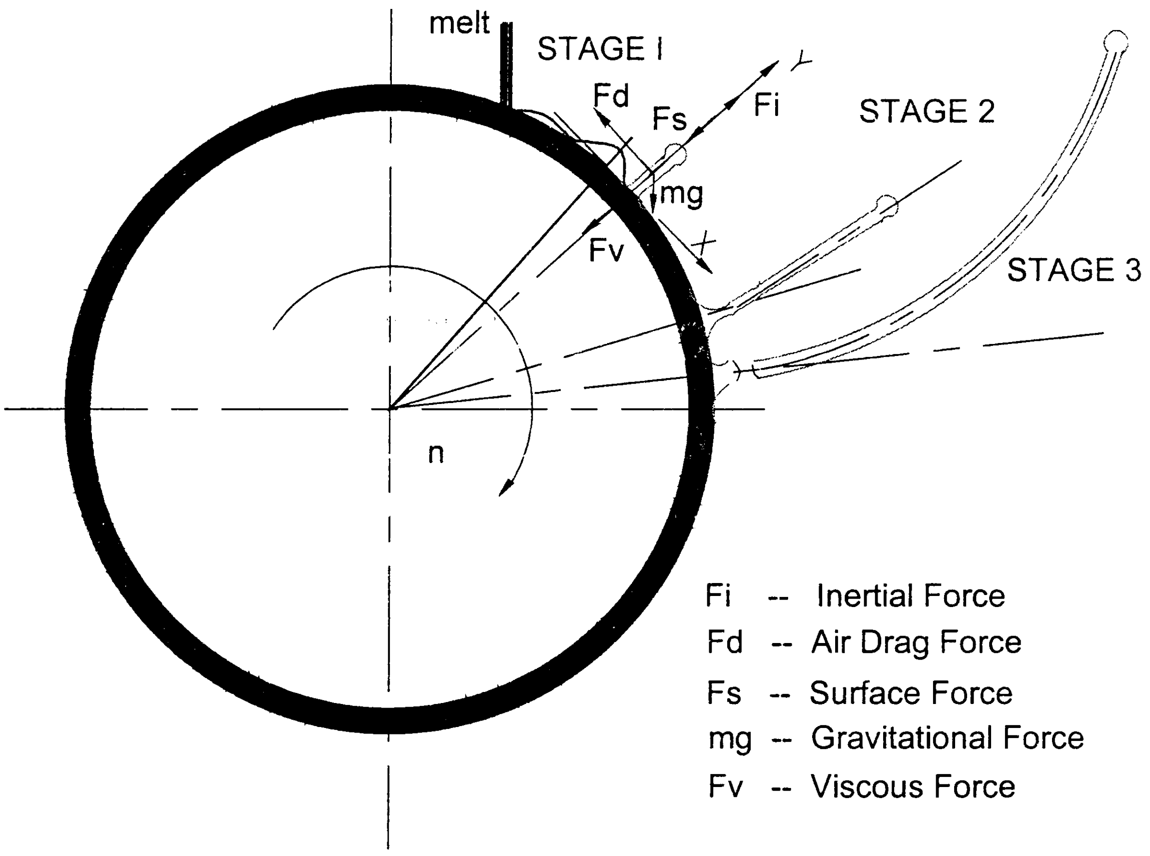

Figure 2.1. Wheel centrifugal spinning process.

Considering the amount of research completed in this area (Cai, 1994, Burget, 1994, Ziabicki, 1991) there is no known previous work reporting on examination of the air/fiber interaction during fiberization, however previous research does provide a basis for further experiments into the discontinuous fiberizing process. The studies of modeling fiber formation by the centrifugal spinning process indicated good predictability of fiber diameter and length within the range of parameters studied (Cai *et. al.* 1994). However, the data began to scatter as Reynolds number increased toward that of the industrial process, or as the effects of turbulence increased. Thus, it is imperative that the effects of air turbulence within the fiberization process are well understood before control of fiber diameter and length can be optimized. In fact, air/fiber interaction may be necessary to properly achieve the required attenuation of the fiber during fiberization processes (Johns Manville, 1997). It can only be speculated which fiber properties or process parameters are affected by the air/fiber interaction during discontinuous fiber manufacturing. An approximation of the effect on air/fiber interaction is shown in Figure 2.2.

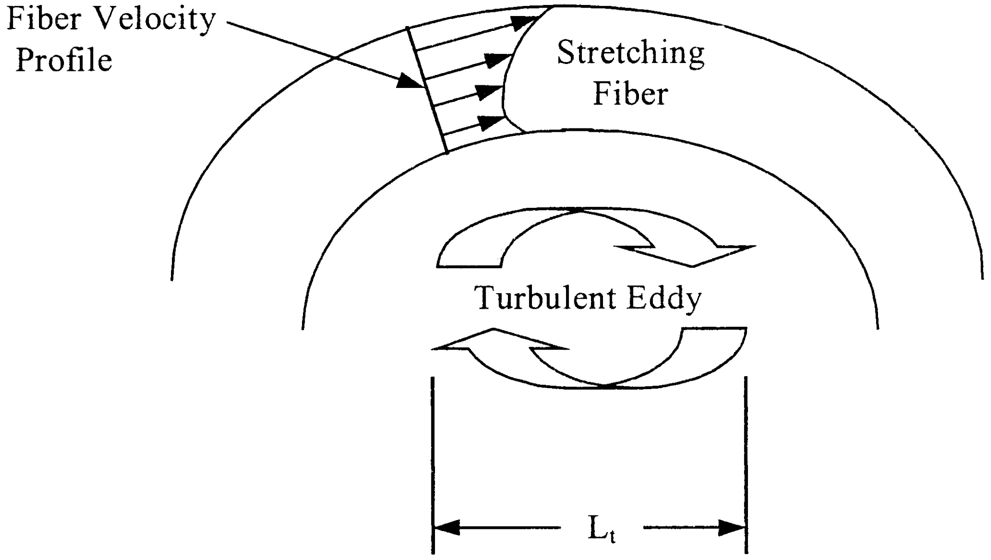

Figure 2.2. Air turbulence interaction

A rotary spinning process, to produce glass and polymer fiber, similar to that shown in Figure 2.3, utilizes a spinning basket with hundreds of small holes around its perimeter. Molten glass/polymer is poured into the top of the basket, spinning about a vertical axis, and relatively thick streams of the glass/polymer flow out of the holes. An array of high-velocity, downward-directed air jets form an annular flow and interaction with the molten glass/polymer streams redirecting them onto a moving conveyer below. Because of the centrifugal acceleration of the disk and the momentum imparted to the fiber from the air jets, the fiber stretches and the diameter thins to several microns. Within this region the flow of air exiting the jets is turbulent and there is a substantial shear air/fiber interaction with the forming fiber. The streams also rapidly solidify into solid fibers within this region and are collected below on the moving conveyer and packaged. It is speculated that this air/fiber interaction is necessary to achieve proper stretching and attenuation of fiber. However, little is known of the direct effects of the high-speed air jet characteristics on fiber formation and there is a timely need to improve the fundamental understanding for purposes of manufacturing system optimization (Cai *et al.*, 1994).

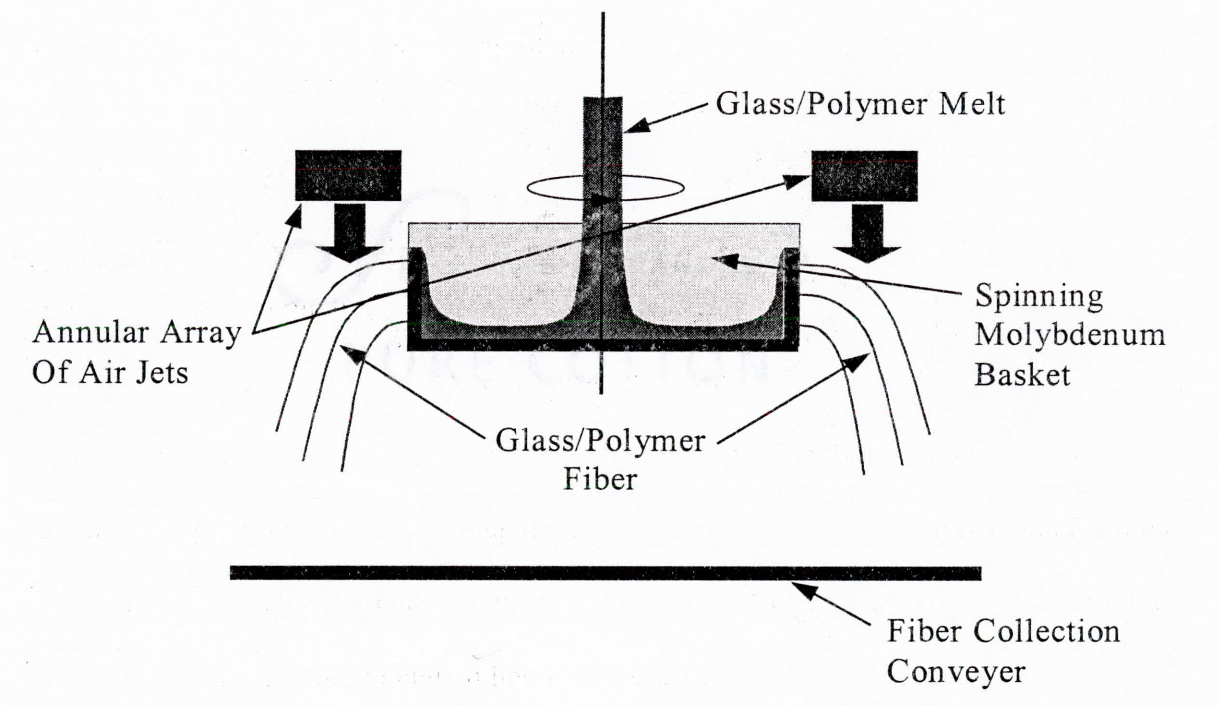

Figure 2.3. Rotary Spinning Process

A critical portion of the research presented herein includes a detailed analysis of GGT (grid generated turbulence). Grid generated turbulence provides a means to match turbulent flow characteristics of the industrial process within a well-controlled laboratory environment. Tresso (1998), Tresso and Munoz (2000) and Mohamed and LaRue (1990) have developed criteria to identify the nearly homogeneous, isotropic flow conditions downstream of a square grid. These criteria included analysis of one-dimensional velocity skewness, three-dimensional cross moments and turbulent kinetic energy dissipation rates for a moderate range of Reynolds numbers (based on grid spacing) between 5,000 and 30,000.

Kistler and Vrebalovich (1965) also studied grid generated turbulence at much higher Reynolds numbers near 2,400,000. Additional studies by Comte-Bellot and Corrsin (1965) examined the effects of contraction to improve the isotropy of grid generated turbulence by equilibrating the average kinetic energies.

Unlike past research that examined drag coefficients experimentally or theoretically for the continuous fiber spinning process (Sakiadis, 1961, Matsui, 1976 and Shimizu and Okui, 1983), presented herein is the fiber friction drag coefficient for a discrete fiber within a well-controlled laboratory wind tunnel. Ziabicki (1960) was the first to introduce rheological equations into continuous melt spinning. More detailed theoretical analysis began with the work of Sakiadis (1961), who derived air drag relationships for the laminar boundary layer on a continuous cylindrical surface. Sakiadis also considered the effects of a turbulent boundary layer on the continuous fiber but suggested that it best be done experimentally. In high-speed spinning, the boundary layer formed around the fiber is indeed turbulent, and turbulence should be taken into account for the air drag (Ziabicki, 1985). Matsui (1976) has formulated an expression for the air drag coefficient using turbulent theory shown below.

$$C_f = 0.37\,\mathrm{Re}_D^{-0.61} \tag{2.1}$$

Experimental drag force measurements have been recorded on stationary filaments in an airstream (Fukuda, 1966, Thompson, 1959, Anderson and Stubbs, 1958, Shimizu and Okui, 1983, Kase and Matsuo, 1967 and Gould and Smith, 1980), moving filaments in still air (Selwood, 1962 and Kwon and Prevorsek, 1979), filaments spun into still air (Shimizu and Okui, 1983, 1981) and filaments spun into an airstream (Shimizu and Okui, 1983). Theoretical drag force predictions have also been developed, using laminar boundary layer theory applied to flow over a flat plate (Sakiadis, 1961). Both the experimental and theoretical predictions agree quite well. A summary of drag coefficient characteristics for the continuous fiber spinning process, which correspond to equation 2.2, are shown in Table 2.1.

$$C_f = k\,\mathrm{Re}_d^{-n} \tag{2.2}$$

Table 2.1. Experimental Air Drag Characteristic Summary (Ziabicki, 1985)
(Continuous Fiber Spinning)

Researcher(s)	**Experimental Method**	**k**	**n**	**Reynolds Number(Re_d)**
Fukuda, 1966	A, polymer	1.78	0.61	$5<Re<20$
Thompson, 1953	A, polymer	1.30	0.61	$20<Re<150$
Anderson *et al*, 1958	A, polymer	0.84	0.61	$10<Re<60$
Shimizu *et al*, 1983	A,B, polymer	0.77	0.61	$50<Re<400$
Kase *et al*, 1967	A, polymer	1.23	0.81	$3<Re<100$
Gould *et al*, 1980	A, polymer	0.41	0.61	$20<Re<200$

Note: A-measurements made on continuous filaments falling in still air.
B-measurements made on continuous stationary filaments in airstream.

The majority of published literature focuses on the process of continuous fiber spinning, where a molten filament is extruded through a small orifice, attenuated primarily through tension provided and subsequently collected by a take-up reel. Most products produced by this method are polymer yarns and fiber optic cable. On the contrary, the process of discontinuous fiber spinning has yet to be examined and the bulk of industrial research is limited and/or retained as industrial trade secrets. Therefore, the first portion of the research detailed herein focuses on the study of drag force measurements for discontinuous fibers in which turbulent air interaction is the primary driving force for fiber attenuation.

There are numerous researchers who have modeled in detail the process of continuous fiber spinning used to produce polymer and glass fibers. Later, Choudhury and Jaluria (1997) examine the practical aspects in the drawing of an optical fiber. The authors examined the neck-down profile of glass fibers using a surface force balance and the contribution of body and surface forces during the drawing process. Choudhury *et. al.* (1999) developed a computational model for generating the neck-down profile for glass flow in optical fiber drawing. Gupta *et. al.* (1996) developed a nonisothermal model of glass fiber drawing stability, which indicates that the stability of the spin line is strongly influenced by the temperature dependent glass viscosity. They also suggested that previous numerical predictions of nonisothermal stability were underresolved and more sophisticated viscoelastic and heat transfer models are needed. The researchers concluded that the draw resonance, caused by constant speed take-up device, leads to non-constant axial tensile forces with the fiber. Their examination of a nonisothermal fiber drawing process contradicts previous research of Shah and Pearson (1972 a,b) which found unconditionally stable solutions based on non-converged results. Gupta *et. al.* (1996) found that the correlation of the temperature dependent glass viscosity has a strong influence on process stability. The viscosity generally has an adverse effect on stability, however decreased viscosity in attenuation processes generally improves stability. Present continuous spinning models have predicted draw ratios of 10^{-4} with the addition of heat transfer, but the models are incapable of predicting draw ratios of 10^{-5}, which occur in industrial spinning processes. Due to the widespread variation in simulation results, there is a need to increase the complexity as well as the accuracy of numerical models in continuous spinning processes.

Yarin *et. al.* (1999) examined the chaotic variation of the fiber radius in glass fiber drawing. The draw resonance in continuous spinning processes, which is due to the constant take-up speed of the winder, results in self sustained oscillations of the fiber radius. However, this phenomenon has not been observed in discontinuous fiber processes. Other researchers (Choudhury *et. al.* 1994, Choudhury and Jaluria, 1997 and Simpkins and Blythe, 1997) examined cooling and the prediction of the temperature in optical fibers during the drawing process.

All of the research completed in glass fiber drawing has focused on continuous spinning processes that are roughly fixed on both ends and more well behaved than discontinuous spinning processes. To date there have been no known attempts or published literature reviewing the formulation and development of specialized techniques that examine the phenomenon of discontinuous fiber manufacturing. The research presented herein examines and details the development of experimental and numerical methods aimed at characterizing the attenuation and formation of a molten glass filaments, which occur in industrial spinning processes. Several efforts have been made to model fiber motion during production, however interactions between the fiber and surrounding fluid have been ignored (Steve Gross7, 1997).

It is the goal of this research to study the air/fiber interaction that occurs during discontinuous fiberization by applying techniques of former and contemporary researchers, in addition to new techniques developed herein, which focus on experimental drag force measurements and CFD model simulations.

CHAPTER THREE

FORCE TRANSDUCER

Currently, there exist no commercially available dynamic force transducers with sufficient dynamic response or the desired sensitivity and resolution required to measure the drag force fluctuations of discontinuous mircofibers. Thus, a force transducer approaching these critical design characteristics has been developed. Possessing a fundamental design frequency of approximately 1000 Hz, the dynamic force sensor is capable of measuring milligram fluctuating tensile forces (10^{-4} N) with an estimated resolution of several hundred micrograms (10^{-5} N). The fluctuating force data is utilized to determine the glass fiber drag coefficient for various flow conditions.

3.1 Grid Generated Turbulence

The first step toward measuring the fluctuating drag force on a discrete fiber begins with simulating the turbulent flow environment of the industrial process within a well-controlled laboratory wind tunnel where it may be carefully characterized. Past research of Tresso (1998), Tresso and Munoz (2000) and Mohamed and LaRue (1990) was utilized to develop, within a wind tunnel test section, the nearly homogeneous and isotropic flow conditions downstream of a square grid. Isotropic flow occurs when each of the three fluctuating velocity components are invariant due to an arbitrary rotation of the defining principal axis (McComb, 1990) given mathematically by

$$\overline{u'v'} = \overline{v'w'} = \overline{u'w'} = 0 \tag{3.1}$$

Homogeneous turbulence is also invariant due to an arbitrary rotation of the defining axis, such that the variances of the fluctuating velocity components are identical (McComb, 1990).

$$\overline{u'^2} = \overline{v'^2} = \overline{w'^2} \tag{3.2}$$

It is well founded that downstream of a grid there appear three distinct flow regions as shown in Figure 3.1 (Mohamed and LaRue, 1990). The Decay Power-Law region is generally characterized by homogeneous and isotropic flow and identified by the downstream decay of turbulent kinetic energy.

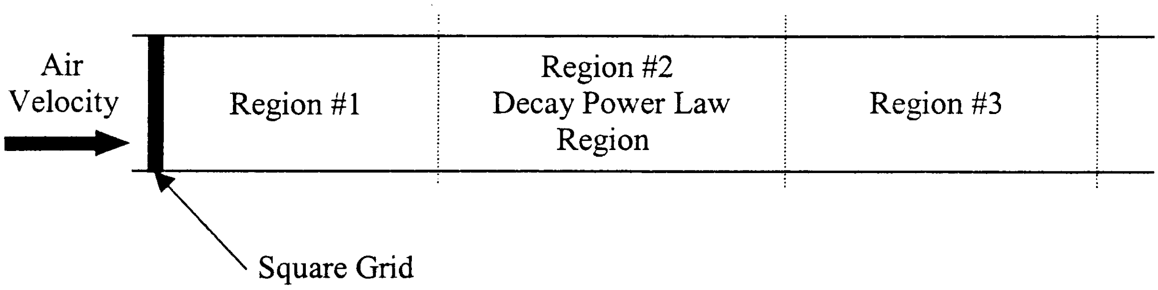

Figure 3.1. Illustration of regions previously identified in grid generated turbulence.

A dynamic force sensor and fiber were placed within the homogeneous, isotropic flow region where integral scale eddy sizes are the same in the cross flow directions and only twice as large in the flow direction. Assuming that large-scale turbulent eddy and force fluctuations are invariant due to an arbitrary rotation of the defining axis simplifies the otherwise more complex and unknown turbulent flow field.

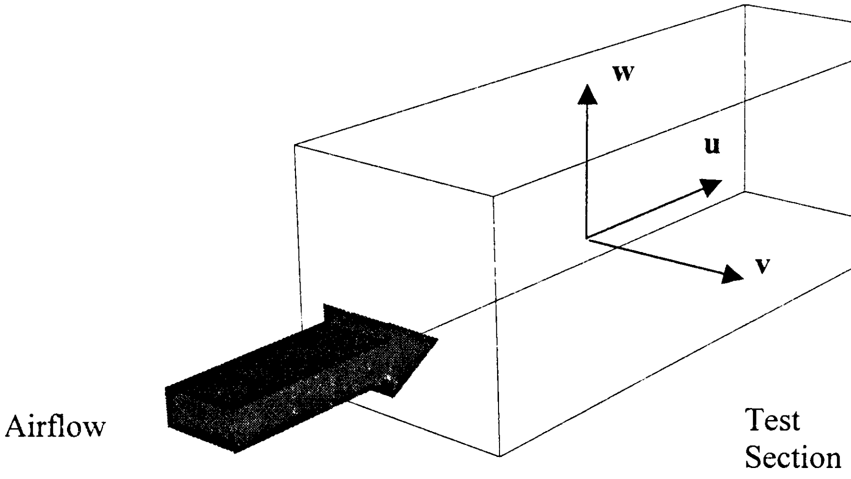

Figure 3.2. Principal velocity components

Each of the three velocity components can be separated into two distinct parts as shown in Figure 3.2; the fluctuating components, denoted by a prime, and the average components denoted by an upper case. The total contribution for each velocity component is given as

$$u = u' + U \tag{3.3}$$

$$v = v' + V \tag{3.4}$$

$$w = w' + W \tag{3.5}$$

The fluctuating components of interest represent the turbulent fluctuations of the flow.

3.2 Friction Drag Coefficient

Ziabicki (1960) was the first to introduce rheological equations into continuous melt spinning. More detailed quantitative analysis began with the work of Kase and Matsuo (1965), who made the theoretical prediction for continuous melt spinning introducing the energy equation from empirical data for the heat transfer. Sakiadis (1961) derived the air drag coefficient on a moving continuous cylinder, oriented parallel to the mean flow direction, from laminar boundary layer theory. The measurements of air drag on filaments falling in still air where conducted by Higuchi and Katsu (1960). However, in high speed spinning, the boundary layer formed around the fiber should be turbulent, and turbulence theory should be taken into account for the air drag (Ziabicki, 1985). Matsui (1976) has formulated a simple expression for the drag coefficient using turbulent theory. Regardless of the method employed, (i.e. measurements made on a stationary filament under known tension or development of turbulent boundary layer theory) drag coefficient results vary. By implementing the dynamic force transducer (discussed in Section 3.3) fluctuating force measurements may be recorded and used to determine more accurately than past researchers the air drag coefficient on a discrete glass fiber for various flow conditions and fiber sizes.

Drag is the resisting body force acting opposite but parallel to the direction of motion. The drag force on a cylinder in cross flow depends strictly on cylinder geometry and flow parameters. Drag force, F_D, of a smooth cylinder of diameter D, moving at speed V, through a viscous incompressible fluid with density ρ, and viscosity μ, can be written as a function of these parameters given as

$$F_D = f(D, V, \mu_a, \rho_a) \tag{3.6}$$

Implementing dimensional analysis and the Buckingham Pi theorem (Fox and McDonald, 1992) the drag coefficient, C_D, of a smooth cylinder can be experimentally determined as a functional relation between two non-dimensional parameters given as

$$\frac{F_D}{\rho_a V^2 D^2} = f\left(\frac{\rho_a V D}{\mu_a}\right) \tag{3.7}$$

The relationship of equation 3.7 is valid for incompressible flow of any body shape, where D, is the characteristic length used for the Reynolds number calculation. The drag coefficient is defined as

$$C_D = \frac{F_D}{\frac{1}{2}\rho_a A V^2} \tag{3.8}$$

where A_s is the surface area of the fiber exposed to the flow.

Implementing the dynamic force transducer, the quantity F_D, can be determined experimentally for various turbulent flow conditions (i.e. Reynolds number). Thus, by plotting the relationship of equation 3.8, a best-fit line will take the form of

$$C_D = k \operatorname{Re}_D{}^{-d} \tag{3.9}$$

which is the functional relationship that will be examined and compared to published results for continuous fibers.

3.3 Dynamic Force Sensor

The sensing element selected for the force transducer is a polyvinylidene fluoride (piezoelectric) film. When a piezoelectric film is deformed it emits an output voltage proportional to the amplitude of deformation. However, the voltage quickly dissipates, therefore additional steps are required for calibration. Also, the capability of a piezoelectric film is strongly dependent upon interface circuitry. Thus, for the small anticipated forces and the frequency of fiber dynamic response observed from high-speed video (100 Hz $< f_{fiber} <$ 500 Hz), the appropriate amplifier was designed and developed to optimize film response characteristics. Using the Nyquist criteria, a sensing element was designed to possess a natural frequency near 1000 Hz to avoid the effects of aliasing. The greater the film natural frequency the better, however, the design must strike a balance between appropriate frequency response, which improves with sensor stiffness, and measurement sensitivity, which increases with decreased sensor stiffness.

A type DT1-028K piezoelectric film, manufactured by Amp Incorporated, was masked and chemically etched with acetone to the specific dimensions shown in Table 3.1. The film dimensions of Table 3.1 represent the smallest piezoelectric film attainable from the commercially available DT1-028K, which incorporates the desired dynamic characteristics and sensitivity needed for the delicate force measurements.

Table 3.1 Piezoelectric Force Sensor Critical Dimensions

Piezoelectric Film Dimensions(mm)	
Film Length	7.112
Film Width	1.143
Film Thickness	0.230

A discrete fiber was attached to one end of a piezoelectric film while the other end of the film is fixed, producing a cantilever effect with the fiber and film. As the fiber experiences motions caused by the passing air, a resulting dynamic force on the fiber will produce a deflection of the piezoelectric film. The tip displacement of the piezoelectric film was proportional to the tensile force on the fiber. Thus, the output voltage of the piezoelectric force transducer was recorded and converted, by film calibration procedures, to measure the fluctuating tensile forces imparted on the fiber as a result of the turbulent airflow.

The dynamic force transducer consisted of a properly calibrated piezoelectric film, non-inverting operational amplifier and digital band-pass filter. The sensor's functional description is depicted in Figure 3.3.

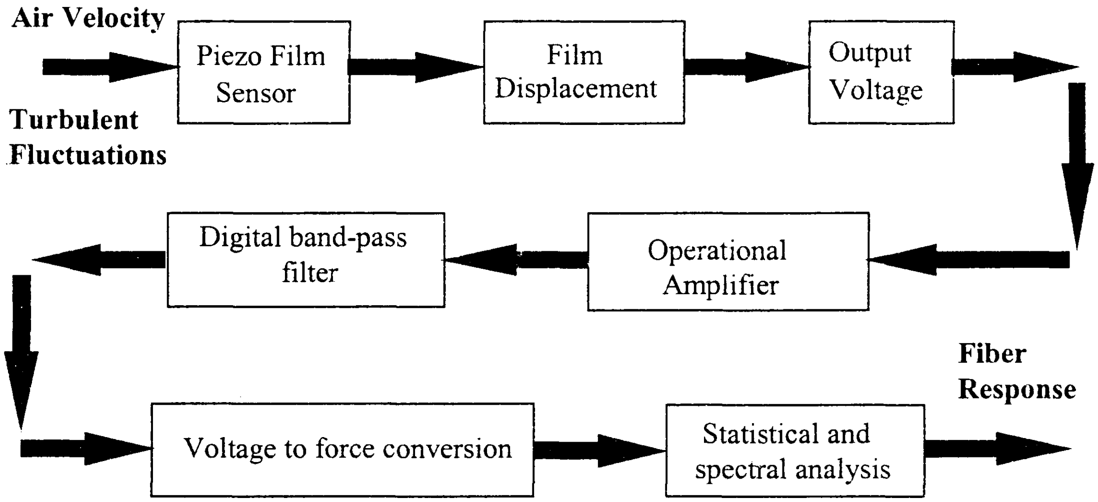

Figure 3.3. Force transducer development

In order to place the film, fiber and electronics in the test section with minimal disturbances to the airflow, an airfoil was designed and built to accommodate the components as shown in Figure 3.4. Thus, for a wide range of Reynolds numbers (based on the grid dimension, $10{,}700 \leq Re_{Mu} \leq 52{,}000$) the flow over the airfoil will minimize the disturbances near the trailing edge of the airfoil due to wake effects and associated turbulent eddies.

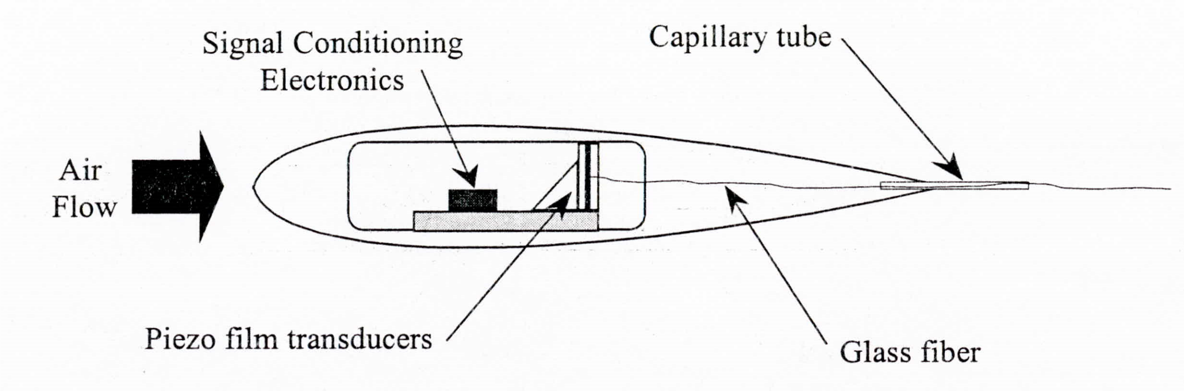

Figure 3.4. Cross section of the 63-3018 NACA airfoil and sensor apparatus.

A NACA 63-3018 airfoil was built using transparent acrylic ribs and model aircraft polyester skin to contain the sensor while minimizing unwanted flow disturbances and enabling visual access for high-speed photography. Preliminary flow visualization techniques show little or no flow separation occurring for a range of flow conditions. The flow around the airfoil was also modeled using FLUENT® (k-ε turbulence model), a commercially available CFD software package, and the results agree with flow visualization observations.

Individual glass fibers of varying diameters (i.e. 5 to 50μm) and lengths (i.e. 100mm to 300mm) will be attached to the piezoelectric film and guided through the airfoil by way of a capillary tube and exit the rear of the airfoil through the same small tube. As the fiber exits the capillary tube outside of the airfoil, flow disturbances caused by the airfoil and capillary tube are minimized. Thus, the trailing half of the fiber is located in a previously well-characterized turbulent airflow (Tresso, 1998, Tresso and Munoz, 2000) with minimal disturbances which could cause considerably erroneous film output signals. The delicate tensile force measurements require the piezoelectric film to be sensitive to small fluctuations. The same turbulent fluctuations that influence the motion of the glass fiber also induce a considerable amount of vibrational noise within the airfoil structure. As a result, the highly sensitive piezoelectric film also records spurious vibrations caused by turbulent fluctuations acting on the foil itself.

To prevent this, an over-sampling technique was utilized to differentiate between fiber fluctuations and unwanted vibrational noise. The noise was over-sampled by recording force transducer fluctuations with no fiber present for a range of flow rates. The over-sampled noise and fluctuating fiber output signals were compared (differenced) producing an output signal that was proportional to only fiber fluctuations. Subsequently, the output signal was digitally filtered and statistically analyzed to determine modal and force characteristics of the discrete fiber.

Preliminary estimates of fiber drag force were estimated by applying the friction drag force for flow over a flat plate (see equation 3.8) and the average friction drag coefficient given as (Schlichting, 1951).

$$\overline{C_f}(x) = 0.0493(\mathrm{Re}_L)^{-1/5} \tag{3.10}$$

Upon substitution of equation 3.10 into equation 3.8, the average drag force for a 0.2 m length fiber subject to a mean axial velocity of 20 m/sec, results in an average drag force of approximately 8.6×10^{-4} N.

In addition to characterizing the turbulent flow field, dynamic analysis of the force transducer, used to measure the fluctuations of the fiber caused by the turbulent flow, was performed. Descriptive equations of motion for the piezoelectric film are shown below. These provide a basis for the measurement system data reduction procedure.

The piezoelectric film used as the dynamic force transducer is positioned in a cantilever fashion and lends itself nicely to the application of the well-known analysis of a single degree of freedom (SDOF), underdamped dynamic system driven by an unknown forcing function. The unknown forcing function is the quantity being measured. The assumptions required are that the

1. force imparted on the piezoelectric film is similar in magnitude to that of the turbulent intensities experienced by the fiber.
2. damping is due to coulomb or viscous forces.
3. forcing function is sinusoidal.
4. mass of the fiber is negligible compared to the that of the system.
5. driving force, due to large (integral) energy containing eddies, acts directly on the piezoelectric film via the fiber.

The second order underdamped single degree of freedom (SDOF) system is shown in Figure 3.5.

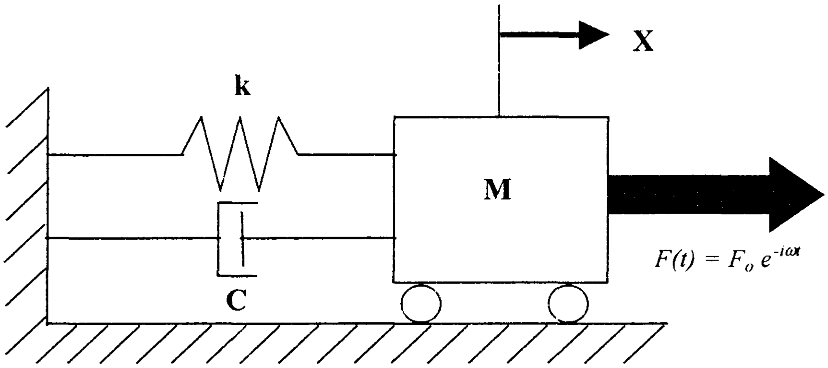

Figure 3.5. SDOF Spring/Mass/Damper system.

The following variables will be defined to represent properties of the SDOF underdamped forced vibration system.

m = mass

c = damping factor

ζ = damping ratio

k = spring constant

$f(t)$ = external forcing function

F_o = force amplitude

ϕ_o = phase angle

x = principal direction of motion

ω = frequency

In general the governing equation for the SDOF underdamped system subject to a periodic force input is given as (Rao, 1995)

$$m\ddot{x} + c\dot{x} + kx = F_o e^{-i\omega t} \tag{3.11}$$

The general forcing function consists of real (Re) and imaginary (Im) parts. The complete solution to the governing equation of motion consists of a homogeneous (transient) solution and a particular (steady state) solution. In this case, the transient solution, which eventually goes to zero, is of no interest to this analysis. Therefore, the focus of the following development will address only steady-state conditions. The general solution to the governing equation is assumed to be

$$x_p(t) = \mathrm{Im}(Ae^{i\omega t}) \tag{3.12}$$

Assuming the displacement amplitude, A is given by

$$A = |A|e^{-i\phi} \tag{3.13}$$

then, the steady-state solution can be rewritten as

$$x_p(t) = \mathrm{Im}[Ae^{i(\omega t-\phi)}] \tag{3.14}$$

If the steady state solution is substituted into the governing equation of motion for the SDOF underdamped system the absolute value of displacement amplitude, A, is found to be

$$|A| = \frac{F_o/k}{\sqrt{\left(\left(1-\frac{\omega^2}{\omega_n^2}\right)^2 + \left(2\zeta\frac{\omega}{\omega_n}\right)^2\right)}} \tag{3.15}$$

The phase angle can be represented as

$$\phi = \tan^{-1}\left(\frac{2\zeta\omega/\omega_n}{1-\omega^2/\omega_n^2}\right) \tag{3.16}$$

The particular solution of the governing equation of motion may be obtained, however the variable of interest is the force amplitude, F_o. All of the unknown variables may be measured or calculated except for the F_o. Equation 3.15 is rearranged to give

$$F_o = k \cdot |A| \cdot \sqrt{\left(\left(1-\frac{\omega^2}{\omega_n^2}\right)^2 + \left(2\zeta\frac{\omega}{\omega_n}\right)^2\right)} \tag{3.17}$$

The natural frequency (ω_n), stiffness (k) and damping ratio (ζ) of the sensing element are known from the piezoelectric sensor calibration (see Section 3.4). In order to calculate the maximum force acting on the piezoelectric film, the amplitude (A) of the fiber/film system must be measured as well as the fundamental frequency of the turbulent driving force (ω).

3.4 Sensor Calibration

To apply the piezoelectric film as a sensing element, the film must be calibrated. The output of the film, in volts, was converted to amplitude in millimeters. This was accomplished using a Kodak Ektapro-TR, high-speed video system to record film tip displacements as voltage data was simultaneously recorded. Figure 3.6 shows the relationship between piezoelectric film displacement and output voltage.

The stiffness of the piezoelectric film was also a paramount issue as the natural frequency of the film had to be higher than that of the phenomenon being measured. As indicated earlier, there exists a trade-off between film stiffness and sensitivity. As the stiffness of the piezoelectric film increases the sensitivity decreases. If the stiffness of the sensing element were decreased, the piezoelectric film would provide a greater output voltage due to the increased tip displacement for a given force, but would fail to respond to the higher frequency dynamic response of the fiber. In contrast, if the stiffness of the sensing element were increased, the piezoelectric film's ability to respond to the fluctuations would be adequate, although a considerable decline in sensitivity would occur. Thus, there is a critical design issue regarding the trade-off between film stiffness and sensitivity.

The stiffness of the film was calculated by applying a known weight to the film tip and recording the tip displacement. A large bellows was used with the Kodak high-speed video system to capture enlarged images (approximately 20X) of the film tip displacement. The results are shown in Table 3.2.

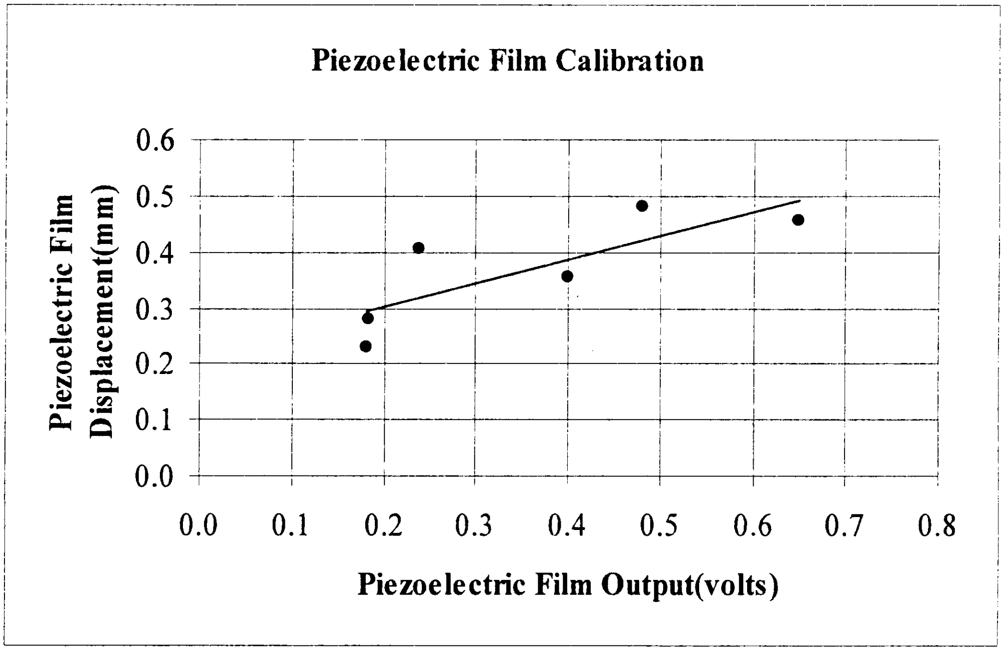

Figure 3.6. Piezoelectric film calibration.

Table 3.2. Piezoelectric Film Stiffness Calibration.

Piezoelectric Film Stiffness Calibration				
weight(N)	**film tip displacement(mm)**	**film tip displacement(m)**	**film stiffness (N/mm)**	**film stiffness (N/m)**
0.00135	0.12700	0.00012700	0.01059	10.59171
0.00069	0.05080	0.00005080	0.01361	13.61041
0.00027	0.02540	0.00002540	0.01051	10.50520
		average stiffness	**0.01157**	**11.56911**

The piezoelectric film damping coefficient (ζ) and natural frequency (ω_n) were determined by displacing the film tip an undetermined distance and recording the resulting time varying output voltage. The output voltage data is shown in Figure 3.7.

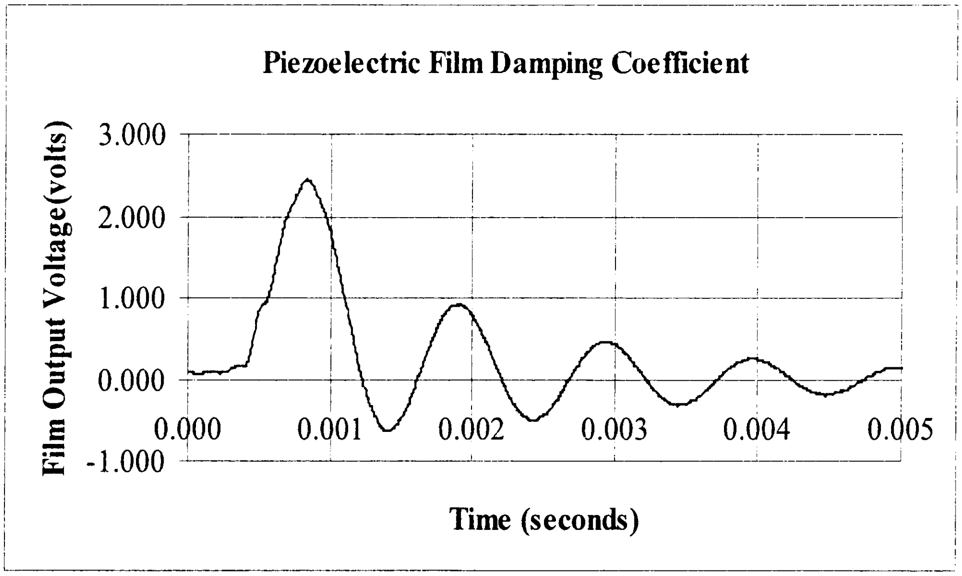

Figure 3.7. Piezoelectric Film Damping Coefficient

The damping ratio of the piezoelectric film was determined using the fundamental relationship shown in equation 3.18. Using the damped natural frequency data shown in Figure 3.7, the damping ratio was determined using the logarithmic decrement law given as

$$\frac{1}{r}\ln\left(\frac{X_0}{X_4}\right)=\frac{2\pi\zeta}{\sqrt{1-\zeta^2}} \qquad (3.18)$$

where X_0 and X_4 represent the first and fourth positive peak amplitudes of the decaying exponential wave form and r is the number of cycles. The logarithmic decrement law was applied to three successive positive peaks. These displacements, recorded in volts, can be easily converted to displacement amplitude in millimeters. The damped natural frequency of the transducer is approximately 950 Hz.

Using the maximum voltage output and converting this output voltage to a corresponding displacement of the piezoelectric film, the logarithmic decrement law introduced above can be utilized to directly calculate the damping ratio (ζ). The damping ratio of the film is calculated to be $\zeta = 0.13$.

The frequency response of the transducer is shown in Figures 3.8 and 3.9. The non-dimensionalized curves indicate the response of the transducer for a range of frequencies. Increasing the natural frequency of the transducer will increase the range of frequencies for which the amplitude ratio curve is relatively flat. Thus, it is necessary for the measurement device to possess a high natural frequency to accurately measure a high dynamic response of the fiber (Doebelin, 1990). The widest flat portion of the amplitude ratio curves exist for damping ratios ranging from 0.6 to 0.8. The same is true for the phase response curve. Thus, the optimal range for the damping ratio is approximately 0.6 to 0.8. In addition, zero phase angle would be ideal, although is rarely attainable.

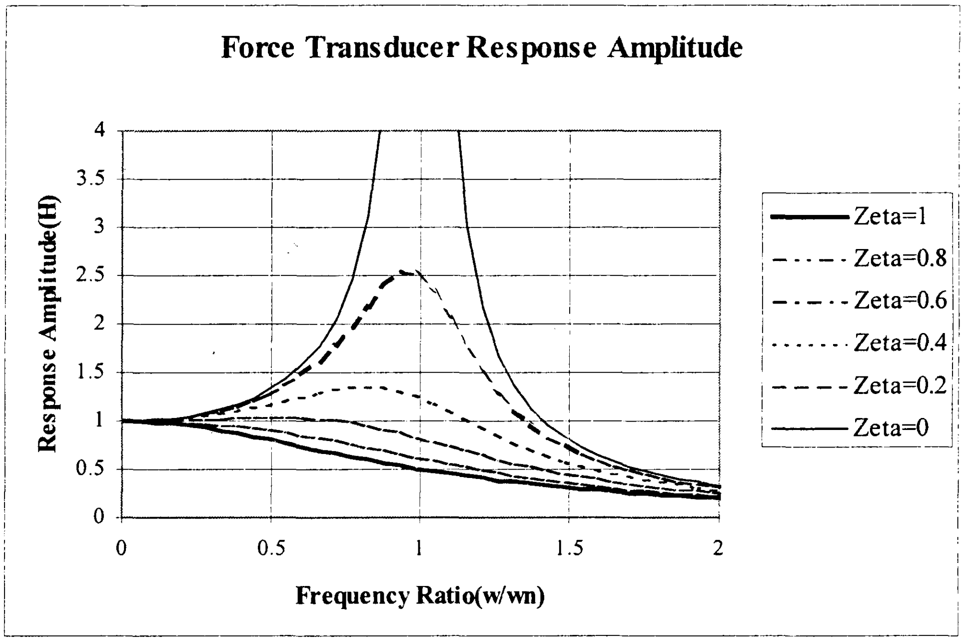

Figure 3.8. Force transducer frequency response curves

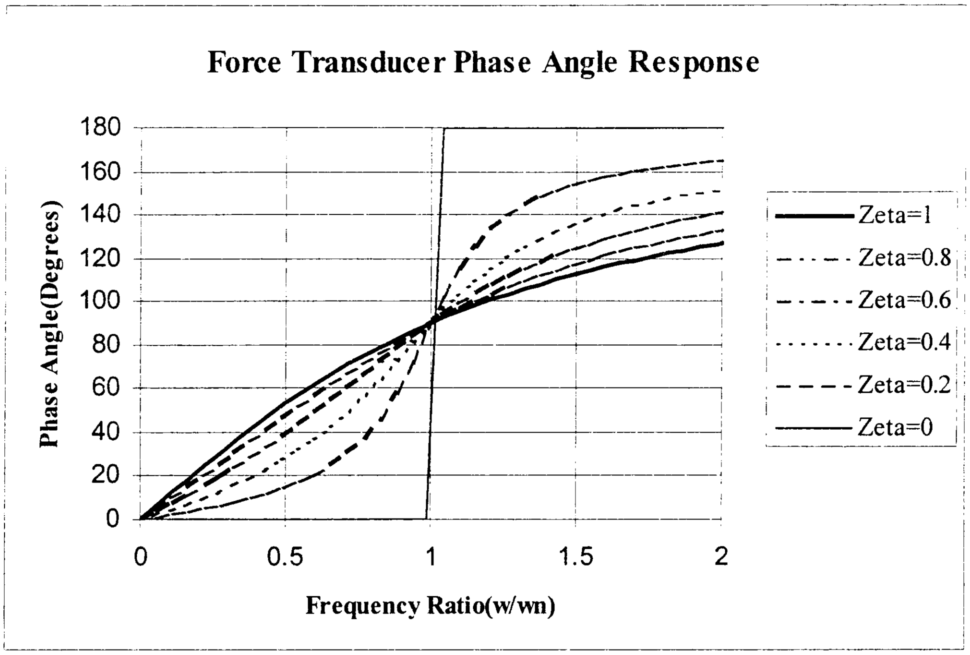

Figure 3.9. Force transducer phase response curves

Given the transducer natural frequency of approximately 940 Hz and an estimated fundamental driving frequency of the system, the resulting frequency ratio can be calculated. Recalling that the damping ratio of the transducer is 0.13, the resulting points from Figure 3.8 and 3.9 can easily be identified.

3.5 Data Reduction Procedure

The friction drag coefficient, C_f, was experimentally determined by measuring the fluctuating drag force on a discrete fiber for various flow conditions and fiber sizes. The friction drag coefficient (see equation 3.8) is dependent upon the following experimental variables.

- Air velocity
- Fiber diameter and length
- Sensing element stiffness, natural frequency and damping coefficient.
- Turbulent airflow driving frequency.
- Maximum fiber amplitude(displacement)

The first step to measuring the fiber drag force was to calibrate the piezoelectric sensing element used as the dynamic force transducer. Through a series of detailed laboratory experiments the following relationships were determined.

- piezoelectric film natural frequency (see Figure 3.7).
- piezoelectric film stiffness (see Table 3.2).
- film displacement as a function of output voltage (see Figure 3.6).

The force sensor needed to possess a natural frequency at least twice that of the maximum expected fundamental frequency of the fiber. Initial high-speed video analysis was used to determine the maximum expected frequency of the fiber. As a result, the natural frequency of the piezoelectric film was designed to be approximately 950 Hz. Using the calibration data, the film characteristics, such as damping coefficient and stiffness, were determined. The piezoelectric sensing element was then integrated into the airfoil structure along with the required electronic circuitry. The force transducer and fiber were then placed within the wind tunnel test section and fluctuating voltage data was recorded for various turbulent flow conditions and fiber sizes. The experimental data reduction procedure is outlined below.

1. Using Figure 3.6, the voltage data was converted to a corresponding displacement amplitude (A) in meters.
2. The turbulent airflow fundamental driving frequency (ω) was estimated using both autocorrelation data and grid dimensions (see Chapter 4).
3. Invoking equation 3.17 and using the previously identified film properties (i.e. stiffness (k), damping coefficient (ζ) and film natural frequency (ω_n)), the fiber drag force (F_d) was calculated.
4. Using equation 3.8, drag force, along with air density, velocity and fiber surface area, were used to calculate the friction drag coefficient, C_f.

CHAPTER FOUR

EXPERIMENTAL RESULTS

The experimental approach consisted of measuring the fluctuating drag force on discrete glass and polymer fibers within a well-characterized turbulent flow field. Grid generated turbulence was imposed on the fiber to simplify the flow while approximating mixing conditions of the industrial fiberizing process. Using a three-dimensional hot-wire anemometer, velocity fluctuations in each principal flow direction were recorded and analyzed. The turbulent measurements characterized a homogeneous, isotropic flow region that occurs downstream of a square grid. Within this region the characteristic, large-scale (integral) turbulent eddies were assumed similar in the cross flow velocity directions. Furthermore, the displacement (amplitude) of the fiber, which is hypothesized to be a result of the integral scales, is also assumed similar in both cross flow directions.

The dynamic force transducer was used to take fluctuating force measurements on both discrete glass and polymer fibers. The fluctuating force data was statistically analyzed and the appropriate signal processing routines were applied. A digital band-pass filter was applied to filter any spurious noise. Measuring an over-sampled noise background, the fiber output signal was conditioned by subtracting the former; thus producing a true fluctuating fiber output signal.

Initial examination of the fiber using high-speed video estimated the fundamental frequency (ω) of the turbulent driving force to be approximately one half of the natural frequency of the force transducer. Upon further examination, using both autocorrelation and grid dimension data, the expected driving frequency of the system was larger than expected. Using axial fluctuating velocity data, the autocorrelation, $R_u(\tau)$, was calculated. The large (integral) energy containing time scales could then be estimated by calculating the area under the autocorrelation curves. Figure 4.1 shows the autocorrelation data determined 80 mesh lengths downstream of the 25.4 mm grid. The area under the autocorrelation curves approximates the integral time scales of turbulent motion (Tresso and Munoz, 2000b).

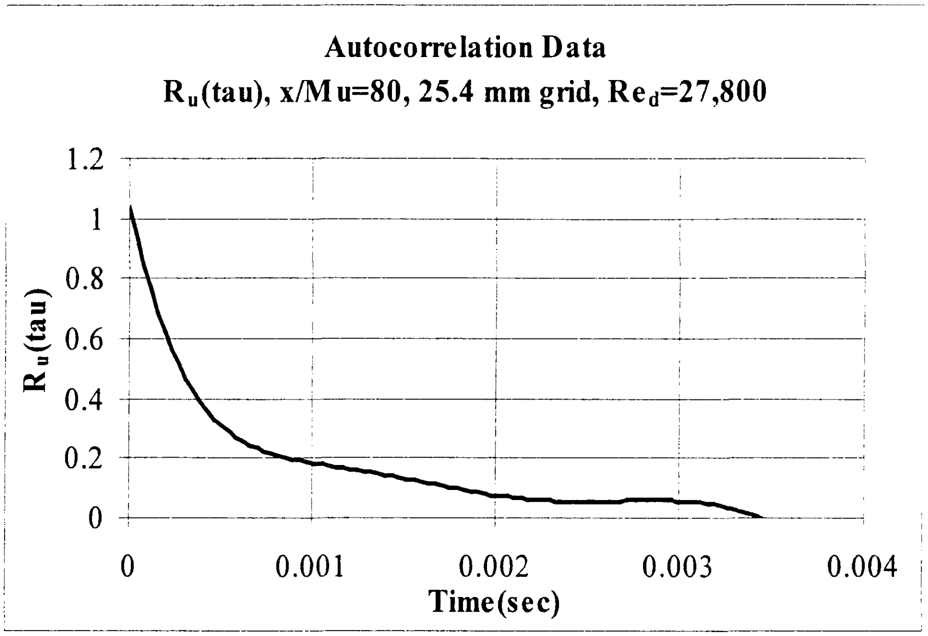

Figure 4.1. Autocorrelation time scale determination.

An alternative approach was to use the GGT scale and mean axial velocity to estimate the integral time scales, given by equation 4.1. The approach assumes that the largest possible scales of motion are no larger than the 25.4 mm grid dimension. For flow with a characteristic velocity, U, and length scale, L_{grid}, the characteristic time scale is

$$T_t \approx \frac{L_{grid}}{U} \tag{4.1}$$

A comparison of the two methods is shown in Figure 4.2.

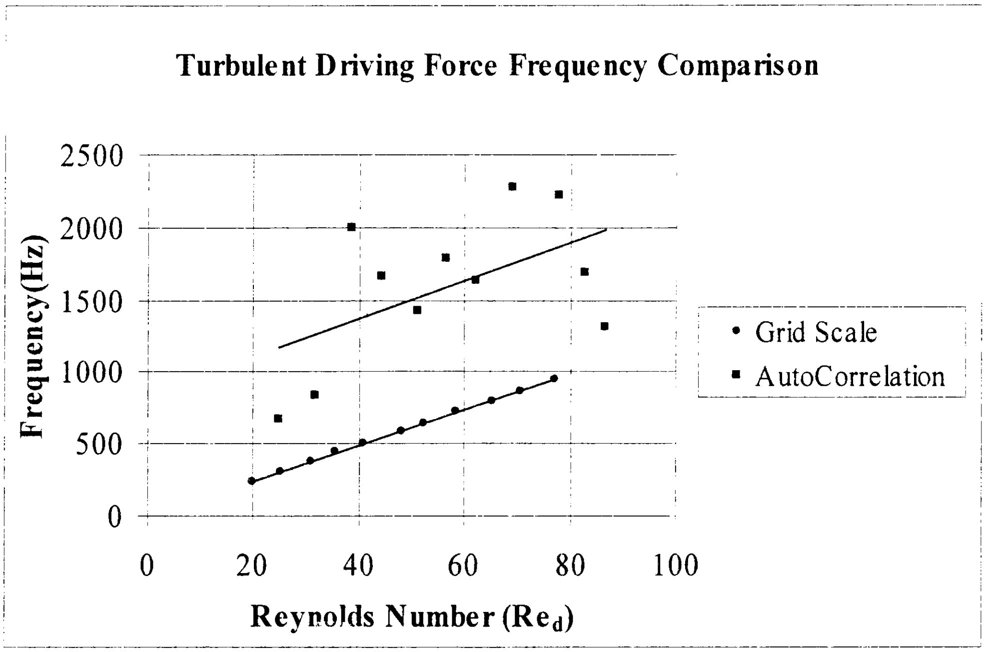

Figure 4.2. Driving frequency comparison.

The scatter in the autocorrelation data may be attributed to the large uncertainty of the computation and that of turbulence, however the more conservative estimate using the grid dimension and mean axial velocity provides less scatter with a similar trend. The reason for offset between the two data sets of Figure 4.2 is unknown.

Given the driving frequency of the turbulence and the piezoelectric film's natural frequency 940 Hz, the frequency ratio (ω/ω_n) will approach unity with increasing Reynolds number (see Figure 3.8). The natural frequency of the piezoelectric film could not be enhanced due to the limits of existing films that possessed the desired sensitivity.

Ideally a sensing element with a natural frequency in excess of 2000 Hz would avoid a frequency ratio near one and subsequent resonance of the system.

Nonetheless, a dynamic correction factor was used to compensate for a large driving frequency and relatively low piezoelectric natural frequency. The correction factor shown in equation 4.2, should compensate for frequency ratios which approach unity.

$$\sqrt{\left(\left(1-\frac{\omega^2}{\omega_n^2}\right)^2+\left(2\zeta\frac{\omega}{\omega_n}\right)^2\right)} \tag{4.2}$$

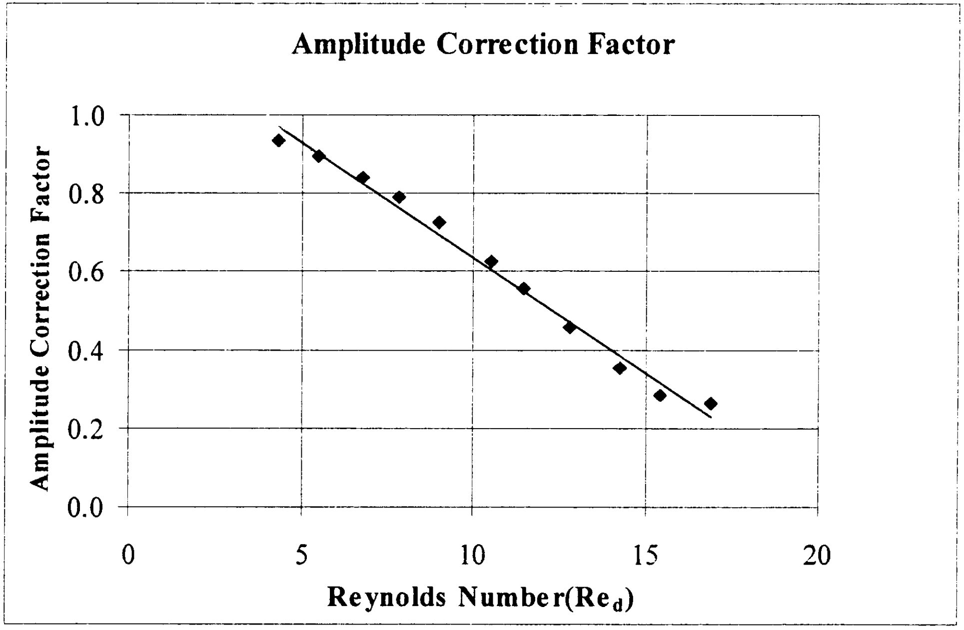

Figure 4.3. Amplitude correction factor.

Upon calculation of the drag force, the correction factor did compensate for frequency ratios approaching one, however it also reduced the sensitivity of the force sensor by collapsing the scatter in the force data for a range of Reynolds numbers and fiber sizes. The displacement amplitude and force data are summarized in Figures 4.4, 4.5 and 4.6.

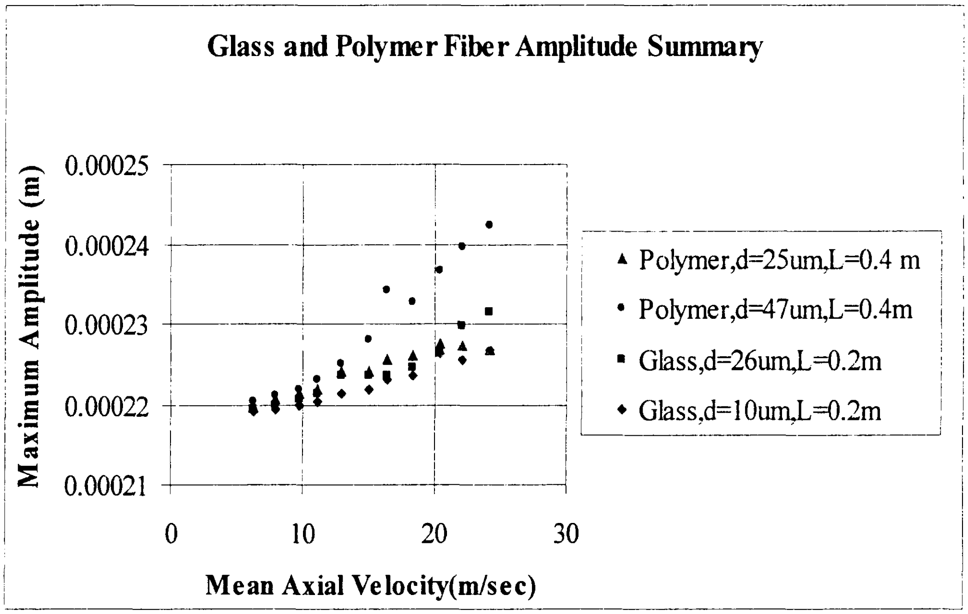

Figure 4.4. Glass and polymer fiber amplitude summary.

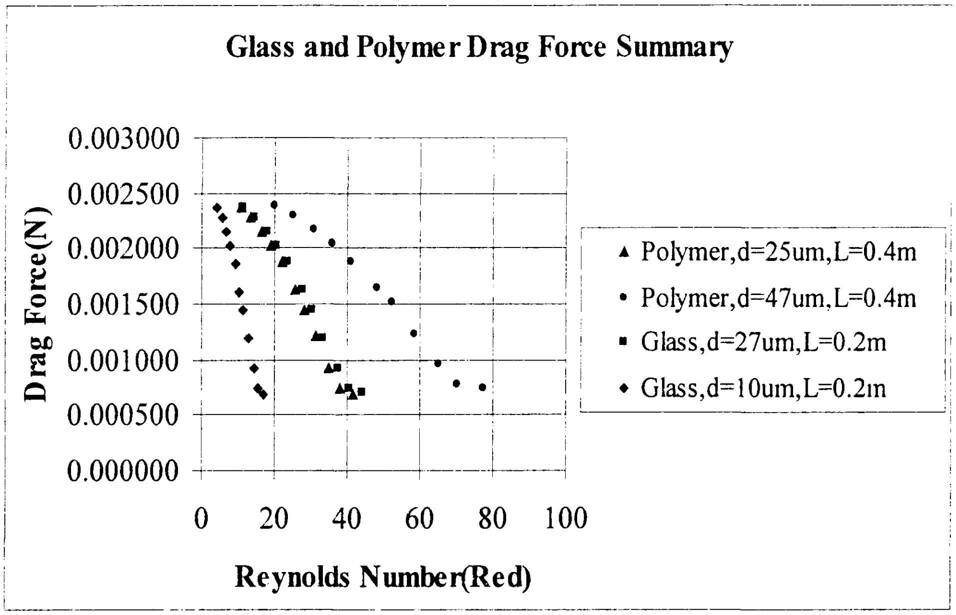

Figure 4.5. Fiber drag force summary as a function of Reynolds number.

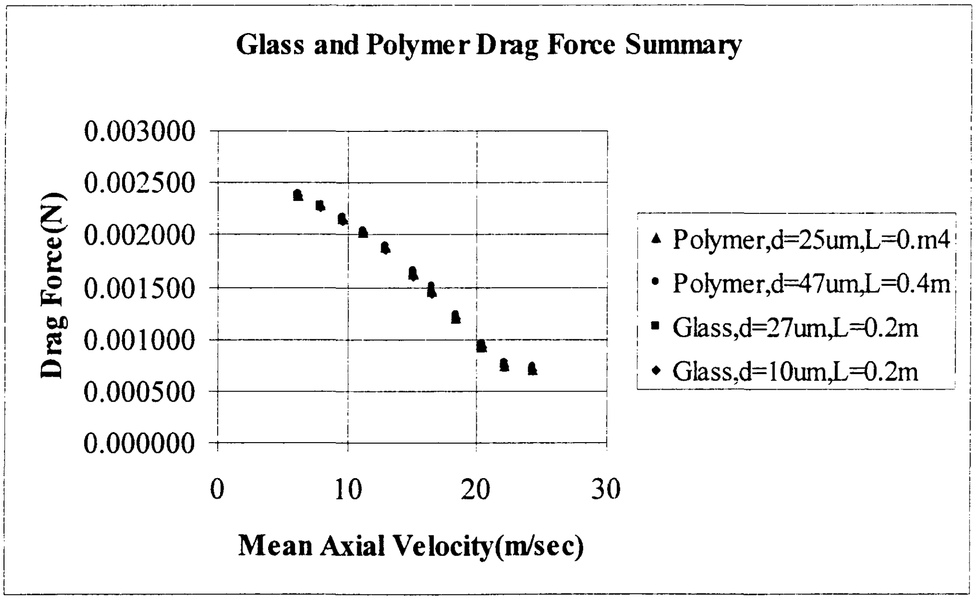

Figure 4.6. Fiber drag force summary as a function of mean axial velocity.

Examining the amplitude data of Figure 4.4., the sensor seems to adequately measure the small amplitude fluctuations of the fiber. However, as the driving frequency of the system approaches the natural frequency of the force sensor, the amplitude correction factor reduces the data scatter. If the drag force is plotted as a function of mean axial velocity, rather than Reynolds number (i.e. removing any dependence on fiber diameter), the data collapses with little apparent scatter. The lack of scatter in the data is due to a decrease in sensitivity as a result of the compensation provided by the amplitude correction factor. Therefor, the piezoelectric film sensor is capable of measuring general trends of fiber drag force, but does not possess the sensitivity or sufficient dynamic response to resolve the smallest fluctuations in drag force.

The drag coefficient calculated from the drag force data for each fiber type and size are shown in Figure 4.7. The condensed drag force data is shown in Figure 4.8.

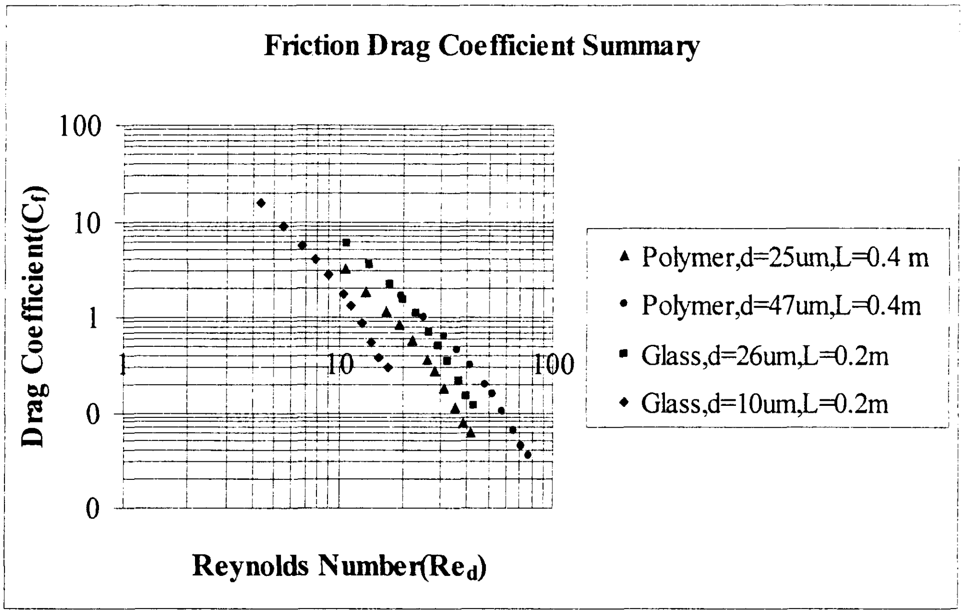

Figure 4.7. Friction drag coefficient summary.

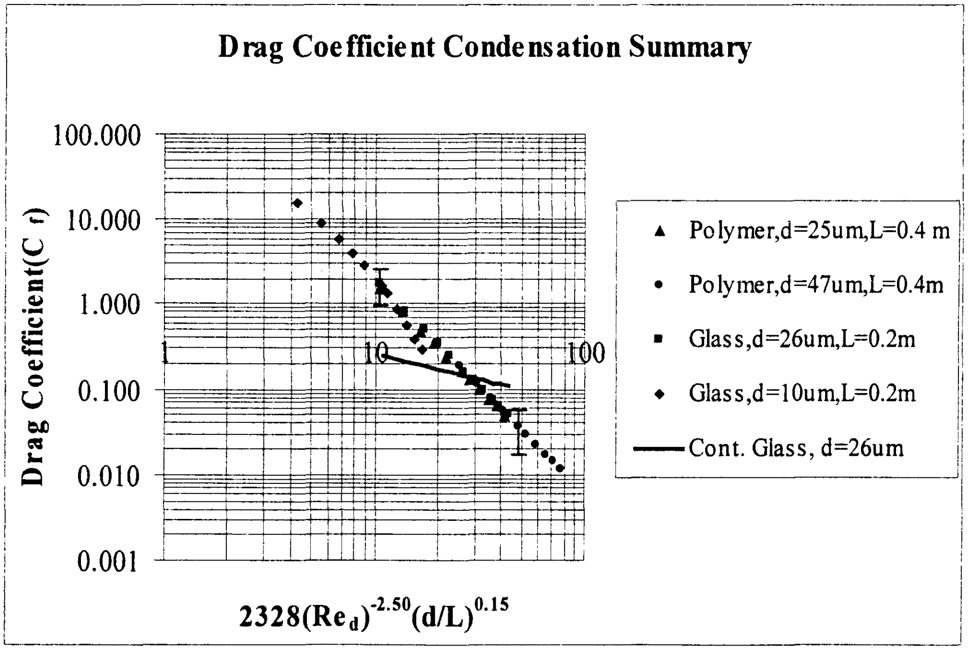

Figure 4.8. Friction drag coefficient condensation summary.

Recalling equation (1.1), the best-fit coefficients k and n were calculated for the friction drag data. For the data shown in Figure 4.8, k=2328 and n=2.50, which are quite different than the friction drag data previously published for continuous fibers (Ziabicki and Kawai, 1985). Although specific numerical values for k and n from previous work depended on experimental procedure, typical values were $k \approx 1.30$ and $n \approx 0.61$.

CHAPTER FIVE

NUMERICAL MODIFICATIONS

The CFD analysis focused on the molten glass filaments as they exit the sidewall of the spinning disk in the horizontal direction (see Figure 5.1). In this region inertial and centrifugal forces dominate as the molten fiber is forced horizontally outward. As the filament is extruded, the effects of the high-speed air jet predominate and redirect the molten filament downward. Subsequently, the heat and momentum transfer imparted on the fiber causes it to attenuate, cool and fracture. It is hypothesized that the effects of heat and momentum transfer immediately after molten filaments exit the disk sidewall, within the critical zone (see Figure 5.1), play a crucial role in attenuation, cooling and formation of discontinuous fibers. The global factors that influence fiber formation are the fluid properties, process environment (i.e. air/glass temperatures and velocities) and the geometric configuration of the spinner. Each of these factors, other than the spinner configuration, within the glass spinning system is extremely difficult to characterize experimentally with current methods. However, the development of a comprehensive CFD model will enable researchers to examine the two-fluid interaction and thermal characteristics within the air/fiber system. The numerical model may be used for quantitative analyses to improve the fundamental understanding of the spinning process by simulating the interactions that occur during fiber formation .

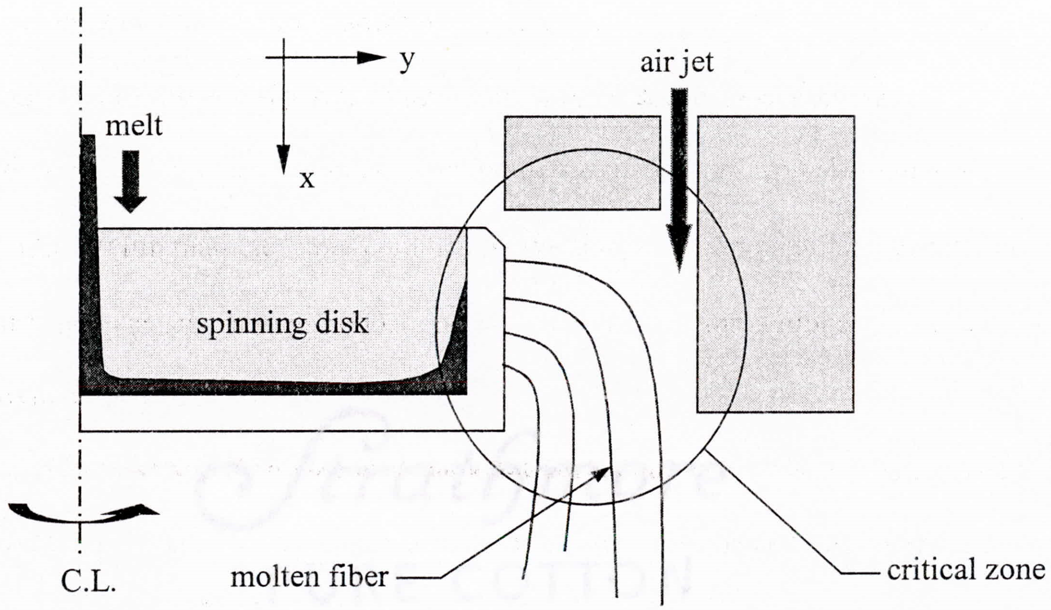

Figure 5.1 Rotary spinner critical zone cross section

A specialized CFD code, called RIPPLE, provides the basis to develop the most complete numerical model to date that can locally simulate the process of fiber formation similar to that occurring in industry. RIPPLE, in its original form , is a CFD model for transient, one fluid, two-dimensional flows of incompressible fluids with surface tension on free surfaces of a general shape (Kothe *et. al.*, 1991).

Modifications to the current code include the addition of the following.

- A more accurate interface tracking algorithm.
- A two-fluid, incompressible variable density and viscosity model.
- A more robust surface tension model.
- An improved pressure coefficient stencil used in the ICCG pressure solution algorithm.
- An energy equation model which includes conductive, convective and radiation heat transfer.

Currently, there exists no commercially available computer code that permits user access and modification of the source code to effectively model the air/fiber interaction as it occurs in industrial fiberizers. Source code access to most CFD codes would enable the user to initiate and develop a comprehensive fiberization model. However, that option is only available for developers of commercial codes. In general, the majority of commercially available CFD codes are inadequate for the studying specific research topics. Although, three-dimensional CFD codes for the simulation of multiphase flows are currently being developed, there is much that can be gained from two-dimensional model development and simulations. The development of a three-dimensional code has been completed at Los Alamos National Laboratory (LANL). The newly developed code offers the best long-term solution to modeling this complex, multiphase problem. However, it has only recently been made available to select university and laboratory research groups outside of LANL. The further development of RIPPLE was completed to learn about the same methods utilized in the three-dimensional code. The development also provides a means to become more familiar with the fiberizing process and the critical factors that influence fiber formation as well providing the necessary computational and analytical background to receive and work with the three-dimensional code as it becomes available. Therefore, it is not the intent of the proposed research to develop a complete and comprehensive model, but to take the first steps toward achieving that goal. In addition, the focus of the numerical development is not specifically code development, but rather the investigation of the air/fiber interaction as it occurs in industry through application of CFD techniques. The benefit of using RIPPLE, rather than other commercially available CFD codes, is that the user has complete source code access to a well-founded CFD flow solver. Rather than attempting to develop a new CFD flow solver, RIPPLE can be modified to simulate the incompressible, free surface flow of molten glass that occurs in the industrial fiberization processes. The appeal of RIPPLE, for the specific application of fiber attenuation, is that it allows the user to model the controlling physical phenomenon at a microscopic (1-100 μm) fiber scale using a fully customized model that will be developed specifically for characterizing the shear attenuation of glass filaments within rotary spinning processes. The process of discontinuous glass fiber manufacturing as it occurs in rotary spinning processes is extremely complex and requires an advanced, very specific CFD model to properly characterize the shear air/fiber interaction.

The modified version of RIPPLE, referred to as Vi^3S-FLOW (Variable, Incompressible, Interface, Instability, Shear, Flow) from this point onward, may be used to simulate the localized mechanisms attributed to attenuation and formation of glass fibers produced during rotary spinning processes. Due to the inherent complexity of discontinuous fiber manufacturing, the CFD model development was limited to selected mechanisms of fiber formation while attempting to maintain fundamental process interactions. The CFD model simulates the two-dimensional, shear attenuation of a single molten glass filament by a high-speed air jet similar to that shown in Figure 5.2. The die geometry, material properties and process parameters are similar to those of the industrial process.

Vi^3S-FLOW serves as a localized model of fiber attenuation and is not capable of simulating the global dynamics of fiber motion, attenuation and fracture. The primary reason is due to an inability to accurately resolve the computational mesh aspect ratios of the attenuating fiber. The necessary radial resolution of the fiber must be on the order of 1.0 to 5.0 μm when considering small fibers (i.e. < 50 μm), while the length of a newly formed fiber reaches approximately 0.05 m. Ideally an adaptive or biased mesh scheme is preferred as the fiber experiences rapid changes in diameter, due to sharp velocity, material and temperature gradients within the air/fiber system. Small computational cell sizes are needed to accurately approximate these gradients, however Vi^3S-FLOW has difficulties implementing computational cells that are highly skewed (i.e. large aspect ratios). Even aspect ratios of 2:1 cause convergence problems. Achieving the required grid resolution needed to capture the rapid changes in fiber diameter while implementing square computational cells results in a large computational mesh. The use of a large computational mesh (i.e. greater than 10,000 cells) requires significant computing resources and is not feasible at this time. There is a limit on the length of fiber that can be simulated in a reasonable amount of time, which depends on the mesh density and the density and viscosity ratios implemented in the simulation. A typical simulation of a 10 mm long 400 μm diameter fiber completed on a 20x500 computational mesh with a density and viscosity ratio of 1000:1 and 10:1 requires a computational run-time of approximately 6 hours.

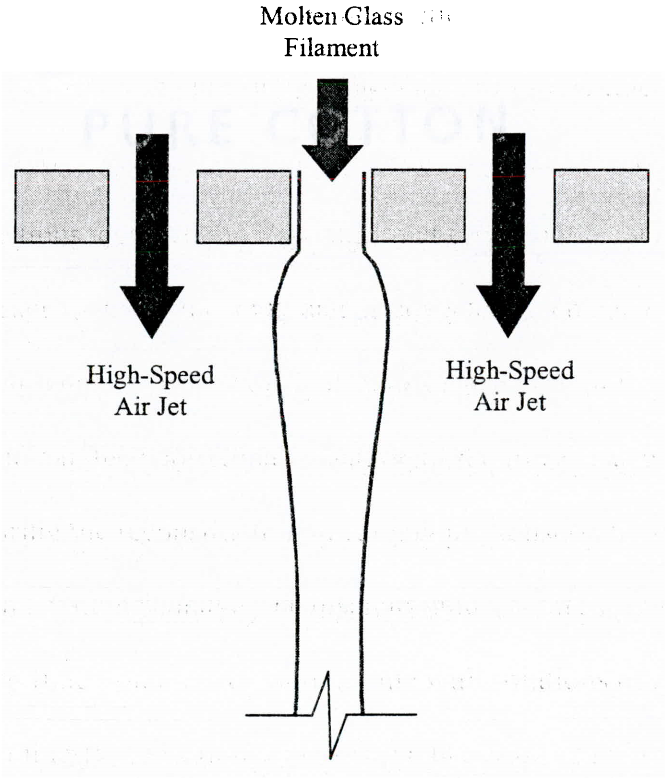

Figure 5.2 Extrusion of molten glass filament.

Considering the previously described issues, the specific objectives of the CFD model development were to

- provide a numerical tool to analyze critical process mechanisms and scenarios.
- provide a tool that can predict "localized" fiber attenuation, formation and diameter.
- initiate the development of numerical models for a complete and comprehensive fiberizing model that may be used as a versatile CFD code to build and expand upon.

Since the release of RIPPLE in 1991, significant progress has been made in the development of more robust solution techniques for solving the time dependent Navier-Stokes equations in fluid flows with large density variations (Rudman, 1998). The specific heuristics developed by Rudman (1998), Kothe *et. al.* (1998) and Brackbill *et. al.* (1991) enable the simulation of the flow of two immiscible fluids with variable density and viscosity. These improvements, in addition to the modifications needed to simulate fiber extrusion, have been integrated into Vi^3S-FLOW and are summarized in the following sections. The modifications to the original RIPPLE source code include the addition of a

- piece-wise linear interface calculation (PLIC) algorithm.
- two-fluid, incompressible variable density model.

- variable viscosity model with substantial modification to the viscous stress tensor.
- higher-order curvature calculation integral to the CSF model.
- 9-point pressure coefficient stencil used in the ICCG pressure solution algorithm.
- energy equation model to include conductive, convective and radiation heat transfer within the air/fiber system.

5.1 Interface Tracking Development

Simulating incompressible, free surface flows presents several challenges to the modeler. Three types of problems arise with the treatment of free surfaces. The first is accurately representing the continuous surface with a discrete technique, the second is tracking the evolution of the surface in time and lastly selecting the method by which boundary conditions are imposed (Hirt and Nichols, 1979). There exist two types of interface tracking schemes; Lagrangian and Eulerian. In a Lagrangian method the computational grid moves with the computed element velocities while in the Eulerian method the grid is stationary and it is necessary to determine the flow field through the computational mesh. Typically, Lagrangian and Eulerian formulations have been used with varying success depending on the problem. Some of the Lagrangian interface tracking schemes include the logically-connected Lagrangian point (LINC) technique (Hirt and Nichols, 1970), the marker and cell (MAC) scheme (Harlow and Welch, 1965) and the level set method (Sussman *et. al.* 1994). Level set methods provide acceptable results when the flow is simple (i.e. no folding of the interface) with the error primarily caused by the difference between the transfer function and the distance function. However, as the fluid body deforms the level set method experiences mass loss and decreased accuracy (Kothe, 1998). The LINC method also suffers from interfaces undergoing large deformation. The MAC method, which was developed prior to and is more stable than the other two methods, provides the simplicity of defining fluid regions rather than interfaces. The method has the distinct advantage of eliminating all logical problems associated with the intersection of surfaces (Hirt and Nichols, 1969). Although the MAC method offers the simplicity, it suffers from increased CPU run-time which is required to store and move the markers points to new locations.

A flexible, efficient method based on an Eulerian formulation, which is capable of modeling complex free surface configurations, is the volume-of-fluid (VOF) method developed by Hirt and Nichols (1979). The VOF method was developed to enable finite difference representation of free surfaces and interfaces that are arbitrarily oriented with respect to the computational grid. In the VOF method fluid volumes are initialized in each mesh cell from specific interface geometry. Fluid volumes are computed in each cell having an interface or free surface and exact interface data is discarded in favor of discrete volume data.

To avoid the difficulties and topological restrictions associated with Lagrangian models, free surfaces have been represented with VOF data on a mesh. The initial research of Harlow and Welch (1965), Hirt and Nichols (1979) and Noh and Woodward (1976) has provided the basis for more recent advances of the Piece-wise Linear Interface Calculation (PLIC) scheme (Young, 1982 and Kothe and Rider, 1998) and FLAIR: the Flux line-segment model (Ashgriz and Poo, 1991) for advection and interface reconstruction within the VOF method. Despite the VOF technique, Eulerian methods require the integration and implementation of an accurate free surface reconstruction algorithm compute the flux volumes needed for the advection of fluid within the computational mesh (Kothe and Mjolsness, 1991).

In the VOF method, fluid volumes must be computed in each mixed cell that contains an interface. Mixed cells have volume fractions between zero and one. The remainder of cells that do not include an interface have a volume fraction of one (i.e. entirely fluid) or zero (i.e. void). Given that the fluid free surface has been replaced with discrete volume fractions, detailed interface information cannot be obtained until the interface is reconstructed. Once the VOF data is advected, each computational cell possesses a specified volume fraction of fluid. The distribution of the fluid volume within each cell results in the approximate location of the free surface (or interface in the two fluid case). During the reconstruction, local volume conservation is obtained by truncating cells with a volume equal to the discrete fluid volumes. Fluid interfaces are tracked by advecting fluid volumes forward in time with solutions of an advection equation. The exact interface location is not known but must be inferred based on volume data. The reconstructed interface is then used to compute the successive volume fluxes for further advection steps.

Historically there have been three basic VOF interface reconstruction methods used: piece-wise linear methods (DeBar, 1974), piece-wise constant/stair stepped VOF approximations (Hirt and Nichols, 1979) and piece-wise constant or simple line interface calculation (SLIC) method (Noh and Woodward, 1976). Recently, a piece-wise parabolic interface calculation (PPIC) algorithm has been developed (Price *et. al.,* 1999). The PPIC method replaces sloped line segments used for reconstruction by the PLIC method and implements a piece-wise parabolic curve within each computational cell to reconstruct the fluid free surface. The PPIC method increases the spatial accuracy of volume tracking methods to third-order and diminishes numerical surface tension effects by allowing two interfaces to coexist in the same computational cell (Price, *et. al.,* 1999). Initial results on a small range of test cases show favorable results compared to other interface tracking routines, however the improvements come at a cost of increased CPU time and algorithm complexity. Until further development and testing has been completed, the PLIC algorithm will be implemented into RIPPLE rather than the PPIC method.

5.1.1 Piece-wise Constant Volume Tracking Method

The approximate reconstruction of the free surface is needed for the advection of fluid from donor to acceptor cell in the VOF method. A much more robust interface tracking algorithm is the PLIC method. Curvature, a second order moment and a principal variable in the VOF calculation, can introduce large errors from small volume fraction discrepancies. Thus, the PLIC algorithm is more desirable as it ensures more accurate results.

Volume tracking methods were advanced significantly by the piece-wise linear scheme of Young (1982). Young's novel approach positioned and reconstructed each interface line, defined by a slope and intercept, within the controlling volume or cell. In Young's method the slope of the line is given by the interface normal (gradient of volume fractions), and the intercept follows from invoking volume conservation. There have been many schemes that have been based upon Young's work. The piece-wise linear interface calculation (PLIC), developed by Kothe and Rider (1998) is based on Young's research and forms the basis of the discussion and results that follow. The following discussion is an overview of the detailed research completed by Kothe and Rider (1998). For a more complete discussion of the procedure summarized herein see Kothe and Rider (1998).

It should be noted that despite the notable improvements offered by the PLIC method and its contemporary, the FLAIR method, variations of the piece-wise constant method and piece-wise constant stair-step method have remained in widespread use due to the ease of implementation.

5.1.2 Fluid Volume Equations

The governing volume equations must be developed prior to the presentation of the PLIC method. Those volume equations are derived below. The volume (V_k) of the material (k) is given as

$$V_k = \int \alpha_k(V)dV \tag{5.1}$$

where $\alpha_k(V)$ is an indicator function given by

$$\alpha_k(V) = 1, \quad \text{if the fluid is present} \tag{5.2}$$

$$0, \quad \text{otherwise}$$

The volume fraction, F_k is given as

$$F_k = \frac{V_k}{V} \tag{5.3}$$

And the total volume (V) is the sum of the volume fractions given as

$$V = \sum_k V_k \tag{5.4}$$

Given a flow field velocity of U, the advection equation that governs the evolution of F is

$$\frac{\partial F}{\partial t} + U \cdot \nabla F = 0 \tag{5.5}$$

In general, Equation 5.5 is a standard advection equation where F may represent any arbitrary scalar value. The equation also indicates that material volumes must remain constant along a streamline. Invoking incompressibility ($\nabla \cdot U=0$), equation 5.5 can be expressed as a conservation law (Kothe and Rider, 1998).

5.1.3 PLIC Method of Solution

In the PLIC algorithm, an interface line segment that partitions each cell containing a free surface into the appropriate volume fraction forms material volumes consisting of n-sided polygons. These material volumes pass through the total volume flux polygons and are referred to as the material fluxed volumes. The fluxed volumes are determined using a heuristic that can be applied to almost any flow field, thus avoiding a case-by-case assessment. The heuristic is condensed into a "geometric toolbox" (i.e. a step-by-step method) developed by Kothe and Rider (1998). Within the geometric toolbox, the two dimensional PLIC method requires the following functions.

1. Line-line intersection
2. Point location
3. Polygon collection
4. Polygon area.

As an example, assume that a line is defined by the equation shown below

$$m \cdot x + \rho = 0 \tag{5.6}$$

where m is the slope of the line, x is a point on the line and ρ is the line constant. In the PLIC method, any cell possessing a volume fraction between one and zero will have an interface that is defined by equation (5.6). Within each cell the line divides the cell into regions of fluid and void. The direction of n may be oriented into or out of the fluid. In this case we will assume that n is directed into the fluid. Thus, n will be positive if pointing into the fluid, zero if on the interface line and negative when pointing into the void. The line-line intersection algorithm locates the point of intersection between two lines, namely the interface line and the cell edge. The second function of the toolbox is the point location function, which locates points inside the fluid. The function is needed to determine which of the cell vertices are located inside of the fluid polygon. The polygon collection function collects the vertices of an n-sided polygon in counterclockwise order. The function collects those vertices lying within the fluid and bounded by the interface line (see Figure 5.2). The polygon area function takes the vertices that have been identified in the direction of n and computes the area enclosed by the polygon.

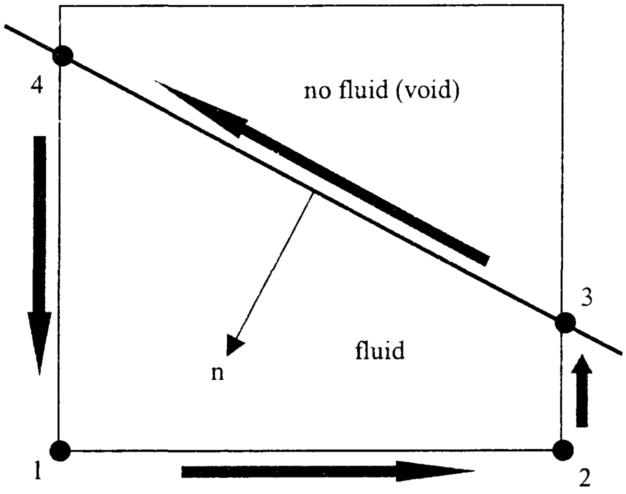

Figure 5.3. Geometric toolbox representation.
Line-line intersection, point location, polygon collection and polygon area.

5.1.4 Reconstructing the Interface

Linear interface line segments must be reconstructed in each cell using the interface reconstruction steps outlined in the geometric toolbox. For each segment the line equation (5.6) must be defined, which means that the inward normal (n) and the line constant (ρ) must be determined. The line constant is derived from conservation of volume and the line normal follows from volume fraction gradients. The value of ρ is constrained by volume conservation of each cell. The line constant, defined by the passing of the intersection line through the cell, must satisfy the constraint that the truncation volume equals the cell material volume (V). The line constant (ρ) is found when the generally nonlinear function

$$f(\rho) = V(\rho) - V \tag{5.7}$$

becomes zero. $V(\rho)$ is the material volume in the cell bounded by the interface segment and the portion of the cell edges within the material. When the two volumes are equal within some error term (ε), the interface is assumed to be reconstructed. There are any number of root finding techniques to determine the zero of this function, such as Newton's or Brent's method. To avoid taking the derivative of V, which is required by Newton's method, Brent's method is employed. The interface reconstruction template is summarized in the following steps.

1. Given an interface reconstruction line segment, truncate the mixed cell.
2. Find the vertices of the polygon inside the fluid defined by the interface line segment and the cell vertices.
3. Compute the volume bounded by this polygon.
4. Does the polygon volume differ from the known volume by more than a given error (ε).
5. If the volumes differ, use Brent's method to find a new estimate for ρ and return to step one.
6. If the volumes are within the margin of error the interface has been reconstructed.

5.1.5 Material Volume Fluxes

The next step of the PLIC method requires determination of material volume fluxes through each cell face. The material volume flux, δV, represent the volume of material passing through a given face during the current time step. The sum of all material volume fluxes must equal the total volume flux of each face. To compute the flux volume the following two steps are required.

1. The polygon bounding the volume swept by the velocity field over the time step must be constructed.
2. The amount of material k must be found for these polygons.

The algorithm needed to accomplish the second step have been discussed in the previous section but the first step must be defined in more detail.

It is now appropriate to define the operator split and unsplit time integration techniques. The operators split method constructs the solution in a series of one-dimensional sweeps. In the unsplit method the flow is considered to be completely multidimensional. Figure 5.4 illustrates both the split and unsplit methods. For operator-split integration, an x-direction sweep is made in (a) followed by a y-direction sweep in (b). A naive unsplit method shown in (c) is not recommended because face adjacent polygons overlap, hindering conservative, monotonic volume advection. In the unsplit method of (d) polygons are constructed by tracing along upwinded characteristics which yield multidimensional, corner coupled fluxing of material volumes (Kothe and Rider, 1998).

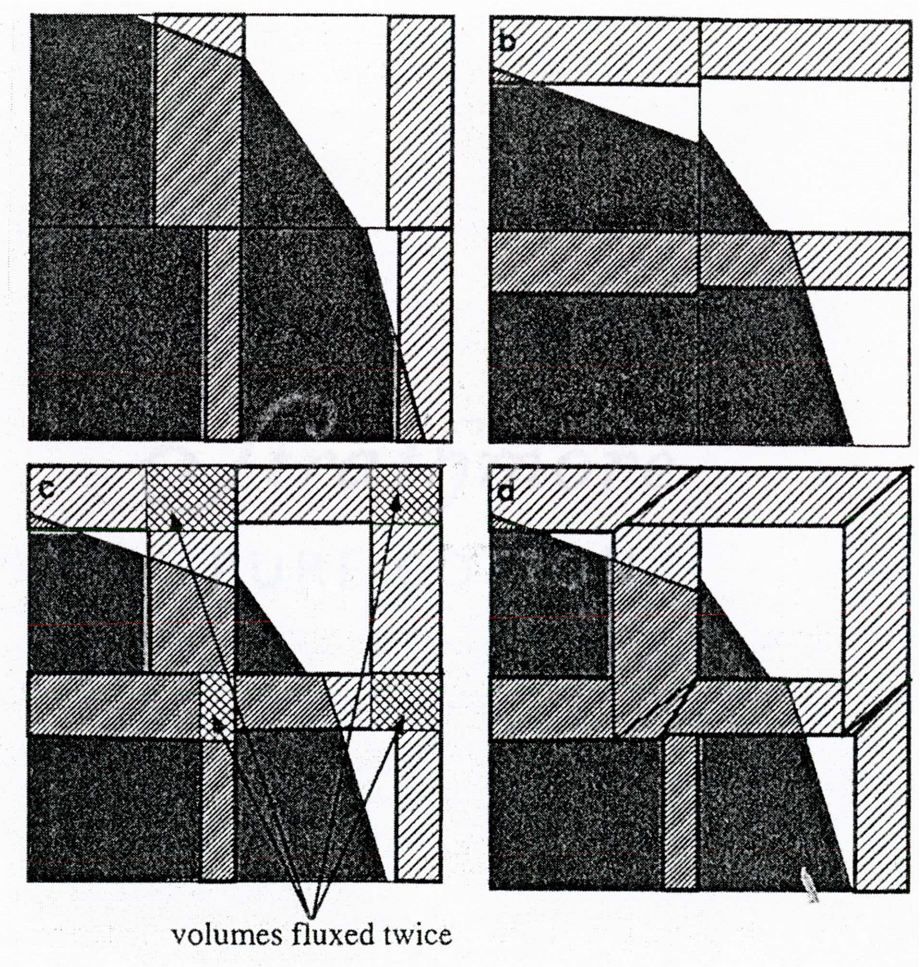

Figure 5.4. Face volume fluxes and bounding polygons for three types of time-integration schemes in two dimensions. In (a) a x-direction sweep of the operator split method, in (b) a y-direction sweep of the operator split method, in (c) a naive multidimensional unsplit method and in (d) an unsplit multidimensional method with corner flux correction.

The following two examples illustrate the split and unsplit techniques on a two-dimensional computational mesh.

Split Algorithm

The operator split time integration technique constructs the solution in a series of one-dimensional sweeps in the x and y directions. As an example, consider a single sweep in the x direction of the cell in Figure 5.5. The interface reconstruction has been completed, resulting in a volume of material that is to be fluxed in the x direction through the right face of the cell. The first step requires that the vertices of the edge being evaluated must be identified. In this case the cell edge 2 (located at i+1/2,j) is chosen, where (i,j) corresponds to the center of the cell. Next the velocity normal to this edge (U_n) and the time step (Δt) are chosen enabling the determination of the final two vertices of the flux volume. It is this material flux volume that is advected across the cell wall in the time integration step.

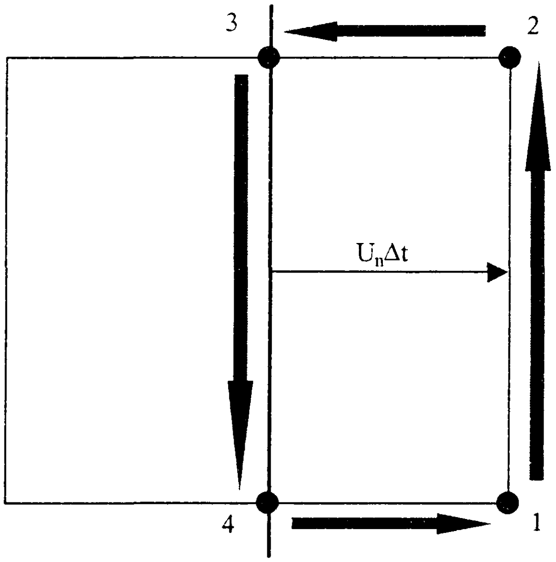

Figure 5.5. Split material volume flux.

Unsplit Algorithm

The unsplit algorithm is similar to the split method, however it requires that correction be made to the material flux volumes. The corrections are necessary so that overlapping does not occur near the edges of the cell when both *x* and *y* sweeps are completed. The corner correction uses the velocity traverse to the direction of the edge under consideration. This velocity is upwind differenced resulting in the normal edge velocity. The corner edge correction algorithm identifies the vertex of the corner being evaluated. This is the first vertex in the flux polygon. The next vertex is identified using the velocity normal to this edge and the time step. The final vertex is found using the upwinded transverse velocity at the corner edge. The algorithm for the upper right corner edge is illustrated in Figure 5.6.

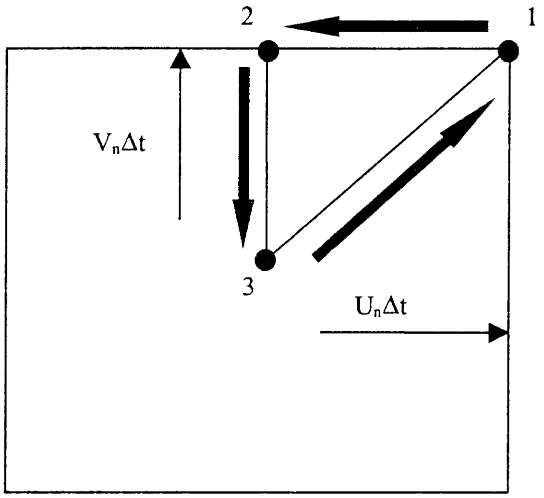

Figure 5.6. Split material volume flux corner correction.

In this example, the unsplit algorithm applies the edge flux method to the selected polygon. Then the corner flux correction is applied at the cell's upper right vertex. If the upwinded transverse velocity is positive, subtract the corner flux volume; otherwise add it. The corner flux correction is then applied at the lower right vertex. If the upwinded transverse velocity at the vertex is positive add the corner flux volume; otherwise subtract it.

5.1.6 Time integration

The time integration takes material (*k*) volume fractions $F^{k,n}$ at the discrete time level n and moves them forward in time to step $n+1$. The material volumes (V_k) must sum to the total cell volume. A global filling constraint also applies. Material volumes summed over the entire mesh must be conserved.

Kothe and Rider (1998) insist that a key point in the time iteration scheme for the incompressible flow volume evolution equations is the recognition that discrete velocity divergences are not necessarily zero, but rather a function of the convergence tolerance used in obtaining the linear system solutions. As a result, the divergence correction, $\nabla \cdot u$ is added to both sides of equation (5.8)

$$\frac{\partial F}{\partial t} + \nabla \cdot (uF) = F\nabla \cdot u \tag{5.8}$$

Applying the divergence correction globally the volume-filling constraint is satisfied more strictly. Equation 5.8 is then integrated forward in time to advance the volume fraction (*F*).

The time integration method operates on two different types of cells; those that are mixed (i.e. contain a fluid interface) and those that are active. The mixed cells are determined according to the following

1. The volume fractions F satisfy $\varepsilon \leq F \leq 1-\varepsilon$, or

2. The volume fractions F satisfy $F > 1 - \varepsilon$, and a face is shared with an empty cell having $F < \varepsilon$.

Active cells are flagged if at least one cell in the domain of dependence is mixed. In a two-dimensional scheme, the domain of dependence for operator-split time integration is three cells along the current sweep direction. A 3 x 3 array of cells is used for the unsplit time integration. The error term (ε) is small, usually 1×10^{-12}.

Using an operator split time integration scheme, equation 5.8 must be integrated twice in two dimensions, once for a sweep in the x direction and once in the y direction. Sweep direction is alternated every time step to minimize asymmetries induced by the sweeping process.

Operator Split Time Integration Algorithm

In summary the operator split time integration procedure is given as

1. Flag all mixed, active and isolated cells.
2. Compute the velocity divergence ($\nabla \cdot u$) in each flagged cell.
3. Reconstruct all interfaces in mixed cells.
4. Compute edge volume fluxes (δV) in all flagged cells.
5. Advance volume fractions in time.
6. Look for and redistribute any volume fraction undershoots ($F \leq 0$) or overshoots ($F \geq 1$).

The unsplit time integration technique advances volume fractions with one equation given for two dimensions and employs the unsplit edge correction method.

The implementation of the PLIC algorithm was tested using a solid body rotation and capillary jet break-up test case (see section 6.1).

5.2 Two Fluid Development

RIPPLE, originally a one fluid code, has been modified to include a second fluid. The VOF method, originally developed by Hirt and Nichols (1981), which RIPPLE is based upon, lends itself nicely to simulating a two fluid interaction as well as the critical interaction that occurs at the interface.

The original version of RIPPLE defined *F* according to

$$F(x,y,t) = \begin{cases} 1, & \text{in the fluid} \\ > 0, < 1, & \text{at the interface} \\ 0, & \text{in the void} \end{cases} \tag{5.9}$$

An interface reconstruction algorithm is applied to those cells possessing $0<F<1$, which are referred to as interface cells. From this reconstructed interface, a donor-acceptor method is used to determine the appropriate volume fraction that must be advected in the x and y directions. The momentum advection is based on a VOF weighted density given as

$$\rho(i,j) = \rho(i,j) \cdot F(i,j) \tag{5.10}$$

In the original RIPPLE source code, solutions to the Navier-Stokes equations and advection of the VOF function are applied everywhere for computational cells satisfying $F>0$. The solutions to the governing flow equations are disregarded in the void. The addition of a second fluid required the flow solutions everywhere within the domain, including the void, which is subsequently defined as the second fluid in the two fluid model. The new VOF function is defined as

$$F(x,y,t) = \begin{cases} 1, & \text{in fluid \#1} \\ >0, <1, & \text{at the interface} \\ 0, & \text{in fluid \#2} \end{cases} \tag{5.11}$$

The process of adding a second fluid (i.e. formerly void) to the original source code required a slight modification to the solution algorithm. The original one fluid version of RIPPLE solved the governing equations over the entire domain regardless of the computational cell type (i.e. fluid, void, surface or obstacle), but discarded the solution in void and obstacle cells. In the two fluid model, the solutions to the governing equations would only be discarded in cells defined as obstacles. The modified two fluid model weights the VOF function by the average density within each computational cell. The method used to implement this was an average density function based on the VOF function given as

$$\rho(i,j) = F(i,j) \cdot \rho_{fluid1} + (1 - F(i,j)) \cdot \rho_{fluid2} \tag{5.12}$$

As the equation indicates, for a cell with $F=1$ (i.e. entirely fluid #1) the average density corresponds to the density of fluid #1. Similarly, for a cell with $F=0$ (i.e. entirely fluid #2 or formerly void) the average density corresponds to the density of fluid #2. The more critical case occurs in an interface cell where $0<F<1$. The resulting average density of the cell is the density weighted volume fraction of fluid #1 and fluid #2. Momentum advection along each cell edge in the x and y directions is accomplished using the average density of the fluid, as shown in equation 5.12.

The development of the variable density, two-fluid model enables the simulation of a two-phase flow field, which is required to accurately simulate the industrial process. The modifications to the source code were validated using Rayleigh-Taylor and pipe flow test cases that examined the interaction between two different fluids of variable density. (see Sections 7.2 and 7.3)

5.3 Continuum Surface Force Development

RIPPLE implements the CSF method to model surface tension at free surfaces (or at the interface in a two fluid case). The CSF model reformulates the surface tension force as a volume force that acts on fluid elements within a transition region across the interface (see Appendix A, Section A.9). The CSF method is quite different from earlier methods that relied on an exact reconstruction of the fluid interface and the application of a surface pressure boundary condition which represents a jump or discontinuity between the two fluids.

The exact surface stress boundary conditions at the fluid free surface can be written in terms of the normal and tangential components given by

$$\left(\tau_{1,nn} - p_1\right) = \left(\tau_{2,nn} - p_2\right) + \sigma\kappa \tag{5.13}$$

$$\tau_{1,nt} = \tau_{2,nt} + \frac{\partial \sigma}{\partial s} \tag{5.14}$$

where σ is the fluid surface tension coefficient, p is the pressure, κ is the local free surface curvature, n is the unit normal to the surface and s is the arc length tangent to the surface.

In the original one fluid, RIPPLE source code, viscous effects are neglected in fluid 1 (see equation 5.13) and the surface tension coefficient is assumed to be constant which reduces the normal stress boundary condition to Laplace's formula given by

$$p_1 - p_2 = \sigma\kappa \tag{5.15}$$

where the p_1-p_2 is the surface tension induced pressure jump across the fluid interface. A re-formulation of Laplace's equation into a volume force is used in the continuum surface force (CSF) model developed by Brackbill *et. al.* (1992). In the CSF model, surface tension is reformulated as a volume force (body force) given as

$$F_b = \sigma\kappa(\bar{x})\nabla F(\bar{x}) \tag{5.16}$$

The original CSF model, developed by Brackbill *et. al.* (1992) has been modified to include a variable viscosity, viscous stress tensor and an improved method for determining interfacial surface curvature (κ).

5.3.1 Viscous Stress Tensor Development

Glass viscosity rapidly changes as a function of temperature. The importance of viscosity in the attenuation of the molten glass is of tremendous interest in industrial fiberizing processes. In order to formulate an accurate model, the addition of a variable viscosity term must be added to the current code. Glass, which is an amorphous solid, does not experience a phase change. Thus, there will be no solidification model included in the code development and inferences regarding the glass material state will depend on the change in the viscosity of the glass as a function of temperature and position within the fiber. It is hypothesized that the molten glass filaments do not undergo solidification but experience a rapid change in viscosity. Thus, accurately characterizing the glass viscosity is of paramount interest to predicting localized fiber attenuation, necking and ultimately fiber formation.

In the two fluid development, a variable viscosity, viscous stress tensor is required to properly simulate the interaction between two fluids at the interface. Like the variable density model, the variable viscosity model uses a VOF weighted, cell centered viscosity given as

$$\mu(i,j) = F(i,j)\cdot\mu_{fluid1} + (1 - F(i,j))\cdot\mu_{fluid2} \tag{5.17}$$

As the equation indicates, for a cell with $F=1$ (i.e. entirely fluid #1) the average viscosity corresponds to the viscosity of fluid #1. Similarly, for a cell with $F=0$ (i.e. entirely fluid #2 or formerly void) the average viscosity corresponds to the viscosity of fluid #2. The more critical case occurs in an interface cell when $0<F<1$. The resulting average viscosity of the cell is the viscosity weighted volume fraction of fluid #1 and fluid #2.

The viscous term in the momentum equations is written in the stress divergence form to allow for variable viscosity. The harmonic average of the viscosity at each computational cell edge (for example, the harmonic average at the cell edge $(i+1/2,j+1/2)$ is shown in Figure 5.7 and is given as

$$\mu_{harmonic}(i+1/2, j+1/2) = \frac{2\mu^{+}\mu^{-}}{\mu^{+}+\mu^{-}} \tag{5.18}$$

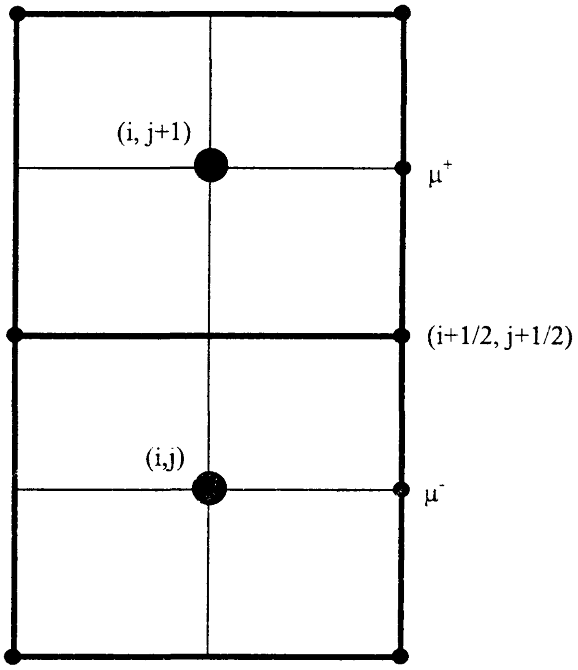

Figure 5.7. Harmonic average for the cell edge *(i+1/2, j+1/2)* on a standard computational mesh.

The upper (μ^{+}) and lower (μ^{+}) cell face viscosities are defined as the arithmetic average between cell centered viscosities of neighboring cells, such that

$$\mu^{+} = \frac{1}{2}\left(\mu_{i,j+1} + \mu_{i+1,j+1}\right) \tag{5.19}$$

$$\mu^{-} = \frac{1}{2}\left(\mu_{i,j} + \mu_{i+1,j}\right) \tag{5.20}$$

In a two fluid formulation, arithmetic averaging of the viscosity between successive cells may produce less accurate results if the cell viscosities are significantly different, resulting in large viscosity gradients. Rudman (1998) insists that harmonic averaging is essential to ensure that fluid stresses do not give rise to excessive accelerations in the less dense, less viscous fluid near the interface.

As shown in Appendix A, section A.9, the one fluid version of RIPPPLE originally implemented a constant surface tension force (or normal force component) at the fluid free surface by assuming the fluid was incompressible and inviscid ($\mu=0$). The viscosity of the void was identically zero in order for the normal and tangential boundary conditions to balance at the free surface. In short, at the free surface the viscosity of the fluid and the void are identically zero. As a result, the pressure jump ($p1-p2$) (see equation 5.13) was balanced by the normal surface tension force (σ), which occurs at the fluid free surface. The tangential condition given in equation 5.14 was applied as a boundary condition at the fluid interface, and both the normal and tangential conditions were satisfied in the one fluid case.

A hypothetical scenario may include two immiscible fluids with identical fluid properties. At the interface between the two fluids, a change in surface tension or pressure jump does not occur between two fluids that possess identical fluid properties.

Thus, the normal (see equation 5.13) and tangential (see equation 5.14) boundary conditions are inherently satisfied.

An example similar to this may be a fixed volume of fluid subject to large temperature gradients. The thermal gradients, which strongly influence viscosity, cause the single fluid with variable viscosity to act similarly to two dissimilar fluids with different viscosities. In both cases the surface tension and shear stress conditions are satisfied in both fluids by applying equations 5.13 and 5.14.

The original formulation of the stress tensor routine (see equation 5.21) neglected the radial component, $\tau_{\theta\theta}$, which is shown in equation 5.22.

$$\nabla \cdot \tau = \left[\frac{1}{r^{\delta}} \frac{\partial}{\partial r} \left(r^{\delta} \tau_{rr} \right) + \frac{\partial \tau_{rz}}{\partial z} \right] i + \left[\frac{1}{r^{\delta}} \frac{\partial}{\partial r} \left(r^{\delta} \tau_{rz} \right) + \frac{\partial \tau_{zz}}{\partial z} \right] j \tag{5.21}$$

$$\tau_{\theta\theta} = -\mu \left[2 \left(\frac{1}{r} \frac{\partial v_{\theta}}{\partial \theta} + \frac{v_r}{r} \right) - \frac{2}{3} (\nabla \cdot v) \right] \tag{5.22}$$

In the axisymmetric case, each term in equation 5.22 is neglected except $\tau_{\theta\theta}$, which is equal to v_r/r. The revised viscous stress tensor is given as

$$\nabla \cdot \tau = \left[\frac{1}{r^{\delta}} \frac{\partial}{\partial r} \left(r^{\delta} \tau_{rr} \right) + \frac{\partial \tau_{rz}}{\partial z} + \frac{v_r}{r^{2 \cdot \delta}} \right] i + \left[\frac{1}{r^{\delta}} \frac{\partial}{\partial r} \left(r^{\delta} \tau_{rz} \right) + \frac{\partial \tau_{zz}}{\partial z} \right] j \tag{5.23}$$

5.3.2 Smoothing Kernel Development

In the continuum surface force model, forces resulting from interfacial surface tension are written as a surface volume force. This body force is given by equation 5.24 (see Appendix A, section A.9)

$$F_{sv} = \sigma\kappa(\bar{x})\nabla F(\bar{x}) \tag{5.24}$$

where σ, is the surface tension coefficient, κ is the surface curvature and F is the volume-of-fluid (VOF) function. RIPPLE calculates the free surface curvature using 4 cell vertices (see Appendix A, section A.9). In the modified CSF model, a cubic B-spline is used to smooth the VOF gradient (∇F) over an "n" point stencil given by

$$K(r,h) = \begin{cases} \left(\frac{1}{h^2}\right)\left(\frac{40}{7\pi}\right)\left[1-6\left(\frac{r}{h}\right)^2+6\left(\frac{r}{h}\right)^3\right] & \text{if } r < h/2 \\ \left(\frac{1}{h^2}\right)\left(\frac{80}{7\pi}\right)\left(\left[1-\frac{r}{h}\right]^3\right) & \text{if } r < h \\ 0 & \text{otherwise} \end{cases} \tag{5.25}$$

where r is the radius from cell (i,j) to the n^{th} cell of the stencil, predetermined by the smoothing length, h. A plot of the smoothing kernel is shown in Figure 5.8. The smoothing length is 5μm. Figure 5.8 depicts only one-half of the smoothing kernel, which in fact continues in both *x* and *y* (or *r* and *z*) directions from each computational cell.

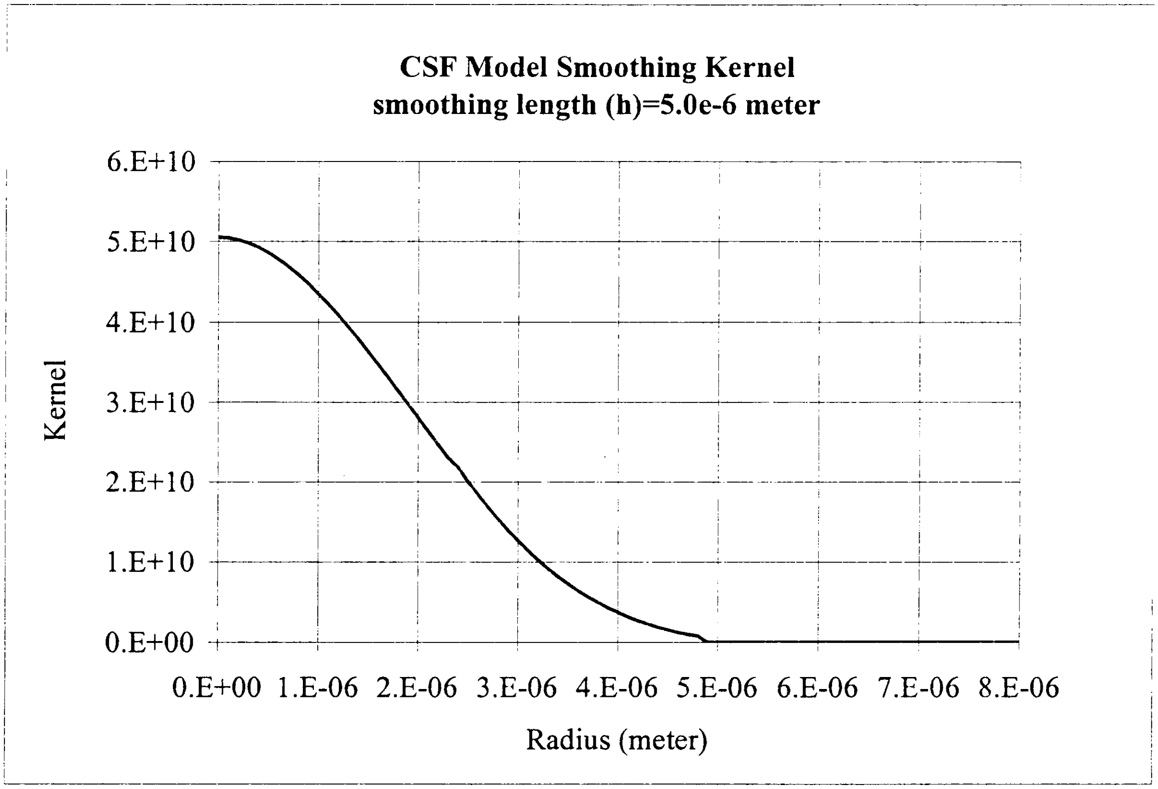

Figure 5.8. CSF smoothing kernel.

The size of the stencil may vary depending on the value of the smoothing length, *h*. A typical smoothing length is approximately two times the minimum grid spacing (Rudman, 1990). The kernel provided by Rudman (1990) defines a smoothed VOF function (F_{tilde}) that varies between zero and one at the interface and is zero everywhere else in the domain, which is consistent with the smoothing kernel's delta function. The result is a body force (F_{sv}) added to the Navier-Stokes equations that represents the surface tension at the fluid interface.

The implementation of the continuum surface force model (i.e. the modified viscous stress tensor, harmonic averaging and smoothing kernel) was validated using a static droplet test case discussed in detail in Section 6.4.

5.4 Pressure Poisson Equation Development

The coupled solution of the continuity and momentum equations is solved using a two-step projection method as discussed in Appendix A, section A.7. The PPE, mapped from physical coordinates (x,y) to computational coordinates (ξ, η), is given as

$$\nabla \cdot \left(\frac{1}{\rho} \nabla p^{n=1} \right) = \frac{1}{Jr^{\delta}} \left[\left(\frac{r^{\delta} \alpha}{\rho} \right) p_{\xi}^{n+1} - \left(\frac{r^{\delta} \beta}{\rho} \right) p_{\eta}^{n+1} \right]_{\xi} + \frac{1}{Jr^{\delta}} \left[\left(\frac{r^{\delta} \gamma}{\rho} \right) p_{\eta}^{n+1} - \left(\frac{r^{\delta} \beta}{\rho} \right) p_{\xi}^{n+1} \right]_{\eta} \tag{5.26}$$

where δ is defined as 1 in cylindrical and 0 in Cartesian geometry and the derivatives are shown using Einstein's notation. The coordinate transformation employs metrics to simplify the notation, where the Jacobian (J) is defined as

$$J = x_{\xi} y_{\eta} - x_{\eta} y_{\xi} \tag{5.27}$$

and the geometric coefficients are given as

$$\alpha = \frac{1}{J}\left(x_\eta^2 + y_\eta^2\right) \tag{5.28}$$

$$\beta = \frac{1}{J}\left(x_\xi x_\eta + y_\xi y_\eta\right) \tag{5.29}$$

$$\gamma = \frac{1}{J}\left(x_\xi^2 + y_\xi^2\right) \tag{5.30}$$

The PPE was transformed from physical (x,y) to computational (ξ, η) coordinates using the coordinate transformations described by Brackbill and Saltzman (1981) and Anderson (1995). A majority of real-world CFD problems involve complex geometries that require adaptive mesh schemes aimed at refining the mesh in critical flow regions. One such example may be the flow over a swept wing. It is more desirable to locate more closely packed grid points near the curved surface of the wing where the velocity gradients are the largest. The increased grid resolution ensures proper determination of the velocity gradient in the critical flow region. However, increasing the number of computational cells within a specified region often results in a physical grid that may contain a number of cells that are highly distorted and skewed. A coordinate transformation is usually employed to convert a non-uniform grid in the physical plane to a uniform grid in the computational plane. Brackbill and Saltzman (1982) provide numerous examples of transforming highly distorted computational grids into less skewed, more desirable (nearly orthogonal) computational grids. Simulating the extrusion of a glass fiber is one such case where adaptive mesh routines would be advantageous in accurately resolving large numerical gradients near the fluid interface or radially as the fiber rapidly attenuates. However, adaptive mesh schemes are beyond the scope of this research. The transformation of the PPE equation from a physical to a computational domain has been included and provides the basis for future mesh generation refinement. All simulations completed during the course of the research have been carried out on an orthogonal mesh, thus negating the need for a grid transformation. Inherent to an orthogonal mesh, the cross derivatives (x_η and y_ξ) are zero and upon substitution into equations 5.27-5.30, the Jacobian and geometric coefficients become

$$J = x_\xi y_\eta \tag{5.31}$$

$$\beta = 0 \tag{5.32}$$

$$\alpha = \frac{y_\eta^2}{J} \tag{5.33}$$

$$\gamma = \frac{x_\xi^2}{J} \tag{5.34}$$

Once transformed, the coupled set of equations is solved over the entire domain using an incomplete Cholesky conjugate gradient (ICCG) method. In the original, one fluid, version of RIPPLE, the ICCG routine was applied using an 9-point stencil on an orthogonal mesh. The time $n+1$ pressure was determined from the solution to the system of equations given by

$$[M]\{p^{n+1}\}=\{S\} \tag{5.35}$$

where S is the solution vector. The pressure coefficients (A,B,C etc.), shown in Figure 5.8, and given in terms of the geometric coefficients α, β, and γ make-up the matrix $[M]$. The cross derivatives, represented by β (see equation 5.29), and the corner cell coefficients (C, E, CF and EF) are identically zero due to the orthogonality of the mesh. However, coefficients, α and γ remain as multipliers in matrix $[M]$ for each of the five remaining pressure terms in $\{p^{n+1}\}$.

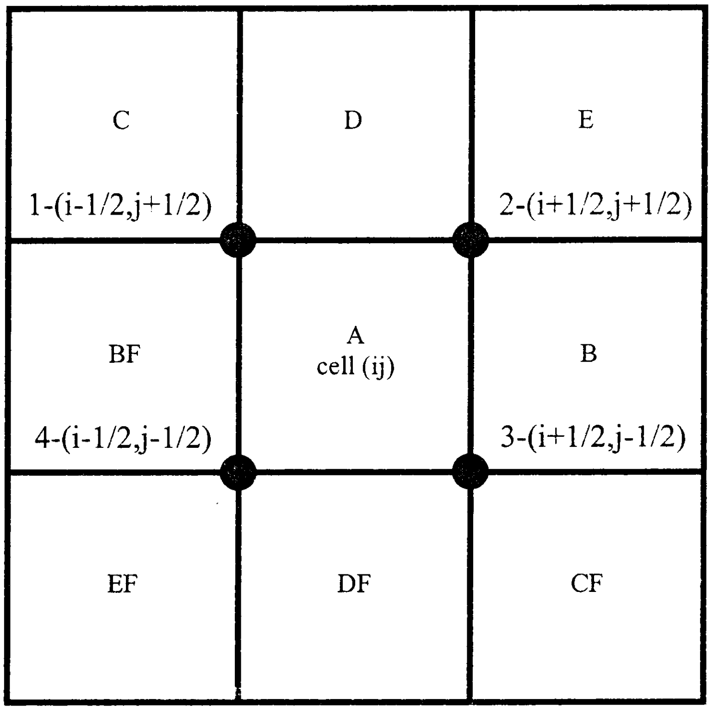

Figure 5.9 Computational pressure cell template.

The orthogonality of the computational mesh reduces the original 9-point template to a 5-point template, which consists of cells A, B, BF, D and DF. The resulting pressure stencil uses fewer cells, than the original 9-point stencil, to cover the same effective area. This is not a concern if the computational cell (*i,j*) and surrounding neighbors (A, B, BF, D and DF) lie completely within fluid one or two. However, if the computation cell is an interface cell or near a boundary or obstacle, using fewer cells may lead to inaccurately biasing the geometric coefficients toward the more dense fluid. Thus, the pressure stencil was recast to extend the calculation template over a larger number of cells to counter the possibility of excessive gradients. However, a trade-off exists when implementing a larger template. Although a larger template may be more robust by averaging over a larger number of cells to smooth any sharp numerical gradients, the larger template also introduces additional numerical diffusion into the model.

The original 5-point template worked well in the one fluid case, however the same template in the two fluid case resulted in numerous pressure convergence failures. In several of the pipe flow simulations (see Section 6.3) the ICCG routine would attain a converged solution using only a large pressure residual (on the order of 10^{-2}). A pressure residual greater than 10^{-2} resulted in convergence failures. Ideally, the code should reach a converged solution with a pressure residual on the order of at least 10^{-6}. Following several attempts to improve the convergence, it was determined that the discretization of the PPE needed to be reformulated in terms of the geometric coefficients α and γ to include all nine computational cells.

The first step in the discretization procedure utilized a second-order polynomial to derive an expression for the pressure gradient (Δp) at cell A (see Figure 5.8). The resulting gradients (dp/dx and dp/dy) consisted of points 1, 2, 3 and 4, which are located at cell vertices $(i-1/2, j+1/2)$, $(i+1/2, j+1/2)$, $(i+1/2, j-1/2)$ and $(i-1/2, j-1/2)$. However, RIPPLE's finite difference scheme only determines cell centered values of pressure, density, viscosity and the VOF function. The determination of those particular cell edge values would require additional averaging which would only introduce additional numerical diffusion. Therefor, the a second discretization step, identical to the first step, was applied at each of the four cell vertices. For example, the gradient for vertex 2, located at *(i-1/2, j+1/2)*, was determined using cells C, D BF and A. The same process was completed for the remaining three vertices. The end result, following extensive algebraic manipulation, was a 9-point template defined in terms of α and γ on an orthogonal mesh. The final form of the newly discretized PPE is given as

$$\begin{aligned}
\nabla\cdot\left(\frac{1}{\rho}\nabla p^{n=1}\right) &= \frac{1}{J_{ij}r_{ij}^{\delta}}\Biggl\{\Biggl[\left(\frac{r^{\delta}\alpha}{\rho}\right)_{i+\frac{1}{2},j+\frac{1}{2}}\left(\frac{p_{ipjp}-p_{ijp}+p_{ipj}-p_{ij}}{16h^{2}}\right)\Biggr]- \\
&\Biggl[\left(\frac{r^{\delta}\alpha}{\rho}\right)_{i-\frac{1}{2},j+\frac{1}{2}}\left(\frac{p_{ijp}-p_{imjp}+p_{ij}-p_{imj}}{16h^{2}}\right)\Biggr]+\Biggl[\left(\frac{r^{\delta}\alpha}{\rho}\right)_{i+\frac{1}{2},j-\frac{1}{2}}\left(\frac{p_{ipj}-p_{ij}+p_{ipjm}-p_{ijm}}{16h^{2}}\right)\Biggr]- \\
&\Biggl[\left(\frac{r^{\delta}\alpha}{\rho}\right)_{i-\frac{1}{2},j-\frac{1}{2}}\left(\frac{p_{ij}-p_{imj}+p_{ijm}-p_{imjm}}{16h^{2}}\right)\Biggr]\Biggr\}_{\xi}+ \\
&\frac{1}{J_{ij}r_{ij}^{\delta}}\Biggl\{\Biggl[\left(\frac{r^{\delta}\gamma}{\rho}\right)_{i+\frac{1}{2},j+\frac{1}{2}}\left(\frac{p_{ipjp}-p_{ipj}+p_{ijp}-p_{ij}}{16h^{2}}\right)\Biggr]- \\
&\Biggl[\left(\frac{r^{\delta}\gamma}{\rho}\right)_{i+\frac{1}{2},j-\frac{1}{2}}\left(\frac{p_{ipj}-p_{ipjm}+p_{ij}-p_{ijm}}{16h^{2}}\right)\Biggr]+\Biggl[\left(\frac{r^{\delta}\alpha}{\rho}\right)_{i-\frac{1}{2},j+\frac{1}{2}}\left(\frac{p_{ijp}-p_{ij}+p_{imjp}-p_{imj}}{16h^{2}}\right)\Biggr]- \\
&\Biggl[\left(\frac{r^{\delta}\gamma}{\rho}\right)_{i-\frac{1}{2},j-\frac{1}{2}}\left(\frac{p_{ij}-p_{ijm}+p_{imj}-p_{imjm}}{16h^{2}}\right)\Biggr]\Biggr\}_{\eta}
\end{aligned}\tag{5.36}$$

where shorthand notation was used such that *ijp=i,j+1, ijm=i,j-1*, and so forth. The corresponding coefficients of [*M*] are given by

$$[M] = Ap_{ij} + Bp_{ipj} + Cp_{imjp} + Dp_{ijp} + Ep_{ipjp} + BFp_{imj} + CFp_{ipjm} + DFp_{ijm} + EFp_{imjm} \tag{5.37}$$

where

$$A = \frac{1}{J_{ij} r_{ij}^{\delta}} \left[\left(\frac{-\alpha r^{\delta} - \gamma r^{\delta}}{16 \rho h^2} \right)_{i+\frac{1}{2}, j+\frac{1}{2}} + \left(\frac{-\alpha r^{\delta} - \gamma r^{\delta}}{16 \rho h^2} \right)_{i+\frac{1}{2}, j+\frac{1}{2}} + \left(\frac{-\alpha r^{\delta} - \gamma r^{\delta}}{16 \rho h^2} \right)_{i+\frac{1}{2}, j+\frac{1}{2}} \right. \\ \left. + \left(\frac{-\alpha r^{\delta} - \gamma r^{\delta}}{16 \rho h^2} \right)_{i+\frac{1}{2}, j+\frac{1}{2}} \right] \tag{5.38}$$

$$B = \frac{1}{J_{ij} r_{ij}^{\delta}} \left[\left(\frac{\alpha r^{\delta} - \gamma r^{\delta}}{16 \rho h^2} \right)_{i+\frac{1}{2}, j+\frac{1}{2}} + \left(\frac{\alpha r^{\delta} - \gamma r^{\delta}}{16 \rho h^2} \right)_{i+\frac{1}{2}, j+\frac{1}{2}} \right] \tag{5.39}$$

$$C = \frac{1}{J_{ij} r_{ij}^{\delta}} \left[\left(\frac{\alpha r^{\delta} + \gamma r^{\delta}}{16 \rho h^2} \right)_{i-\frac{1}{2}, j+\frac{1}{2}} \right] \tag{5.40}$$

$$D = \frac{1}{J_{ij} r_{ij}^{\delta}} \left[\left(\frac{-\alpha r^{\delta} + \gamma r^{\delta}}{16 \rho h^2} \right)_{i+\frac{1}{2}, j+\frac{1}{2}} + \left(\frac{-\alpha r^{\delta} + \gamma r^{\delta}}{16 \rho h^2} \right)_{i-\frac{1}{2}, j+\frac{1}{2}} \right] \tag{5.41}$$

$$E = \frac{1}{J_{ij} r_{ij}^{\delta}} \left[\left(\frac{\alpha r^{\delta} + \gamma r^{\delta}}{16 \rho h^2} \right)_{i+\frac{1}{2}, j+\frac{1}{2}} \right] \tag{5.42}$$

$$BF = \frac{1}{J_{ij} r_{ij}^{\delta}} \left[\left(\frac{\alpha r^{\delta} - \gamma r^{\delta}}{16 \rho h^2} \right)_{i-\frac{1}{2}, j+\frac{1}{2}} + \left(\frac{\alpha r^{\delta} - \gamma r^{\delta}}{16 \rho h^2} \right)_{i-\frac{1}{2}, j-\frac{1}{2}} \right] \tag{5.43}$$

$$CF = \frac{1}{J_{ij} r_{ij}^{\delta}} \left[\left(\frac{\alpha r^{\delta} + \gamma r^{\delta}}{16 \rho h^2} \right)_{i+\frac{1}{2}, j-\frac{1}{2}} \right] \tag{5.44}$$

$$DF = \frac{1}{J_{ij} r_{ij}^{\delta}} \left[\left(\frac{-\alpha r^{\delta} + \gamma r^{\delta}}{16 \rho h^{2}} \right)_{i+\frac{1}{2}, j-\frac{1}{2}} + \left(\frac{-\alpha r^{\delta} + \gamma r^{\delta}}{16 \rho h^{2}} \right)_{i+\frac{1}{2}, j+\frac{1}{2}} \right] \tag{5.45}$$

$$EF = \frac{1}{J_{ij} r_{ij}^{\delta}} \left[\left(\frac{\alpha r^{\delta} + \gamma r^{\delta}}{16 \rho h^{2}} \right)_{i-\frac{1}{2}, j-\frac{1}{2}} \right] \tag{5.46}$$

The ICCG solution algorithm remained unchanged, although the discretization of the coefficients that make-up matrix [*M*] were significantly altered. The 9-point stencil provides a more robust determination of the corresponding coefficients for an orthogonal grid. The same discretization strategy could be employed to produce a 25-point template and so on.

The addition of the 9-point pressure template also required altering the stencil used to calculate the new value of velocity at time $n+1$ from the updated pressure field. Recall the numerical solution of the continuity and momentum equations is based on a two-step projection method given by equation 5.47 and 5.48.

$$\vec{V}^{*} = \vec{V}^{n} + \partial t \left[-\nabla \cdot (\vec{V}\vec{V})^{n} + \frac{1}{\rho^{n}} \nabla \cdot \tau^{n} + \vec{g}^{n} + \frac{1}{\rho^{n}} \vec{F}_{b}^{n} \right] \tag{5.47}$$

$$\vec{V}^{n+1} = \vec{V}^{*} - \frac{\delta t}{\rho^{n}} \nabla p^{n+1} \tag{5.48}$$

The two equations are combined into a single pressure Poisson equation (PPE) for the pressure given as

$$\nabla \cdot \left[\frac{1}{\rho^n} \nabla p^{n+1} \right] = \frac{\nabla \cdot \vec{V}^*}{\delta t} \tag{5.49}$$

Equation 5.49 uses the newly calculated pressure field (p^{n+1}) to update the velocity field. Recall that RIPPLE employs cell face velocities, thus the gradient of the pressure for cell (*ij*) is determined using a difference over cells (*i,j*) and (*i+1,j*) (i.e. cell A and B, see Figure 5.8). The two cell template is inconsistent with the newly developed 9-point pressure stencil. Consistency was achieved using an averaged 6-point template. For example, the pressure gradient in the *x*-direction was determined using a weighted average of 6 cells about cell *ij* (cell A). The updated pressure gradient in the *x*-direction is given as

$$\frac{\partial p}{\partial x} = \left[\frac{0.125\left(p_{ijp} - p_{ipjp}\right) + 0.75\left(p_{ij} - p_{ipj}\right) + 0.125\left(p_{ijm} - p_{ipjm}\right)}{\Delta x} \right] \tag{5.50}$$

The identical technique is used to calculate the pressure gradient in the *y*-direction. The addition of the 9-point pressure stencil and the weighted 6 cell averaging used to update the velocities with the new pressure field increased the robustness and accuracy of the ICCG method. The modified discretization of the PPE resulted in converged solutions with a pressure residual of 10^{-8}.

5.5 Energy Equation Development

Glass is a homogeneous material with a random, non-crystalline (liquid-like) molecular structure. Glass manufacturing processes require that the raw material be heated to a temperature sufficient to produce a completely fused melt, which when cooled rapidly, becomes rigid without crystallizing (Owens Corning, 2000).

Glass does not solidify but rather experiences a dramatic change in viscosity with temperature, as shown in Figure 5.10. The ability to predict the axial temperature profile within the glass fiber is critical. Once the temperature is known a corresponding viscosity may be determined within the fiber. As a result, localized areas of high viscosity are the most likely to experience brittle failure and fracture.

Within the three classical states of matter, there is no place for glass. Glass is amorphous, although it combines the rigidity of crystals with the random molecular structure of liquids.

The atoms in glass, although arranged at random, are frozen in position. Thus, glass combines some of the aspects of a crystalline solid and a liquid; it is rigid like a solid but its random atomic structure is characteristic of a liquid. The American Society for Testing and Materials defines glass as "... an inorganic product of fusion which has cooled to a rigid condition without crystallizing" (Owens Corning, 2000).

The viscosity of water at room temperature is 0.001 N-sec/m^2 (0.010 poise); that of SAE30 motor oil is about 0.1 N-sec/m^2 (1.0 poise). The viscosity of most glass at room temperature is theoretically about 10^{18} - 10^{21} N-sec/m^2 (10^{19} - 10^{22} poise). As the temperature of glass increases, the inflexible molecular network breaks down into smaller units. Viscosity drops to about 10^6 N-sec/m^2 (10^7 poise) and may start to deform under its own weight. At higher temperatures, viscosity drops to 10^2-10^3 N-sec/m^2 (10^3-10^4 poise) when the glass will flow into a mold, or can be blown with ease (Owens Corning, 2000). When heated to very high temperatures, the viscosities of glasses may be so low that they become as liquid as thin motor oil. The critical value of viscosity that corresponds to a melt temperature of 1260 K for the generic glass used in all of the simulations is approximately 11 N-sec/m^2 (110 poise), as shown in Figure 5.11. If the localized glass temperature falls below this critical value, the glass is assumed to be a solid and most likely to fracture at that particular point within the fiber.

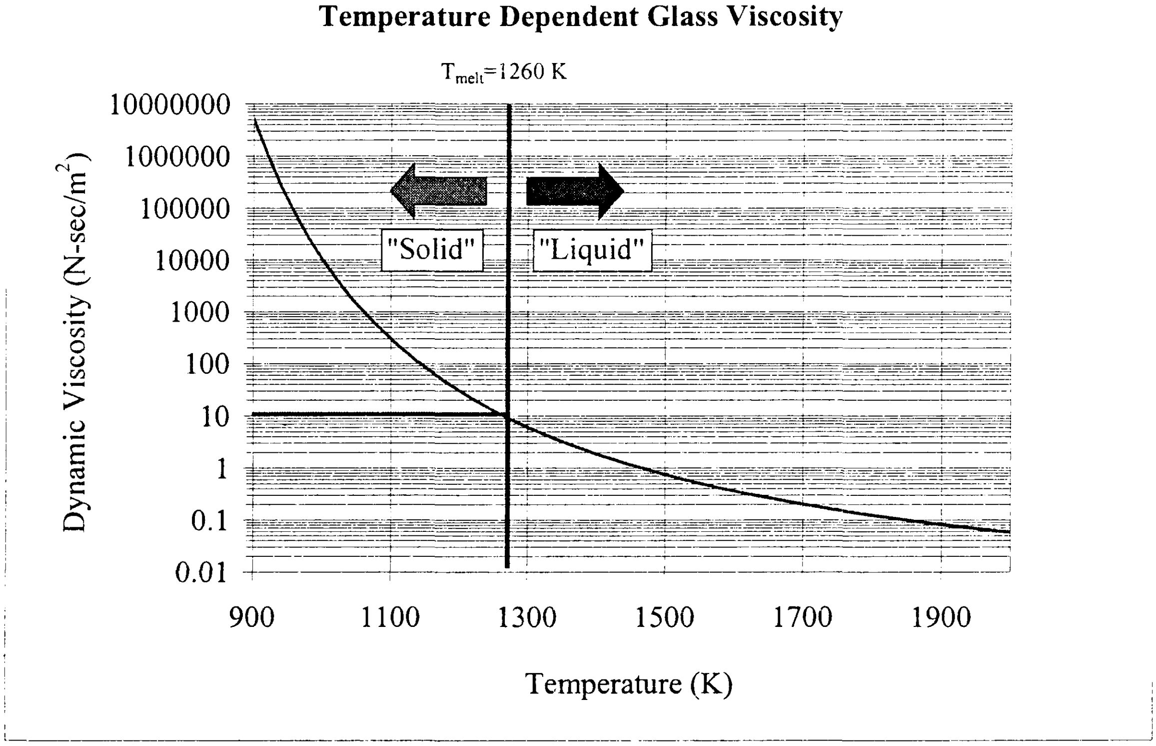

Figure 5.10. Temperature dependent kinematic viscosity. T_{melt}=1260 K is the critical melt temperature of glass.

The implementation of Johnson's one fluid, heat transfer model into the current two-fluid model required several modifications and simplifying assumptions. A fully temperature dependent, variable density and viscosity, two-fluid, model was initially proposed to accurately simulate the process of discontinuous fiber spinning. This would require solving both the governing flow and energy equations in each of the fluids, as well as applying specific boundary conditions at the fluid interface. However, an initial order of magnitude analyses, which examined the axial and radial analytical temperature distributions within a hypothetical glass fiber, has provided the basis to pursue the development of a much more simplified fluid/thermal solver.

A hypothetical thermal environment of the rotary spinning process is shown in Figure 5.11. The arrow indicates the general free stream path of the molten glass filaments as they exit the disk sidewall. It is hypothesized that initially the filaments follow a path that is approximately tangent to the temperature contours. The glass filament is either heated or cooled by the surroundings depending on the exit temperature of the glass filament and the surround environmental. As the fiber attenuates it eventually reaches a point in the critical zone when the filament begins to cool.

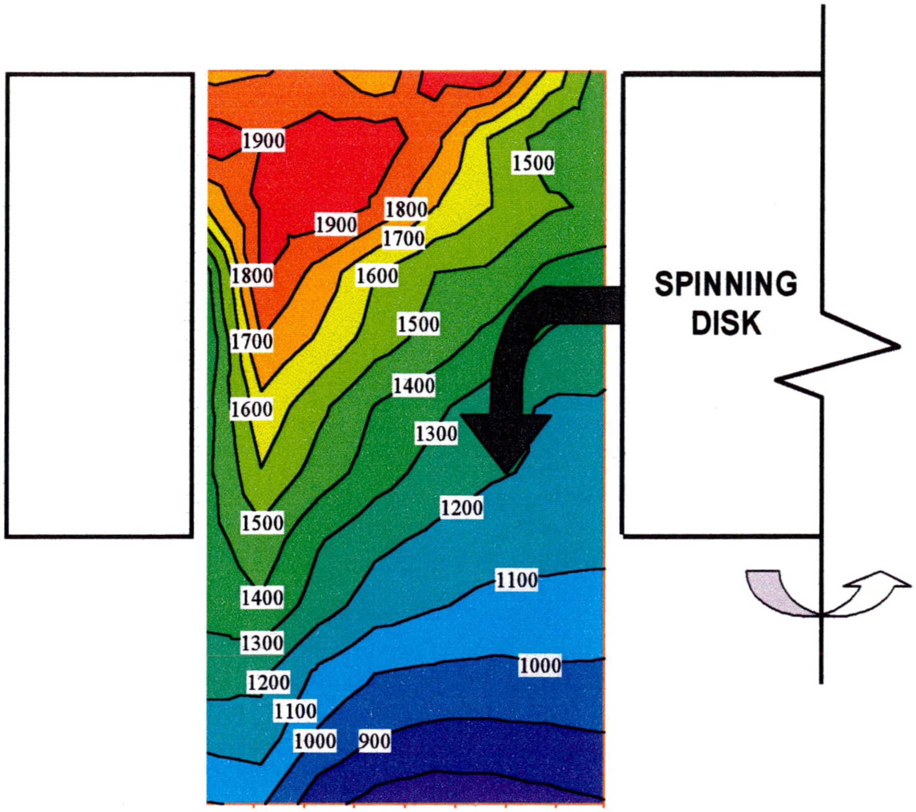

Figure 5.11 Hypothetical temperature contour. (units: deg. K) Arrow represents direction of extruded fibers.

The distance between each successive temperature contour is believed to be larger than the size of glass filament that can be simulated in a reasonable amount of CPU run time. In theory a very large computational domain could be constructed to model a much larger length of fiber given sufficient computing resources. Due to mesh density restrictions, the simulated fiber size is less than the distance between each temperature contour. Thus, the surrounding temperature of the fiber is assumed to be constant, but remains dependent on the position of the fiber within the flow field.

Theoretical predictions of the radial and axial temperature profiles within the fiber have been estimated using correlations for the temperature distributions within an infinite cylindrical fin (Incropera, 1990). The inlet and surrounding temperature of the glass and air were 1300 K and 1500 K, respectively. The Heisler-Grober charts were used to predict the analytical solution for the radial heat transfer in a 400 micron diameter fin. The results indicate a uniform temperature profile. The axial temperature variation, shown in Figure 5.12 was estimated using a cylindrical fin in cross flow. The temperature of the 5 mm long glass filament eventually approaches the surrounding gas temperature.

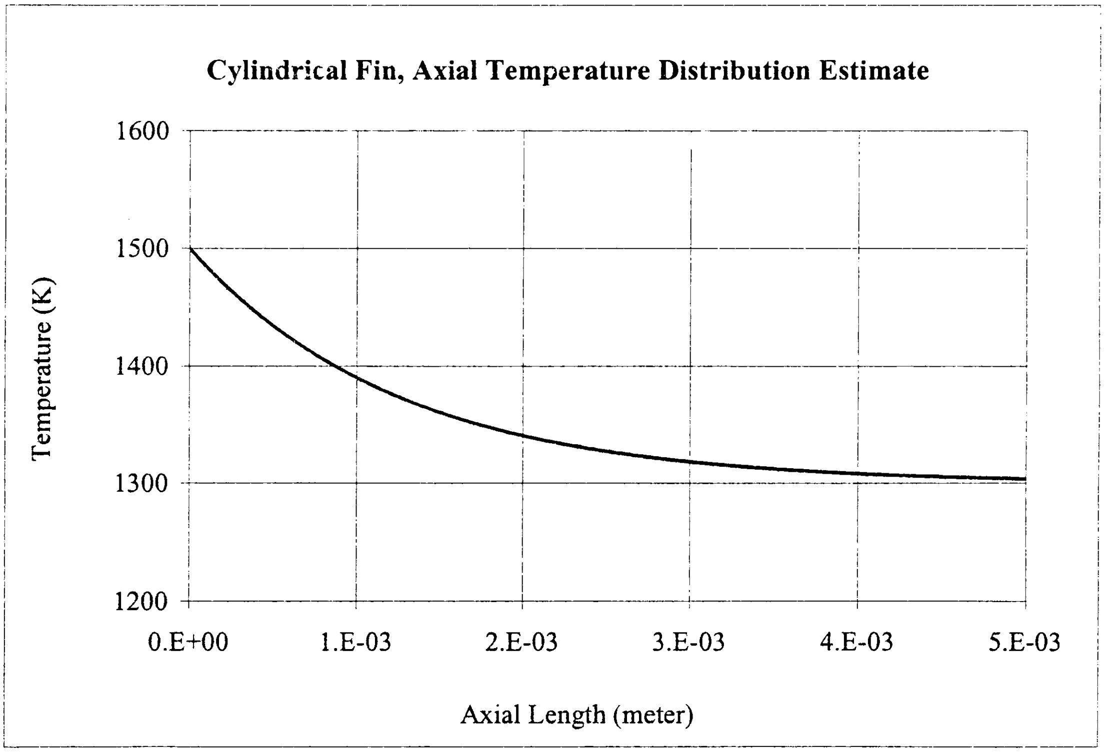

Figure 5.12 Infinite cylinder axial temperature profile approximation.

The results of the scaling arguments, CPU limitations and preliminary analytical temperature predictions indicate that the extrusion of a molten glass filament may only be simulated using a localized model. A global model of larger scale may only be achieved by "piecing" together a number of smaller simulations.

Furthermore, a fully temperature dependent, two fluid/thermal solver is not needed to accurately model the process of discontinuous fiber spinning. The same level of complexity may be achieved using the one fluid, constant property, heat transfer model of Johnson (2001) integrated with the two fluid, flow solver RIPPLE.

In the process of discontinuous glass manufacturing molten glass filaments are cooled by the passing turbulent airflow, which results in a sharp increase in the glass viscosity. This localized increase in glass viscosity causes the fiber to become brittle, ultimately leading to fracture (i.e. fiber formation). In order to characterize this behavior, a thermal model was needed to identify localized areas of the fiber that undergo rapid changes in viscosity. Characterizing these localized areas aids industrial practitioners in identifying potential failure mechanisms. The background required to assemble such a model has initially been completed by Johnson (2001). The researcher has developed a numerical model specifically for simulating the process of droplet solidification. The researcher's model provides the basis to develop a thermal model of discontinuous fiber manufacturing.

Johnson has developed, verified and validated a numerical model for the simulation of heat transfer in free surface flows. The thermal solver simulates the impact and solidification of a droplet onto a substrate as it occurs in the process of spray deposition. Johnson's one fluid, heat transfer model has been successfully integrated into RIPPLE, which allows detailed numerical simulations of droplet impact, spreading and solidification. The heat transfer model is applied over the complete domain (droplet and substrate) using the enthalpy method.

The heat transfer model initiated by Delplanque *et. al.* (1999,1996) focuses on the effect of solidification on fluid flow. In order to predict quantitatively the heat transfer and solidification behavior of liquid metal impact, it is necessary to solve the energy equation. The enthalpy formulation, rather than a temperature formulation, which uses contact resistance between the droplet and substrate, is more desirable because the phase change process can be determined without explicitly tracking the solid liquid interface. The enthalpy method, which is based on the conservation of energy principal expressed in terms of thermal energy (i.e. enthalpy) and temperature, together with equation of state contain all of the information needed to determine the phase evolution. The energy equation, formulated in terms of enthalpy, was discretized and implemented into the one fluid, flow solver RIPPLE. Johnson's droplet model solves the energy equation over the entire droplet, while considering the surrounding volume to be void. Recall that RIPPLE advects the VOF function (*F*) with the velocity field to track the location of the free surface. Johnson's method advects the enthalpy along with the VOF data, which is used to identify phase change by the localized value of enthalpy.

The fundamental principle of conductive and convective heat transfer is the thermal energy conservation law given as

$$\frac{\partial h}{\partial t} + \nabla \cdot (Fh\vec{V}) = -\nabla \cdot q + \frac{\partial p}{\partial t} + \nabla \cdot (Fp\vec{V}) \qquad (5.51)$$

assuming the heat generated by viscous dissipation is negligible.

Johnson (2001) focused on solidification of the droplet near an obstacle. In the case of glass fiber formation there are several differences. First, the process of glass spinning requires simulating the interaction between two fluids, unlike the process of spray deposition, which is modeled using only one fluid. Secondly, Johnson 's droplet impact requires a solidification model, where as glass does not solidify.

The enthalpy along with the VOF data is advected using the updated velocity field. However, the enthalpy is only advected within the glass region. The enthalpy of the air is neglected. Additional, modifications to the heat transfer model included the addition of convection and radiation at the fluid interface. Using the modified heat transfer model of Johnson, the associated temperature and heat flux data is determined within the glass region. The heat flux is determined iteratively and related to the temperature using either conduction or convection and radiation depending on the location within the fiber. Within the fiber the conduction term is given by Fourier's Law

$$\vec{q}_{cond} = -k\nabla T \tag{5.52}$$

and the convection and radiation terms are given as

$$\vec{q}_{conv} = \bar{h}(T_s - T_{surr}) \tag{5.53}$$

$$\vec{q}_{rad} = \varepsilon\sigma(T_s^4 - T_{surr}^4) \tag{5.54}$$

where T_s is the fiber surface temperature, T_{surr} is the surrounding temperature, k is the glass conductivity, h is the heat transfer coefficient, ε is the glass emissivity and σ is the Stefan-Boltzmann constant.

Johnson's (2001) initial heat transfer model applied an adiabatic (i.e. heat flux equal to zero) boundary condition at the free surface of the droplet. The glass fiber simulation requires the addition of convection and radiation heat transfer, thus applying the appropriate heat flux balance to the free surface. The convective heat transfer coefficient was estimated using an average coefficient determined over the entire length of the fiber. An approximation for laminar flow over a flat plate was used to calculate the Nusselt number (Incropera and DeWitt, 1990), given by

$$Nu_x = \frac{0.338\, Re_x^{1/2}\, Pr^{1/3}}{\left[1 + \left(0.0468/Pr\right)^{2/3}\right]^{1/4}} \tag{5.55}$$

From the localized Nusselt number, a connective coefficient was determined and the assumption of a constant air temperature enabled the explicit determination of the convective heat flux at the interface. The explicit radiation heat transfer was approximated as a real surface with an emissivity of 0.8 and the surrounding temperature was estimated form process measurements.

The two fluid flow solver and the one fluid thermal solver are two independent models which share the commonality of advecting scalars (i.e. the VOF and enthalpy data) using the velocity field as well as updating the glass viscosity with the current glass temperature field. The remaining material properties within the glass and air regions remain constant for the duration of the simulation.

Several modifications to each model were required upon successful integration of the two solvers. The strong dependence of glass viscosity with temperature favors the use of integrating the thermal/fluid solvers, however as discussed in section 6.6, several difficulties originated that did not permit a fully integrated model. The most prominent of these was Vi^3S-FLOW's inability to function within the "creeping" flow regime, which was primarily due to the rapid increase in viscosity with decreasing temperature as the molten glass approaches the melt temperature. As a result, the thermal and fluid models were not integrated but remain capable of providing useful information regarding fiber formation by tracking the development of the fluid interface (from the fluid model) and the temperature field (from the thermal model). Superposition of the VOF and temperature fields can aid in identifying critical regions (i.e. regions of elevated viscosity and attenuation) were fiber formation is most likely to occur.

The temperature dependent glass viscosity is the critical factor in the fiber simulations. If the temperature of the glass melt remains above the critical melt temperature of 1260 K, an accurate solution to the thermal/fluid flow field is likely to be achieved in a timely manner. However, if the temperature of the glass drops below the critical temperature, a corresponding sharp rise in viscosity is initiated which results in a transition of the glass flow from the laminar to creeping flow regimes, which resulted in significant inaccuracies do to V*i*^{3}S-FLOW's inability to simulate creeping flows.

Preliminary simulations of hypothetical glass fibers in the creeping flow regime have produced erroneous results. There were significant instabilities that developed at the air/glass interface which resulted in break-up of the VOF field. As a result the fluid thermal solvers will remain separate while a solution to this difficulty is reached.

CHAPTER SIX

NUMERICAL RESULTS

Over the course of the numerical development several modifications have been made to the original RIPPLE source code. The modifications substantially altered the code from its original one fluid state to one that enables the user to simulate the shear air/fiber interaction, similar to that occurring in industry. Following the completion of the numerical modifications (presented in Chapter 5), test cases that possessed well-founded analytical solutions were used to verify, validate and test (VV&T) the CFD code to ensure that the original flow solver had not been corrupted during the modification process and that the addition of each module provided measurable improvement to the CFD code's ability to simulate the air/fiber interaction. Since there exists very little experimental data and no known numerical data for the process of discontinuous glass fiber spinning, the test cases were paramount to VV&T the CFD model to ensure accurate and acceptable results from the glass fiber simulations.

6.1 PLIC Test Cases

The PLIC algorithm, developed by Kothe and Rider (1998), has been implemented to track the rotation of a known VOF data on a mesh when subject to a known velocity field. The intent is to demonstrate the algorithm's ability to accurately track the fluid free surface. A single forced vortex meant to induce solid body rotation has been placed at the center of the fluid domain (Fox and McDonald, 1992). The rotation experienced by the fluid due to the forced vortex provides a useful tool in debugging and evaluating the PLIC interface tracking routine. An acceptable interface tracking method must translate and rotate a fluid volume without significant degradation of the fluid interface (Kothe, 1999).

6.1.1 Solid Body Rotation

In this example, a 10 x 10 VOF data was created on a 20 x 20 computational mesh. Figure 6.1 shows the results from the initial time step through one complete revolution of the VOF data. One revolution occurs following a CPU run-time of 64 seconds. The solid body rotation was applied using the following velocity components given by

$$\begin{aligned} u(i,j) &= -\omega(y(j) - y_{center}) \\ v(i,j) &= \omega(x(i) - x_{center}) \end{aligned} \tag{6.1}$$

where ω=constant

Figure 6.1 shows the results of the solid body rotation test case.

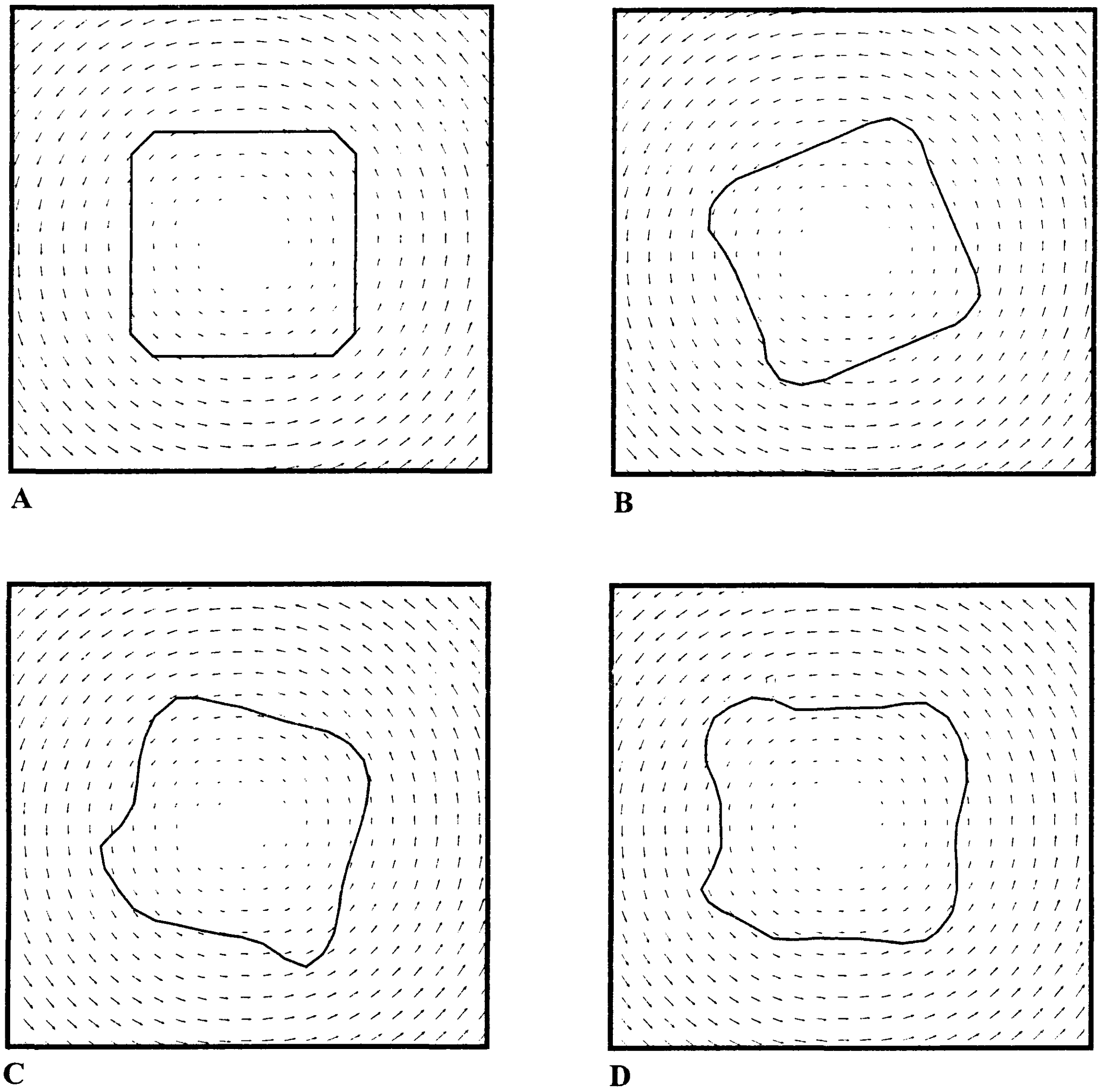

Figure 6.1. PLIC Test Case. (A) t = 1 sec, (B) t = 5 sec, (C) t = 30 sec, (D) one complete revolution at a computational run-time of t = 64 sec.

6.1.2 Capillary Jet Break-up

Given the results of solid body rotation test case, it is evident that the PLIC interface-tracking algorithm possess the potential to accurately track the fluid free surface. However, further analyses must be completed to determine if the PLIC algorithm provides more favorable results than the SLIC algorithm, which is currently used in RIPPLE. A quantitative comparison of the two methods has been completed using the capillary jet breakup example provided by Kothe *et. al.* (1991). The capillary jet breakup test case was chosen due to its similarity to the process of molten glass extrusion and its well-founded analytical solution developed by Rayleigh (1879) and Mansour and Lundgren (1990). Three capillary jet test cases have been simulated using RIPPLE, interfaced with two different interface-tracking algorithms. The first case uses the SLIC algorithm applied on a coarse mesh. The second case uses the SLIC algorithm applied on a more refined mesh. Lastly, the PLIC algorithm is applied on a coarse mesh identical to the first case.

Rayleigh (1879) developed the first quantitative theory for the growth and radial perturbation on a small cylindrical column of liquid (i.e. capillary jet). Surface tension forces in the *r-z* plane at points *z* along the jet surface, pinching it inward and eventually leading to the development of bulges and contractions causing the jet to break up, forming small droplets or satellites.

An example of a capillary instability of a liquid jet is shown in Figure 6.2. The figure shows water forced out of a 4 mm tube from the right hand side of the Figure. The tube was perturbed at various frequencies by a loudspeaker to produce break-up. The instability results in break-up of the capillary jet producing satellites of various size.

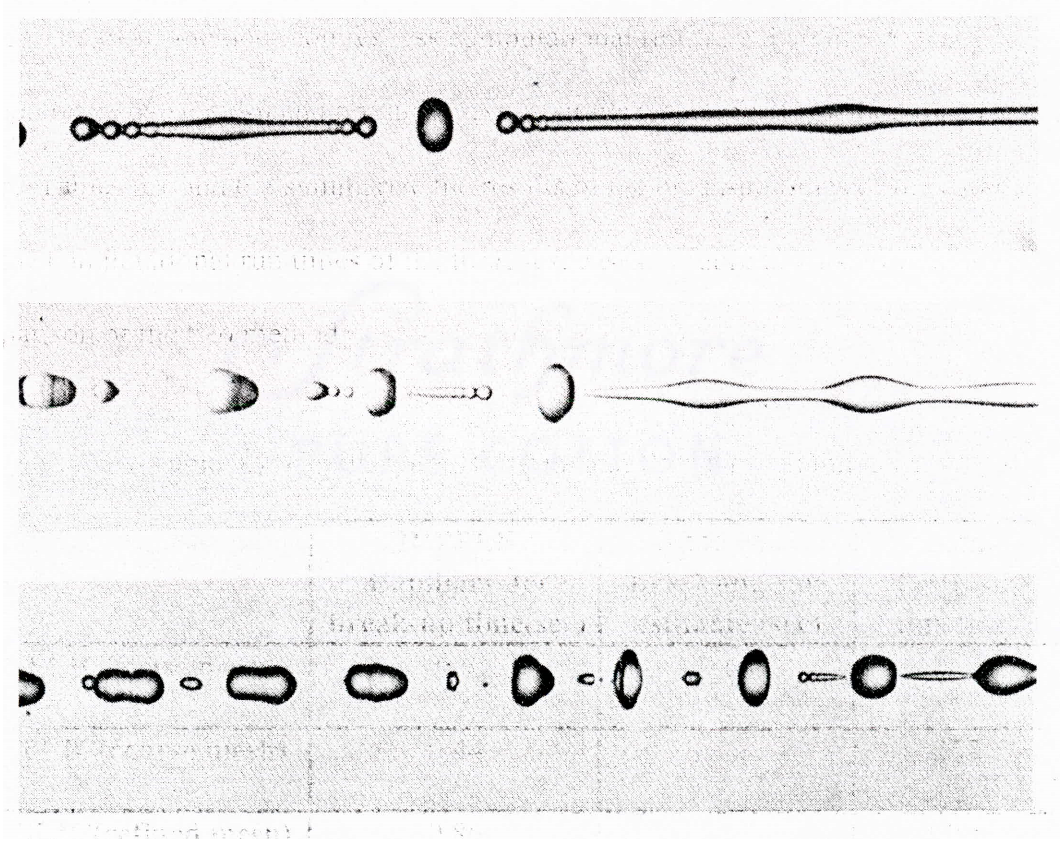

Figure 6.2 Capillary jet break-up. Image taken from An Album of Fluid Motion (Van Dyke, 1998). Experiment completed by Rutland and Jameson, 1971.

The capillary jet break-up was computed with RIPPLE using water (ρ=1 g/cm^3, σ=73.05 dynes/cm) as the liquid stream with a zero pressure background (Kothe *et. al.*, 1991). Symmetry conditions about the axis were implemented to take advantage of the flow geometry and avoid excessive computing time.

Each of the three simulations are identical except for the interface tracking algorithm and the mesh density. The first and third simulations use a 30 x 40 coarse mesh, while the second simulation uses a 30 x 140 refined mesh. The refined mesh gives a much higher lateral resolution and an improved radial resolution with cell spacing closer near the cylindrical axis. The increased resolution of the second simulation captures the higher harmonics of the nonlinear flow. Although, the refined mesh provides a more accurate solution, the computational time dramatically increases by a factor of six. Thus, there exists a trade-off between numerical accuracy and computational run time.

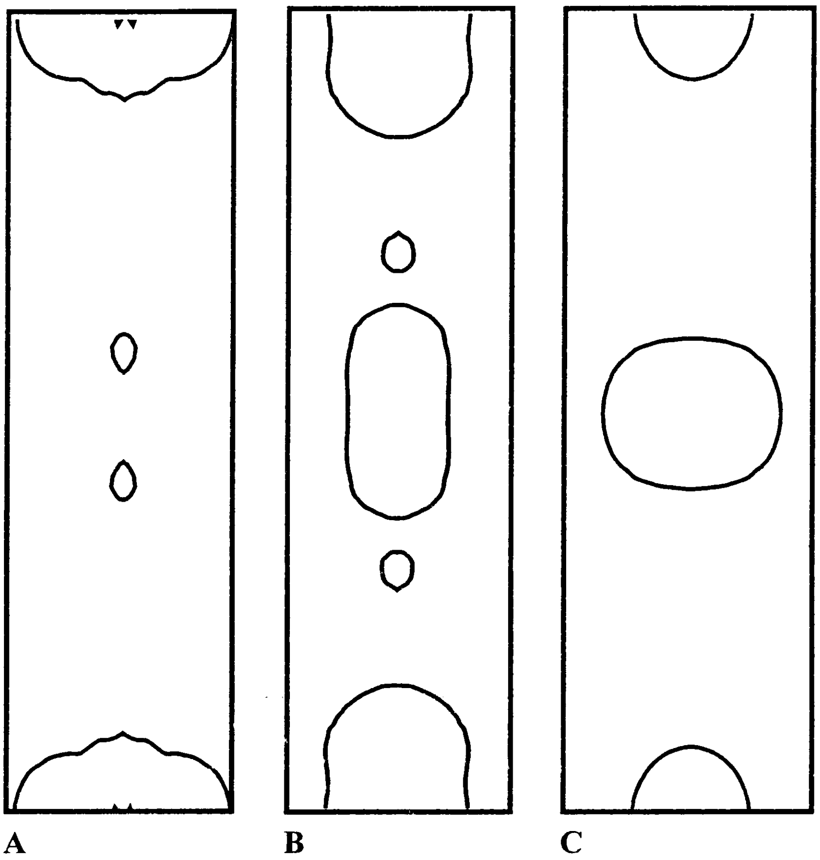

Figure 6.3. PLIC vs. SLIC comparison. (A) SLIC coarse mesh, (B) SLIC refined mesh, (C) PLIC coarse mesh

Each of the three results were recorded at a finish time of 0.9 seconds. Figure 6.3(A) shows the formation of two small satellite droplets. This is consistent with the results of Kothe *et. al.* (1991). Figure 6.3(B), shows the formation of one large droplet with two small satellite droplets. The refined mesh provides a much higher lateral and radial resolution than the alternative coarse mesh, in addition to resolving the higher harmonics of the nonlinear flow. The additional resolution produces more accurate results at the expense of substantial increases in computing time.

An alternative to the SLIC method on a refined mesh is to implement the PLIC method on the original coarse mesh. In Figure 6.3(C), the pinching of the capillary jet produces one large satellite, which is similar to that of the SLIC method on a refined mesh. The PLIC method requires less computational run-time than that of the SLIC method on a coarse mesh and produces results similar to the SLIC method on a refined mesh. Tables 6.1 and 6.2 summarize the results of the break-up times of the capillary jet and the computational run times of the three test cases. Figure 6.3 also provides a comparison of the two methods.

Table 6.1. Capillary Jet Break up and Run Time Summary

	RIPPLE Capillary Jet break-up time(sec)	**Kothe *et. al.* break-up time estimate (sec)**	**Total CPU run time(sec)**
SLIC(coase mesh)	0.6	0.69	233
PLIC(coarse mesh)	0.44	n/a	257
SLIC(refined mesh)	0.86	1	1495

Another qualitative measure of the PLIC algorithm's ability to provide more accurate results than the SLIC algorithm is to compare the satellite droplet size computed using RIPPLE with the analytical predictions derived by Mansour and Lundgren (1990). Table 6.2 summarizes the droplet size results obtained from RIPPLE simulations and Mansour and Lundgren analytical solution (1990). The percent error in each case is somewhat large and may be attributed to inconsistencies between the analytical and numerical solutions. The analytical solution provided by Mansour and Lundgren (1990) is a linear solution that is applicable in the early stages of the perturbation development. The phenomenon of capillary break-up, disregarding the early development stages, is a highly non-linear event. The analytical predictions due not capture this aspect, however the CFD code, which is a nonlinear code, does capture the entire process. As a result, the discrepancy is likely due to the non-linearity of the capillary jet break-up and the inability to capture it with a linear, analytical prediction.

Table 6.2. Satellite Size Comparison Summary

Interface Reconstruction Algorithm	**RIPPLE estimated satelite volume (m^3)**	**Rayleigh's analytical volume (m^3)**	**Error Estimate (Rayleigh)**
SLIC(coarse mesh)	2.02E-08	6.17E-06	100%
PLIC(coarse mesh)	3.19E-06	6.17E-06	48%
SLIC(refined mesh)	3.79E-06	6.17E-06	39%

A comparison summary of the PLIC and SLIC methods are shown in Figure 6.4. The SLIC method applied on a refined mesh is likely the closest to the actual phenomenon than either the PLIC or the SLIC applied on a coarse mesh. As mentioned previously, the refined mesh enables resolution of higher harmonics. However, additional computational run-time time is required for the SLIC calculation on a refined mesh. A trade-off exists between resolving higher harmonics within the simulation at the expense of increased computational run time required for greater mesh density. The goal was to minimize computing time while improving the interface tracking algorithm. Thus, the PLIC method was implemented using a coarse mesh.

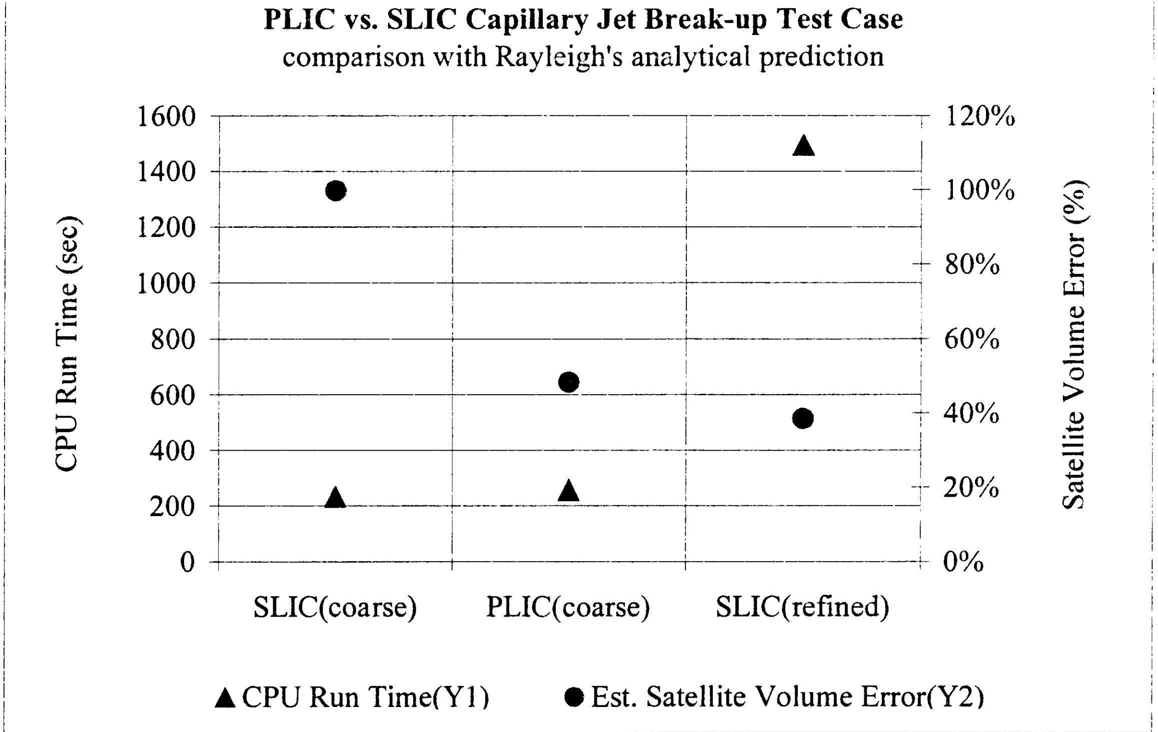

Figure 6.4. PLIC vs. SLIC comparison summary

6.2 Rayleigh-Taylor Test Case

A Rayleigh-Taylor (RT) instability test case was used to validate the addition of the variable density, two-fluid model to the original RIPPLE source code. As a fluid of density, ρ_1 is supported against gravity by a lighter, fluid of density, ρ_2, a Rayleigh-Taylor instability develops perturbations that grow exponentially in time. The following test case predicts the evolution of the two-dimensional Rayleigh-Taylor instability for several different surface tension coefficients.

The RT test case is one of the classical instabilities used in fundamental fluid mechanics. The buoyancy driven flow is also one of the most difficult to accurately simulate. It is the prototype problem for fluid mixing induced by unstable stratification, and is of similar importance as the KH instability, which is fluid mixing induced by shear flow. This fundamental test case has been the focus of numerous past studies starting with Rayleigh (1935) and most recently those studies completed by Tryggvason and Unverdi (1992).

An example of a RT instability is shown in Figure 6.5, which depicts buoyant thermals rising from a heated surface. The results show mushroom shaped plumes rising periodically from a heated copper plate. The plumes are made visible by an electromechanical technique using thymol blue.

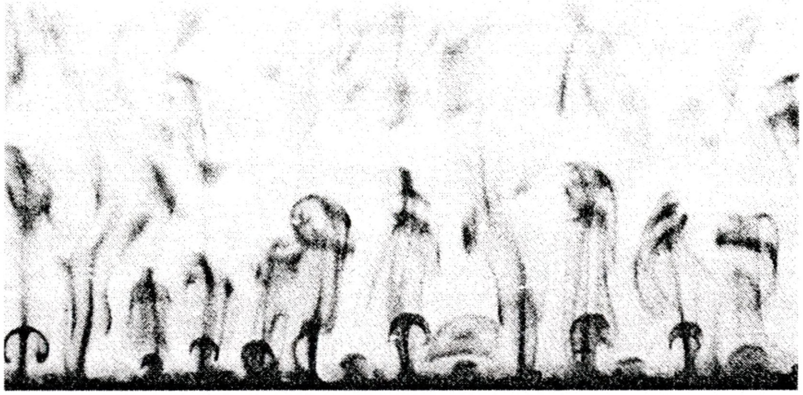

Figure 6.5. Rayleigh Taylor instability. Buoyant thermals rising from a heated plate. Image taken from An Album of Fluid Motion (Van Dyke, 1998). Experiment completed by Sparrow, Husar and Goldstein, 1970.

The RT instability possesses both linear and nonlinear phases of growth. The calculated linear growth rate is compared with Chandrasekhar's (1961) analytical predictions.

The RT instability develops perturbations of the interface that grow exponentially in time as exp*(nt)* for small attitudes. Given a known surface tension coefficient, the growth rate n is given by

$$n^2 = kg\left[A_t - \frac{k^2\sigma}{g(\rho_1 + \rho_2)}\right] \tag{6.2}$$

where k is the wavenumber of the perturbation, g is the gravitational acceleration perpendicular to the interface, and A_t is the Atwood number defined as

$$A_t = \frac{\rho_1 - \rho_2}{\rho_1 + \rho_2} \tag{6.3}$$

A critical surface tension coefficient (σ_c) can be calculated from equation 7.2 by setting the growth rate (n) to zero. Referring to the work of Daily (1969), a stability parameter (I) can be defined as

$$I = {}^{\sigma}\!/_{\sigma_c} \tag{6.4}$$

For values of $I>1$, n becomes imaginary causing the interface to oscillate. Following the work of Brackbill *et. al.* (1992), the time and velocity are expressed in units of τ and $g\tau$, respectively, where τ is the RT growth time n^{-1} for $\sigma=0$. The Atwood number is 0.6. The instability is initiated with a perturbation of the form 0.035cos(kx) given to the vertical velocity component at the interface. The wavenumber (k) is set to 5/3. Surface tension varies between 0 and 12 N/m. The numerical computations were performed on a 30 x 90 mesh.

The RT instability test case examines the accuracy of the two fluid CSF model (Brackbill *et. al.* 1992). A comparison of the numerical and theoretical results show that becomes unstable for $I>1$. If the interface is to remain stable, the surface tension force must directly balance the gravitational acceleration.

The results of the RT test case simulations are shown in Figure 6.6. The development of the interface is shown at a time of 6.25 for a stability parameter (I) equal to 0, 0.19, 0.38, 0.57, 0.75, 0.94, 1.0 and 1.13. Examining Figure 6.6 indicates a decrease in interface deformation with increasing surface tension between the two fluids. For a stability parameter of $I=1$, the surface tension directly balances the gravitational acceleration and there is no movement of the interface. For $I>1$, the growth rate becomes unstable, due to the imaginary root, and the initial surface perturbation begins to oscillate. These results are in agreement with those completed by Brackbill *et. al.* (1992) and Daily (1969).

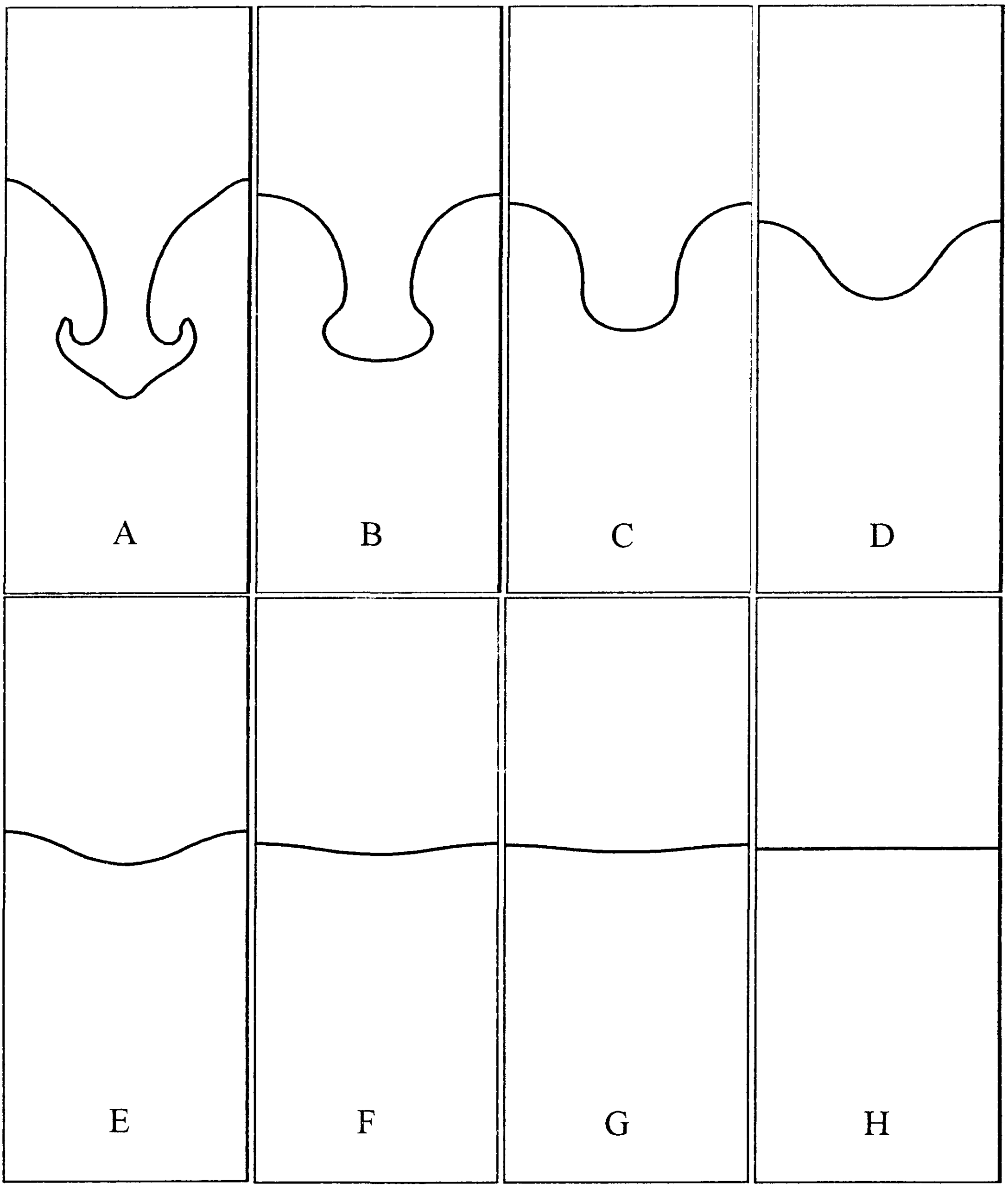

Figure 6.6. Rayleigh-Taylor Instability Test Case.
Interface between fluids, defined as the VOF contour, shown at a time of 6.25 for a stability parameter (I) equal to (A) 0, (B) 0.19, (C) 0.38, (D) 0.57, (E) 0.75, (F) 0.94, (G) 1.0 and (H) 1.13.

The theoretical growth rate as determined by Chandrasekhar, (1961) has also been compared to the numerical growth rate and is plotted as a function of the stability parameter, *I*, as shown in Figure 6.7.

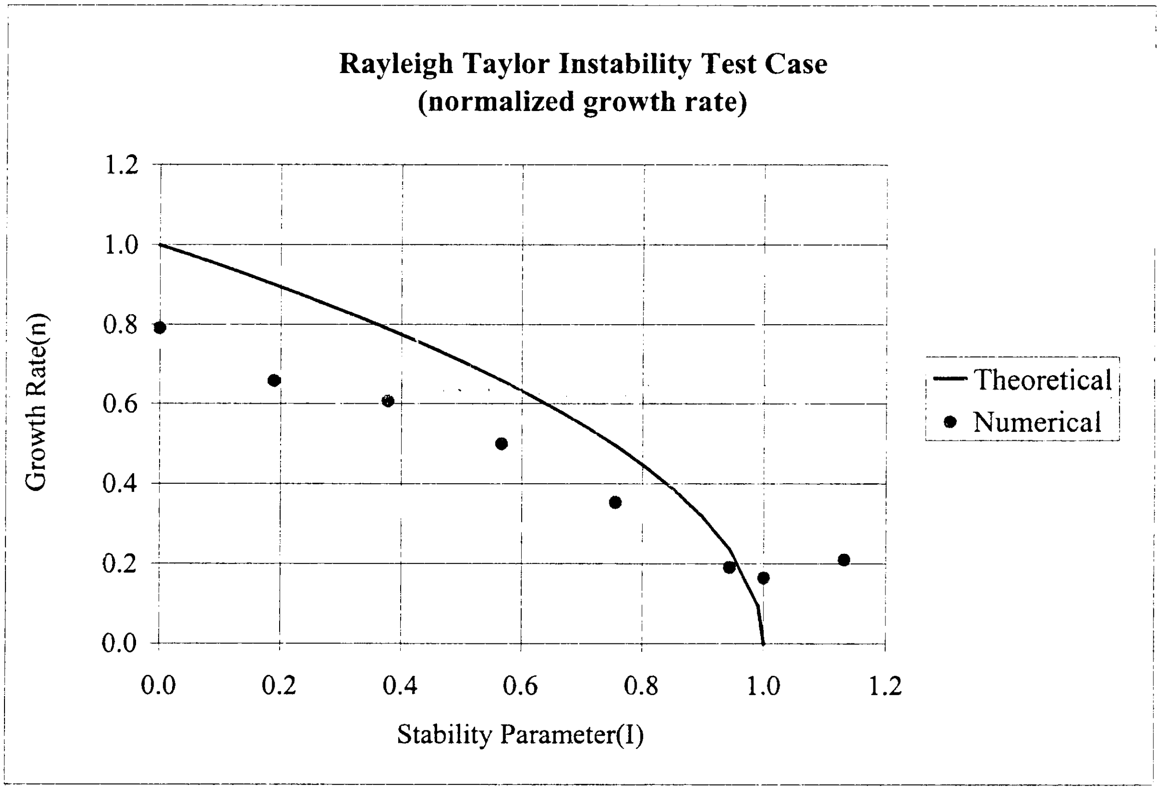

Figure 6.7 Theoretical vs. numerical instability growth rate comparison.

The numerically computed linear growth rate, is nonzero for $I > 1$. This result is consistent with that of Brackbill *et. al.* 1992, who insists that mass diffusion is the cause for the unstable flow prior to $I > 1$. Other results not shown indicate how this may occur. There is a persistent circulating flow, even before $I > 1$, which may cause numerical diffusion in the calculation of conductive transport term (Brackbill *et. al.* 1992). Diffusion of the heavier fluid downward and buoyancy of the lighter fluid upward provide a source of free energy that drives flow, just as bulk motion of the heavier fluid drives to flow in the RT instability in the absence of diffusion (Brackbill *et. al.* 1992).

6.3 Pipe Flow Test Case

A comprehensive characterization of the shear stress interaction occurring at the fluid interface has been attained with the addition of the complete viscous stress tensor and variable viscosity model discussed in Section 5.3. The addition of the modified 9-point pressure template used in the ICCG routine (see Appendix A, section A.7) has also been integrated and provides a more robust method for determining the pressure field over the two fluid domain. Initially a two fluid, laminar pipe flow test case was used to evaluate the viscous stress tensor and PPE modifications. The pipe flow test case was chosen due to its well-founded analytical solution which fully describes the velocity profile of two dissimilar fluids along a pipe cross section (Schlichting, 1951). However, difficulties due to the no-slip, wall condition at the right domain boundary led to erroneous results, which are unexplainable at this time (see Appendix C).

The ultimate goal of the research is to simulate the extrusion of a glass filament similar to that which occurs in the process of discontinuous fiber manufacturing. The fiber simulations, which are similar to the two fluid pipe flow, did not include a no-slip boundary along the right edge of the computational domain. Instead, the fiber simulations employ a free-slip condition on both the left and right boundaries. Thus, an additional test case was completed that compared the analytical and numerical profiles for free-slip boundaries with two fluids with identical fluid properties. The result is shown in Figure 6.8.

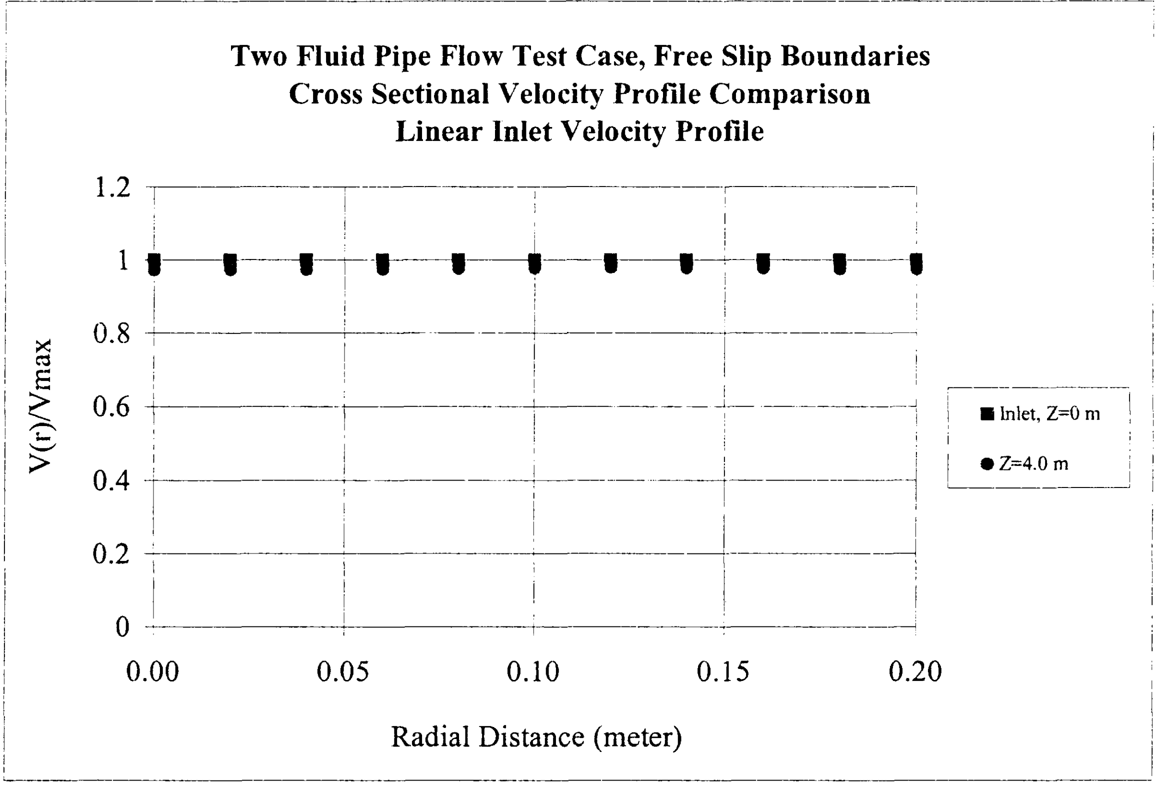

Figure 6.8 Two fluid, free-slip boundary test case.

The numerical and analytical results compare very well, producing a total error of less than 3%.

Although there is measurable error associated with the two fluid pipe flow test case that employs a no-slip condition, acceptable results are attained from the two fluid pipe flow test case which employs a free-slip condition along the right boundary. Additional free-slip simulations were completed that demonstrate the code's ability differentiate between two fluids with vastly different fluid properties. Density and viscosity ratios on the order of 20,000:1 and 25:1 were successfully modeled, which indicate that the newly modified code is capable of accurately simulating the glass extrusion process as it occurs in industry.

During the process of identifying potential sources of error in the two fluid pipe flow test case, another challenge was identified that required immediate attention. The modified CFD code attained converged solutions only with a residual that was much too large (on the order of 10^{-2}). As the residual was decreased to an acceptable value (on the order of 10^{-8}) pressure convergence failures occurred throughout the domain, ultimately terminating the simulation. The identification of the convergence problems led to the development of the new 9-point pressure stencil used in determining the pressure coefficients that are an integral part of the ICCG solution algorithm (see Section 5.4). Upon successful integration of the 9-point pressure stencil, the code achieved convergence with a pressure residual on the order of 10^{-8}. The robustness of the code was also improved, enabling simulations of density and viscosity ratios near 20,000:1 and 25:1, respectively. However, the velocity deficit remained in the two fluid pipe flow test case.

6.4 Static Droplet Test Case

In all interface tracking numerical schemes the development of parasitic surface currents occur, which result from numerical errors in the surface force calculation. These numerically induced errors can become a problem and may lead to physical impossibilities in the flow field. Following all modifications to the two-fluid, CSF model, a static droplet test case was implemented to examine the development of spurious surface currents between the original two-fluid source code and the modified source code. A 30x30 computational mesh was used with a density ratio of 2:1 and a viscosity ratio of 10:1. The coefficient of surface tension was approximately 0.07 N/m.

The ideal solution should result in a velocity field that is identically zero, but the development of spurious surface currents develop in both cases. The growth of total kinetic energy (TKE) over the entire domain is used to measure the growth of spurious surface currents. The total TKE was normalized using the surface tension coefficient and the droplet diameter (σd^2).

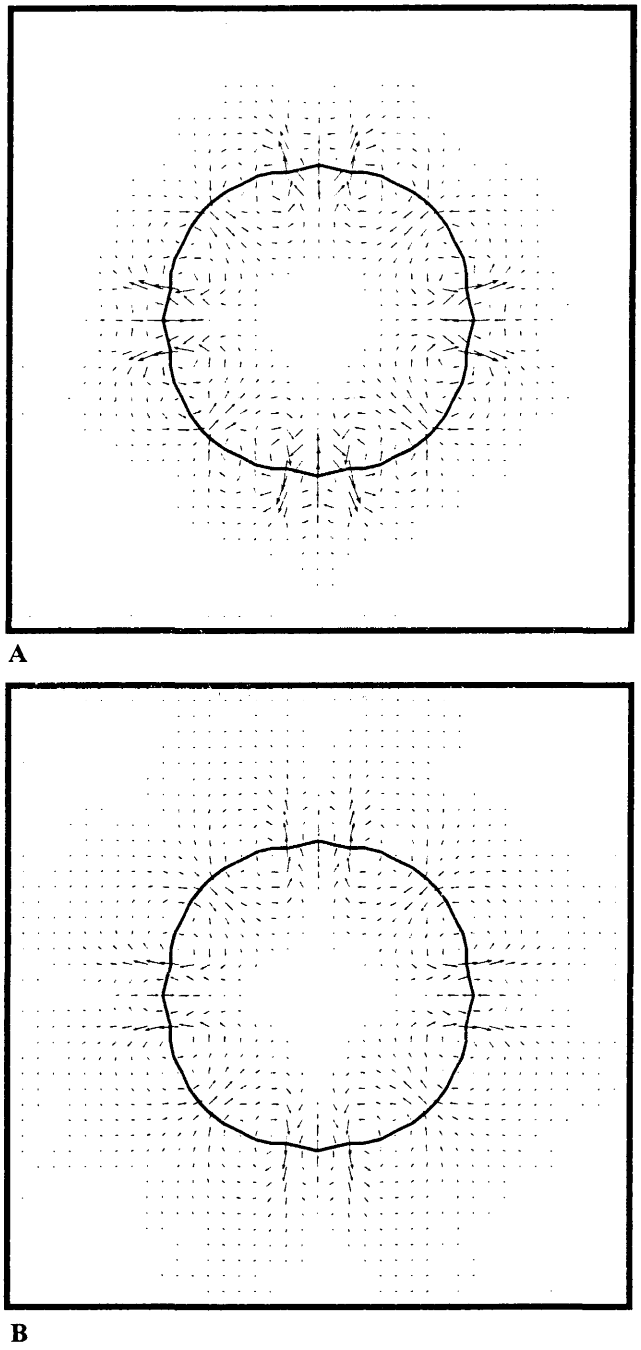

Figure 6.9 Two-fluid, variable viscosity static droplet test. (A) original CSF model (B) modified CSF model. computational run-time, t=10.0 (n)

Figure 6.9 depicts the two CSF model comparison. Notice in 6.9(A) that the surface currents are somewhat larger in magnitude than those shown in 6.9(B). As a result the growth of the velocity field over the entire computational domain is much less. Figure 6.10 shows the growth of TKE for each CSF model.

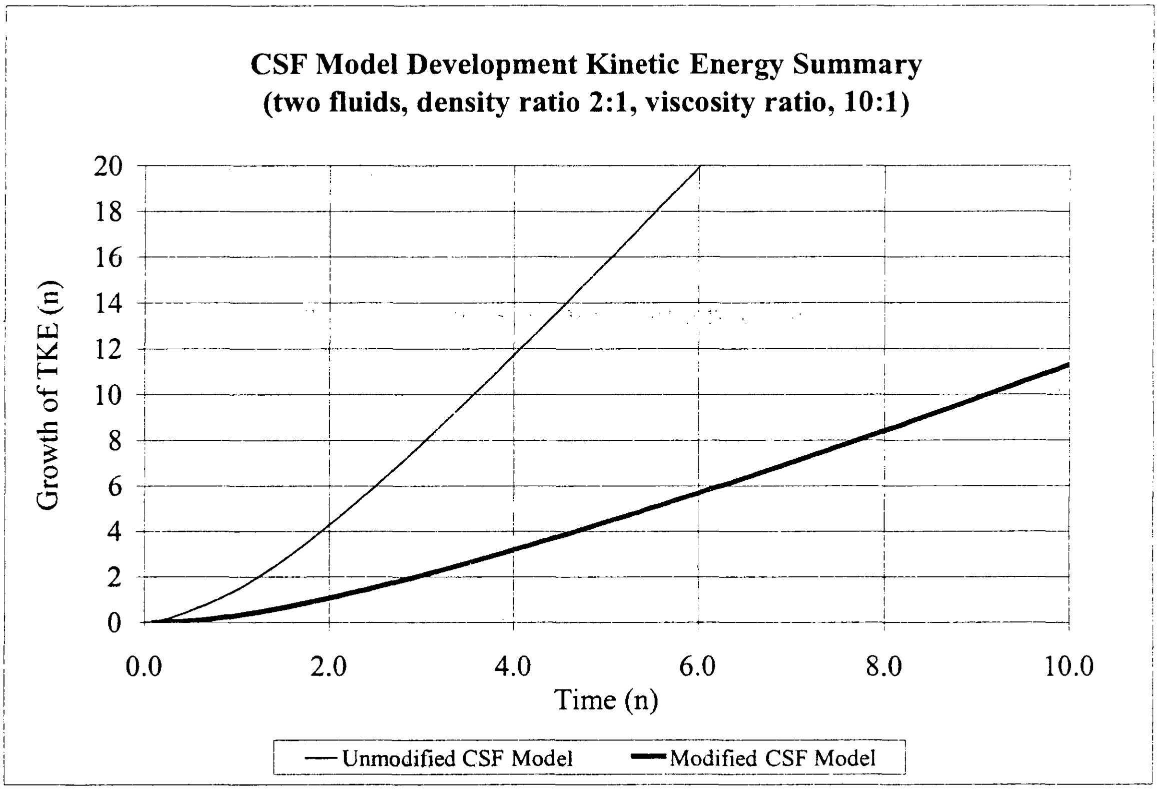

Figure 6.10 Growth of TKE versus time for a static droplet.

The growth of TKE in Figure 6.10 depicts the significant difference between the modified CSF and original model. Clearly, the modifications have improved the code's ability to decrease the propagation of numerical noise that may be introduced into the solution by surface tension forces.

6.5 Heat Transfer Test Cases

The addition of Johnson's (2001) thermal model into RIPPLE, was verified, validated and tested using two different test cases. The integration of the thermal model enables the determination of two-dimensional conduction, convection and radiation. The first test case was identical to the nickel plate test case completed by the researchers during the course of their development. The duplication of this test case ensured that the thermal model as it exists in Johnson's CFD code was properly integrated into the two fluid flow solver. The second test case ensured that the thermal solver accurately included all three modes of heat transfer (i.e. conduction, convection and radiation) in the two fluid model.

6.5.1 The Rectangular Plate

The verification test case used to ensure that the thermal model had been properly integrated into the two fluid RIPPLE model was the steady state heat transfer within a rectangular plate, which was identical to that completed by Johnson (2001).

Two-dimensional, steady state heat conduction in a rectangular plate with three sides at *T1* and on side at *T2* has an exact solution that is obtained by separation of variables (Incropera, 1990) and is given by

$$\theta(x,y) = \frac{2}{\pi}\sum_{n=1}^{\infty}\frac{(-1)^{n+1}+1}{n} sin\left(\frac{nx\pi}{L}\right)\left(\frac{sinh[n(W-y)\pi/L]}{sinh(nW\pi/L)}\right) \tag{6.5}$$

where $\theta=(T-T1)/(T2-T1)$

The analytical solution is compared to the numerical simulation in the particular case of nickel with *L=W=5mm, T1=1900 K* and *T2=1800 K* (in the simulation the initial temperature was chosen to equal T1). Figure 6.11 depicts the analytical and numerical results, which where identical to those obtained by Johnson (2001). All data was gathered at a computational finish time of 1.5 seconds.

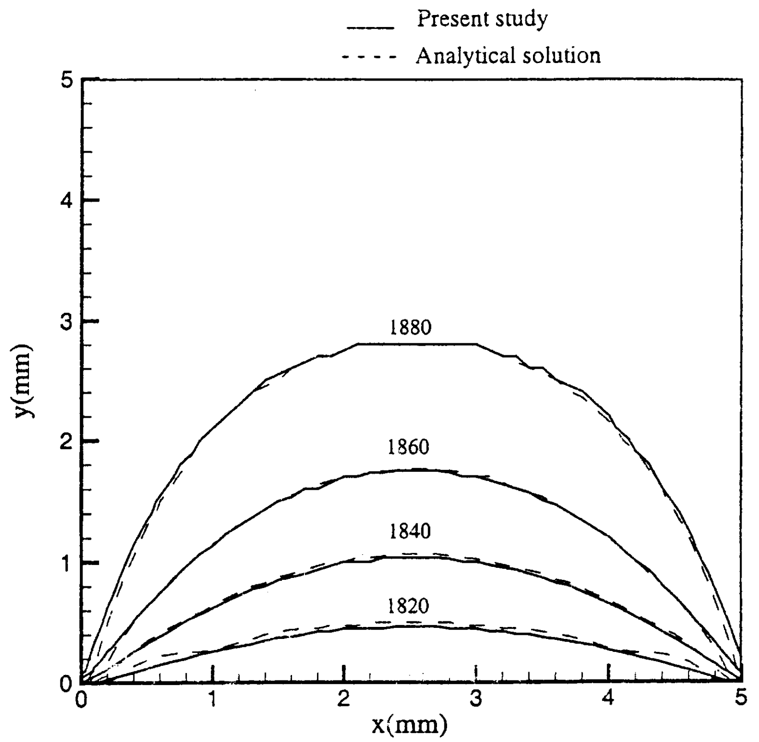

Figure 6.11. Johnson (2001) analytical and numerical nickel plate temperature contour test case results.

6.5.2 The Glass Fiber

In addition to the nickel plate test case that examined only conduction, a glass fiber simulation was completed using the newly modified fluid/thermal solver, which included conduction, convection and radiation heat transfer modes. The simulation modeled the shear interaction between a molten glass filament and a high-speed air jet. The diameter and length of the glass filament were 400 microns and 1 mm, respectively. As shown in Figure 6.12, the temperature of the glass melt entering the die was 1500 K.

The temperature of the high-speed air jet was 1300 K. The inlet temperature within each jet obstacle remained constant throughout the simulation, which explains the uniform inlet temperature shown near the bottom of Figure 6.13(B). The softening temperature of the glass was 1260 K and the density and viscosity ratios were 10:1. The glass surface tension coefficient was 0.03 N/m and the gravity vector was present in the axial (z-axis) direction. The inlet velocities of the glass and air flow were 20 m/sec and 400 m/sec, respectively. The specific heat of the glass and air was 1256 J/kg-K and 1140 J/kg-K and the thermal conductivity and emissivity of the glass were 200 W/m-K and 0.8.

The air/fiber simulation results are shown in Figure 6.13. Figure 6.13(A) depicts the VOF contour of the attenuated glass filament. Figure 6.13(B) shows the temperature contour of the fiber due to conduction, convection and radiation heat transfer. The numerical results of Figure 6.13, indicate the fiber quickly assumes the temperature of the surrounding air due to all three modes of heat transfer. As the simulation progresses, the temperature of the fiber assumes the temperature of the surrounding air. The numerical results show a good comparison to those predicted by the analytical solution for the radial and axial temperature distributions within the filament. The Heisler-Grober charts predict a constant radial temperature distribution within the fiber. Using an approximate solution to predict the temperature distribution within a cylindrical fin in cross flow indicates a decrease in axial temperature along the axis of the fin or fiber in this case. However, the temperature gradient predicted from the cylindrical fin estimate is less than that given from the numerical results. The discrepancy could be attributed to absence of radiative heat transfer in the analytical fin prediction.

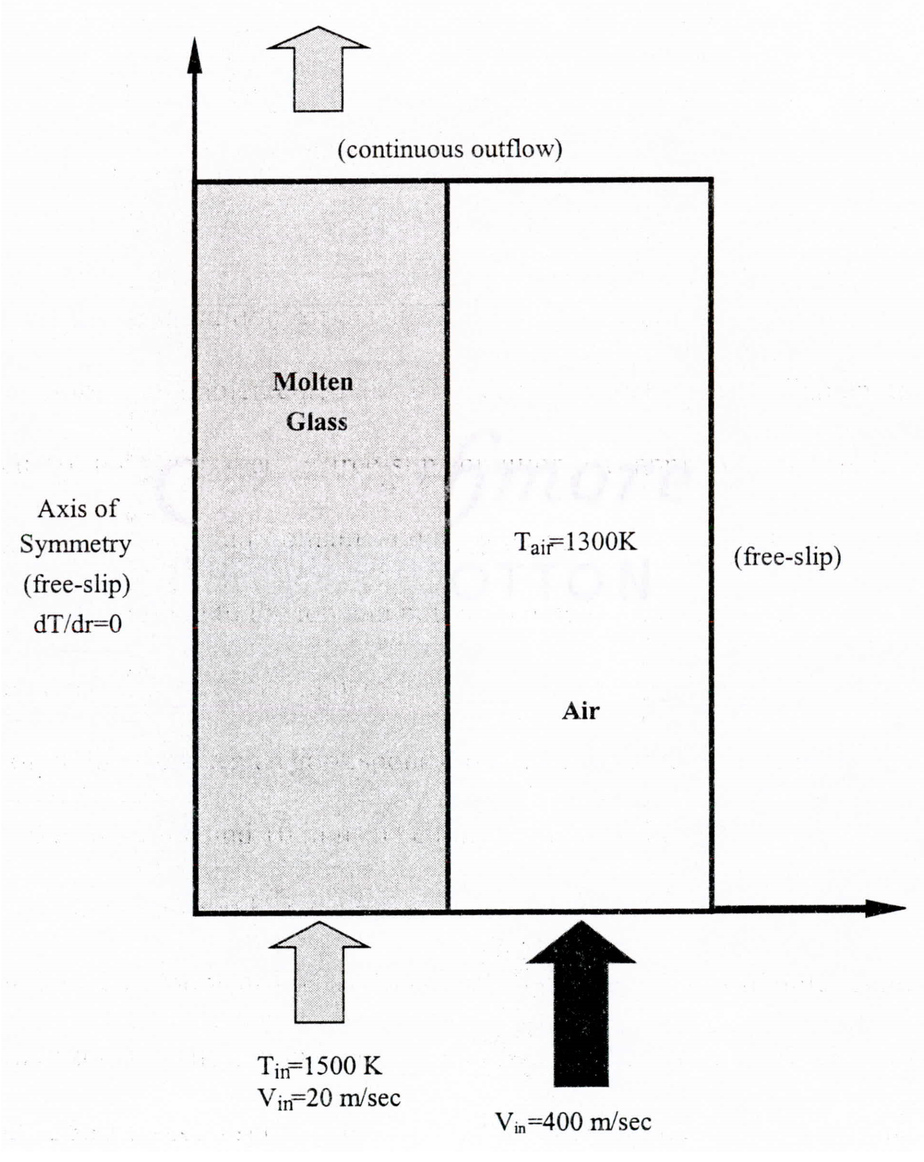

Figure 6.12. Glass fiber test case boundary and initial conditions

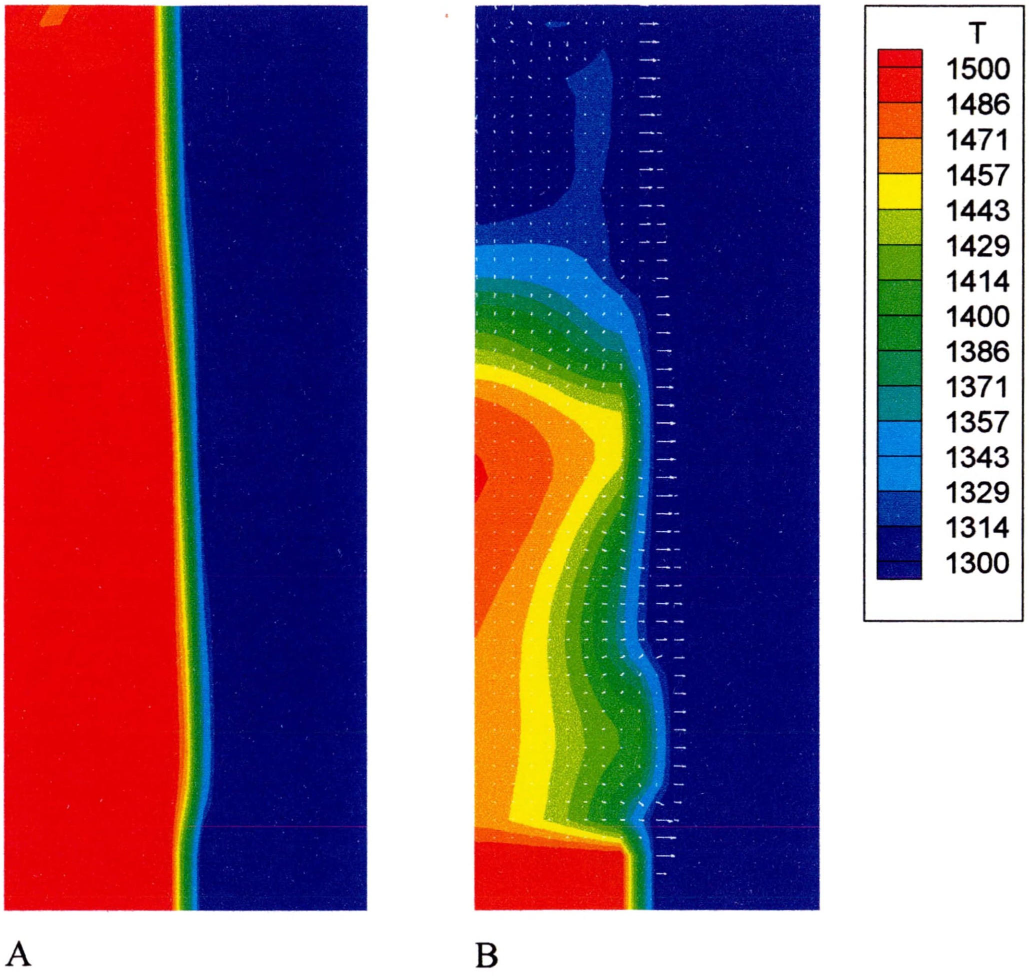

Figure 6.13 Glass fiber thermal test case results, (A) VOF contour, (B) temperature contour (degree K) and heat flux vector plot. Conduction, convection and radiation taken at a computational run-time of 4.0e^{-6} seconds.

6.6 Industrial Process Simulations

The purpose of the investigation into the process of discontinuous glass fiber manufacturing was to characterize the fundamental shear air/fiber interaction through detailed experimental measurements and numerical simulations. The air/fiber interaction, which occurs within the critical region of the rotary spinning process shown in Figure 6.14, provided the basis for the numerical model development.

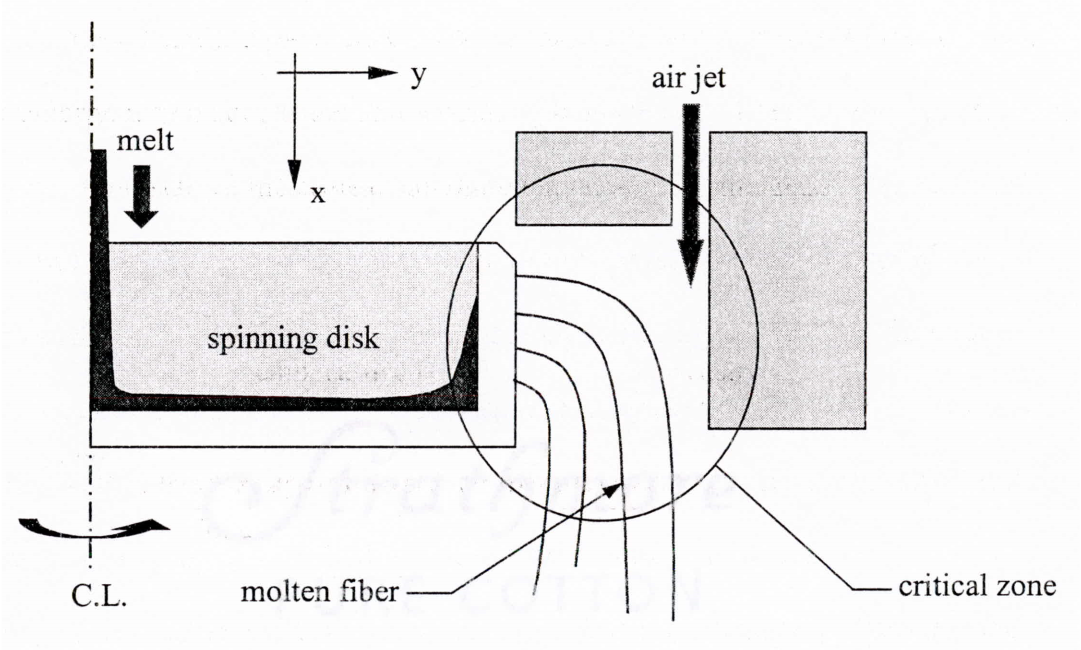

Figure 6.14 Rotary spinning process.

Within the critical zone, several complex interactions occur that influence the formation of glass fibers. The extreme velocity and temperature gradients and subsequent variation in material properties result in a process that is extremely difficult to characterize experimentally. However, improving control of fiber formation requires an intimate understanding of the shear interaction between the molten glass filament and the high-speed air jet.

The shear air/fiber interaction that exists during the process of discontinuous glass fiber manufacturing occurs on both macro and micro scales. The experimental drag force measurements and dynamic analysis of the glass fiber examined the effect of the integral scales of the air turbulence (i.e. the macro-scale interaction). The force transducer characterized a global drag force over the entire length of the glass fiber. The drag force measurements also included the oscillations (flapping) of the fiber tip due to fluctuations of the turbulent air flow. On the contrary, the numerical simulations have targeted the localized micro-scale, shear interaction between the molten glass filament and the high-speed air jet. The numerical simulations completed herein are the first attempts toward applying a specialized CFD code to simulate the shear interaction between two dissimilar fluids comparable to that occurring in the process of discontinuous glass fiber manufacturing. Both experimental and numerical techniques were applied to develop the most complete characterization of the air/fiber interaction known to date.

The following is a summary of the air/fiber test cases simulated using Vi^3S-FLOW.

1. Industrial Process Test Case simulated the maximum or worst case fiber production input parameters and air/glass material property ratios determined at the critical melt temperature of glass.
2. Test Cases A, B and C examined influence of air/fiber momentum ratio on fiber attenuation.

3. Test Case D examined the influence of increased drag force on fiber attenuation by substantially increasing the air jet velocity.
4. Test Case E examined the influence of an additional body force that characterized the tangential centrifugal acceleration of the glass fiber.
5. Test Case F examined the cumulative effect of increased drag and body forces on fiber attenuation.

The boundary conditions of the air/fiber simulation are shown in Figure 6.15. A free-slip condition was implemented along the centerline of the glass filament to exploit the symmetry of the glass fiber. A free-slip condition was applied to the right boundary, which indicates an infinite air domain, and a continuous outflow condition and inlet air/glass jets were applied to the top and bottom boundaries, respectively. The computational mesh density varied between 5,000 and 10,000 cells with a radial and axial resolution of 20 microns, which corresponds to a fiber diameter of 400 microns and filament lengths of 5 mm and 10 mm. The inlet temperature of the molten glass and high-speed air jet were 1500 K and 1300 K, respectively. The temperature of the surround process environment was assumed to be 800 K and the softening temperature of the glass was 1260 K. The conductivity (k) and specific heat (C_p) of the glass were 2.0 W/m-K and 1256 J/kg-K, respectively. In each air/fiber simulation the smoothing length (h), required by the CSF model, was two and one-half times the minimum cell size and the associated smoothing length error (Δh) was 10% of the smoothing length.

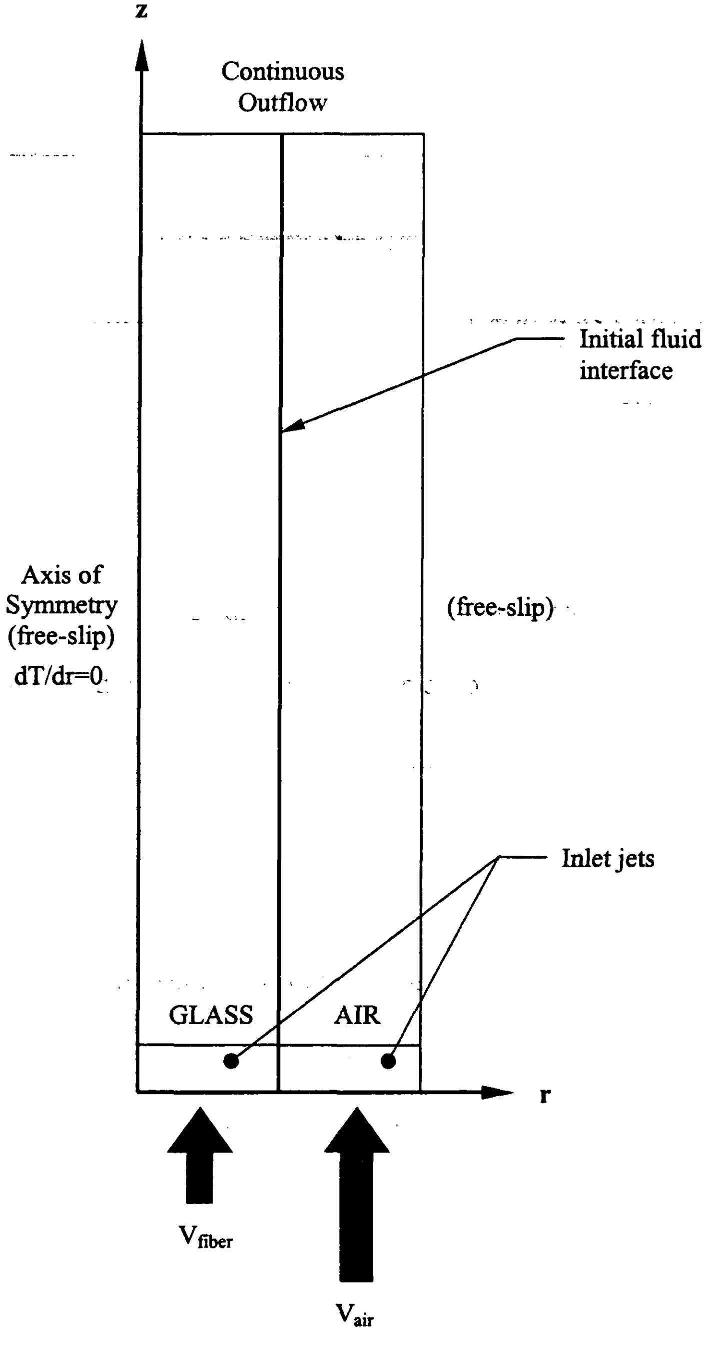

Figure 6.15. Air/glass simulation input boundary conditions

6.6.1 Industrial Process Test Case

Table 6.3 summarizes the "worst" case input parameters used in the production of discontinuous fibers made from typical E-glass. A critical factor in glass manufacturing is the dependence of glass viscosity on temperature, as shown in Figure 6.16. Although glass is amorphous and does not solidify from a liquid to a solid, the terms will be used to describe the fluid state at the critical softening temperature of the glass.

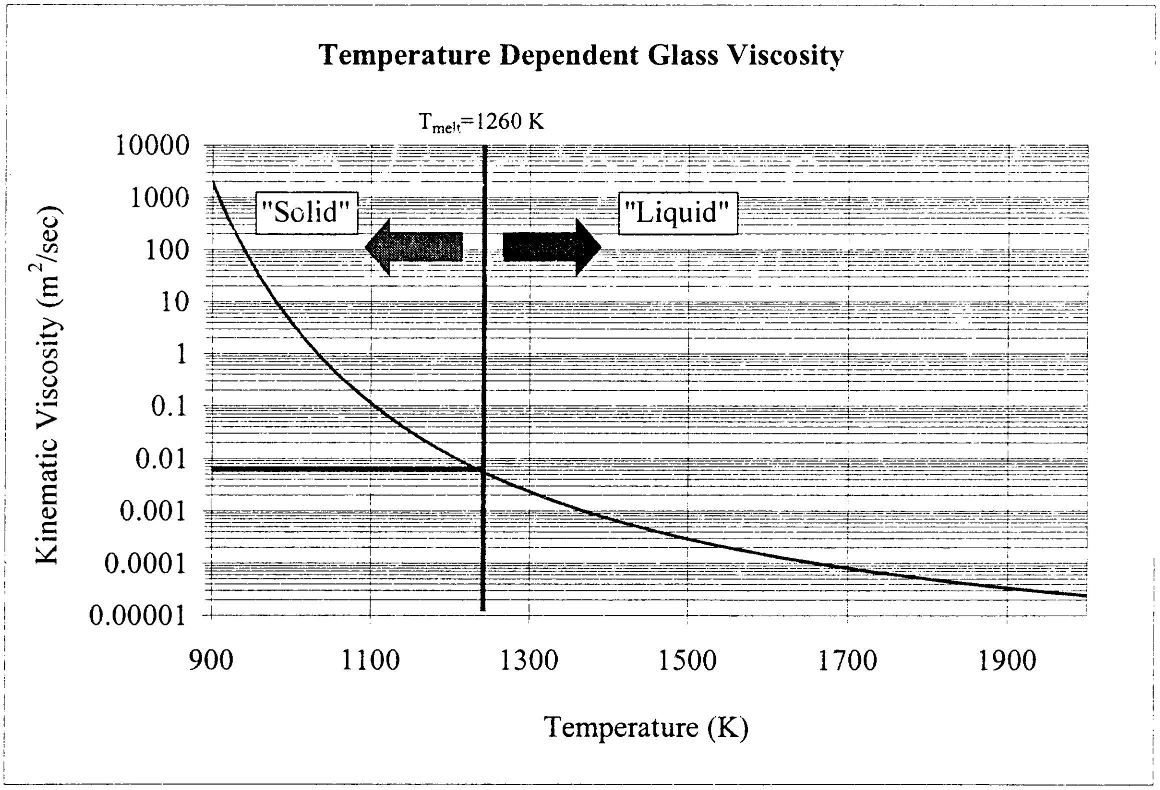

Figure 6.16 Temperature dependent glass kinematic viscosity.

Initial estimates of Reynolds number (Re_d=1.9), based on the worst case parameters, indicate that the glass flow is within the creeping flow regime, while the high-speed air flow remains laminar (Re_d=1280). Creeping flow occurs when $Re_d \ll 1$, however the transition occurs over a range of Reynolds numbers and the effects are most likely to occur well before the specified limit. Creeping flow is characterized by a negligible pressure gradient due to decreased convective acceleration, thus advection and pressure are neglected in the momentum equations and viscous forces dominate the flow. Vi^3S-FLOW, which does not compensate for creeping flow, may produce erroneous results within the creeping flow regime (Kothe, 1999). CFD analyses often requires the use of several specialized codes to address specific creeping and compressible flow regimes. In general, a compressible flow can not be accurately modeled using a CFD code developed to simulate incompressible or creeping flows.

In addition to the difficulties associated with simulating a creeping flow, further problems may arise due to the large density, velocity and viscosity ratios, which occur on the micro-scale of the fiber. Although density and viscosity ratios of 20,000:1 and 25:1 have been successfully modeled on larger scales using Vi^3S-FLOW (see Section 6.3), the application of such extreme gradients in a micro-scale environment may provide excessive resistance to the flow. Resolving the large gradients could also result in convergence failures, time step constraints and similar errors.

Table 6.3 Industrial Process Input Parameters

	density (kg/m^3)	**viscosity (m^2/sec)**	**velocity (m/sec)**	**momentum (kg-m/sec)**
air T=1000 K	0.34	1.3E-04	400	5.4E-08
glass T=1260 K	2633	4.1E-03	20	2.1E-05
air/glass ratio	1.3e-4:1	0.03:1	20:1	0.003:1

The fluid properties shown in Table 6.3 were determined at the critical transition temperature of the generic E-glass used throughout the numerical analysis. The simulation was completed on a 20x250 mesh, corresponding to a fiber diameter and length of 400 microns and 5 mm, respectively. The surface tension coefficient was 0.3 N/m and the gravity vector was included in axial direction. The results of the simulation are shown in Figure 6.18.

The glass filament presented no indications of necking, but rather exhibited a behavior similar to the Kelvin-Helmholtz instability (KH), which is characterized by the phenomenon of breaking waves as shown in Figure 6.17. The figure shows the experimental results of the KH instability of superposed streams (Dimotakis and Roshko). The upper stream of water is moving to the right faster than the lower one, which contains the dye that fluoresces under illumination by a vertical sheet of laser light.

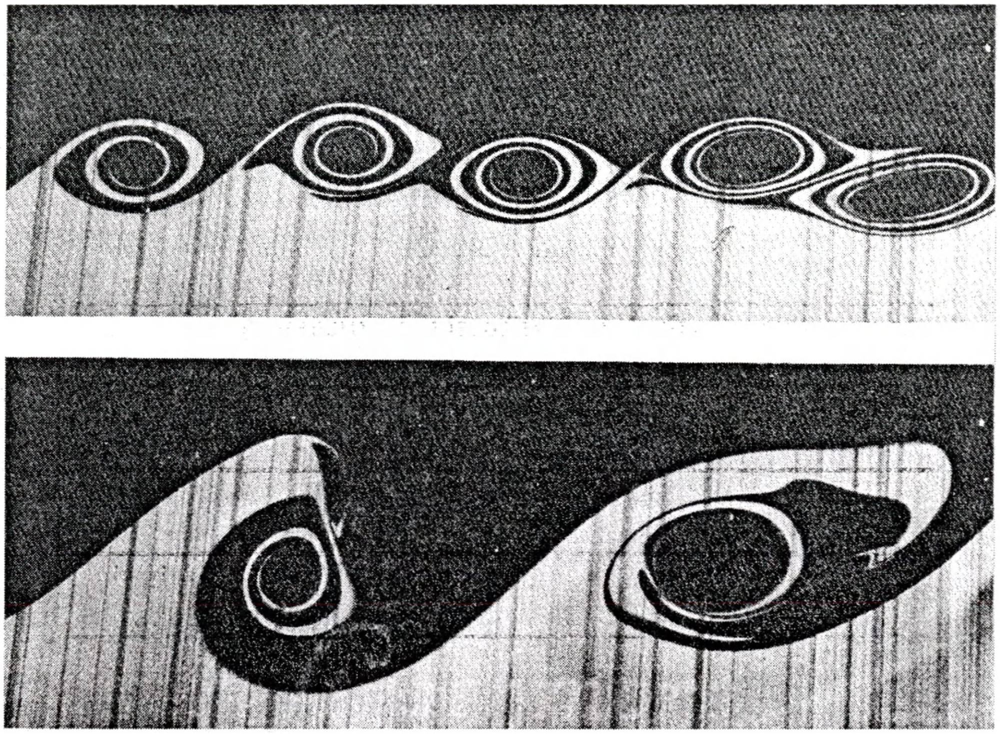

Figure 6.17 Kelvin-Helmholtz instability. Image taken from An Album of Fluid Motion (Van Dyke, 1998). Experiment completed by Dimotakis and Roshko.

The inability of the fiber to attenuate can be attributed to several factors, mainly Vi^3S-FLOW's inability to accurately simulate creeping flows. Recall that the Reynolds number is approximately 1.9, which indicates the onset of creeping flow. The momentum of the air/fiber system also provides an indication of potential necking within the glass filament. The momentum of the air and glass were estimated using the average inlet velocity and mass of each fluid within a single computational cell. As shown in Table 6.3, the momentum of the glass is greater than that of the air, which results in the glass dominating the flow field. Alternatively, the velocity of the high-speed air jet may not have been large enough to produce the drag force necessary to produce fiber attenuation. The surface area of the fiber, which is directly related to fiber length, may also have not been large enough to produced the desired drag force to promote the onset of necking. A potential solution would be to increase the length of the fiber, which would increase the effective surface area and resulting drag force at the expense of additional computational run-time. Instead, the material properties and velocity of the high-speed air jet were modified to induce fiber necking, while not increasing the length of the fiber and corresponding simulation run-time.

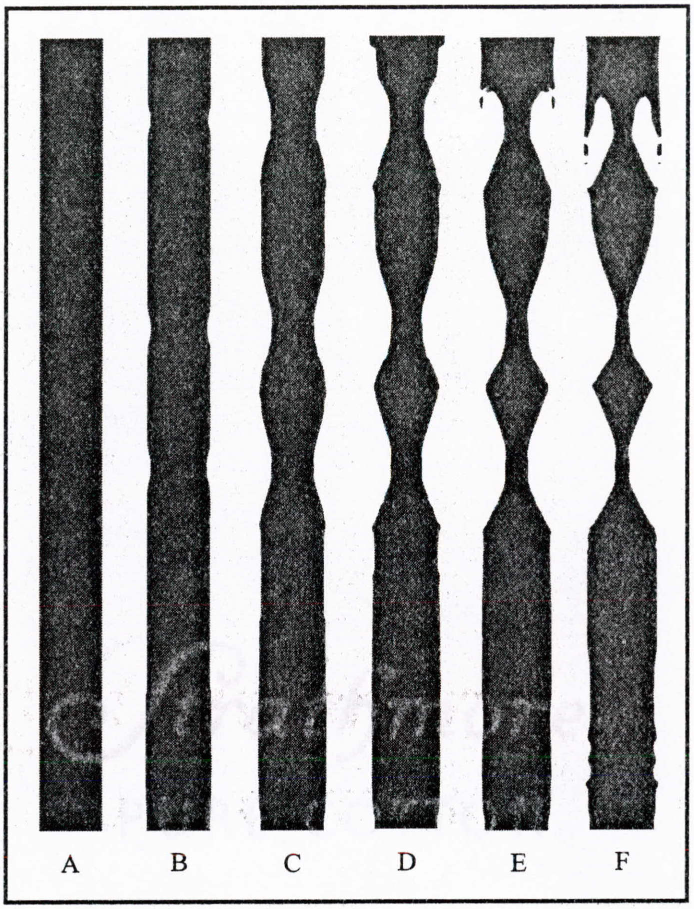

Figure 6.18 Industrial process simulation results.
Interface represented by VOF contour, Figure 6.18 A, B, C, D, E and F correspond to computational run-times of 0.0, 1.0e^{-9}, 3.0e^{-8}, 5.0e^{-8}, 7.0e^{-8} and 9.0e^{-8} seconds.

6.6.2 Test Case A

As a result of the worst case simulation, the Reynolds number (Re_d) of the glass flow was increased to ensure the that the flow was within the laminar regime. The diameter and length of the fiber remained unchanged (i.e. dia=400 microns, L=5 mm), as well as the inlet velocities of the two fluids. However, the viscosity and density of the air and glass were modified, as shown in Table 6.4.

Table 6.4 Test Case A Input Parameters.

	density (kg/m^3)	**viscosity (m^2/sec)**	**velocity (m/sec)**	**momentum (kg-m/sec)**
air	10	1.0E-04	400	1.6E-06
glass	100	1.0E-03	20	8.0E-07
air/glass ratio	0.1:1	0.1:1	20:1	2:1

In general, V*i*^{3}S-FLOW is capable of simulating incompressible two fluid flows with density and viscosity ratios of 20,000:1 and 25:1, respectively. However, the large ratios applied to the micro-scale of the fiber resulted in increased computational run-time as well as providing additional difficulties (such as increased flow resistance) to the CFD model. For simplicity, as well as the development of a baseline for future air/fiber simulations, the density and viscosity ratios were decreased to 10:1. The magnitude of the glass kinematic viscosity was chosen to ensure laminar flow in each of the simulations test cases. The density was arbitrarily chosen. The magnitude of density and viscosity in the industrial process simulation were approximately equal to those of a glass approaching its softening point in industrial fiberizing processes. However, the severity of the density and viscosity gradients and the surface tension coefficient presented excessive resistance within the flow field, which increases with decreasing temperature of the glass. Thus, the magnitudes of the density and viscosity were decreased so that the focus of the simulations remained on resolving the shear interaction between the two fluids and the phenomenon of necking, rather than resolving the extreme gradients on the micro-scale of the glass filament.

The remainder of the test cases presented herein included a gravity vector in the axial (or positive z-axis) and a surface tension coefficient of 0.03 N/m. The surface tension coefficient was also decreased by a factor of ten from the industrial process simulation. The resulting Reynolds number (Re_d) of the glass based on the modified properties of Table 6.4 was 8.0, which indicates laminar but not creeping flow. The high-speed air jet remained laminar. The input temperatures of the air/fiber system remained unchanged, as well as the computational mesh. The diameter and length of the glass filament were 400 microns and 5 mm, respectively.

Figure 6.19 Test Case A air/glass simulation results.
Interface represented by VOF contour, Figure 6.19 A, B, C, D, E and F correspond to computational run-times of 0, $4e^{-6}$, $1.2e^{-5}$, $2.0e^{-5}$, $3.6e^{-5}$, and $5.0e^{-5}$ seconds.

The results of Test Case A indicate attenuation, unlike the previous creeping flow results of the Worst Case Test Case. The interface instability produces attenuation, break-up and the formation of satellites or "shot". A careful distinction must be made that clearly identifies the phenomenon depicted in Figure 6.19. The utility of Vi^3S-FLOW lies within its ability to simulate the shear interaction between the high-speed air jet and the molten glass filament. However, the mechanism attributed to break-up of the VOF field cannot be identified with the current code. The break-up phenomenon of the glass filament requires further characterization that should be completed on a more refined mesh to resolve the smallest localized scales of motion that occur at the interface between the two fluids. V*i*^{3}S-FLOW should only be used to examine the shear interaction occurring at the interface and potential for attenuation and necking.

The momentum ratio provides a measure to access the potential for attenuation and necking between the two fluids in the simulation. In the industrial process simulation (see Table 6.3) the momentum of the glass was greater than that of the air, which indicated that the glass dominated the flow field. The air did not possess sufficient momentum to influence the propagation of the molten glass through the computational domain. In Test Case A (see Table 6.4) the air/glass momentum ratio was greater than one, indicating that the high-speed air jet dominated the flow field subsequently producing attenuation of the glass filament.

The temperature contour taken at $1.2e^{-5}$ seconds (corresponding to Figure 6.24(C)) is shown in Figure 6.20. The numerical results indicate that the temperature of the glass fiber quickly approaches the temperature of the surrounding air. Theoretical solutions of the axial temperature distribution in a cylindrical fin in cross flow predict similar results (Incropera and DeWitt, 1990). However, radiation heat transfer was neglected in those predictions. In each of the following test cases, the thermal properties (i.e. temperature, conductivity, specific heat, etc.) of the air and glass remained unchanged. The temperature dependent glass viscosity is the most critical factor in the production of discontinuous fibers. The glass viscosity is also one of the key factors in developing a successful numerical simulation of the spinning process. As the glass viscosity increases due to decreases in temperature, the resistance to flow within the glass increases proportionally. The increase in viscosity as the glass approaches the critical softening temperature, results in creeping flow which Vi^3S-FLOW is unable to accurately model. Although there is a need to include the non-Newtonian behavior of the glass into a comprehensive CFD model, Vi^3S-FLOW is not equipped to resolve such interactions and is limited to the laminar/turbulent flows. The alternative is to increase the glass viscosity just enough to ensure laminar flow while minimizing the deviation from the material and process parameters implemented in the industrial spinning process. Since the fluid and thermal solver are de-coupled (see Section 6.5), the viscosity of the glass will remain constant. The temperature contours for each of the remaining simulations will also be omitted as the results indicate that the molten glass filament quickly assumes the temperature of the surrounding environment as the glass filament attenuates.

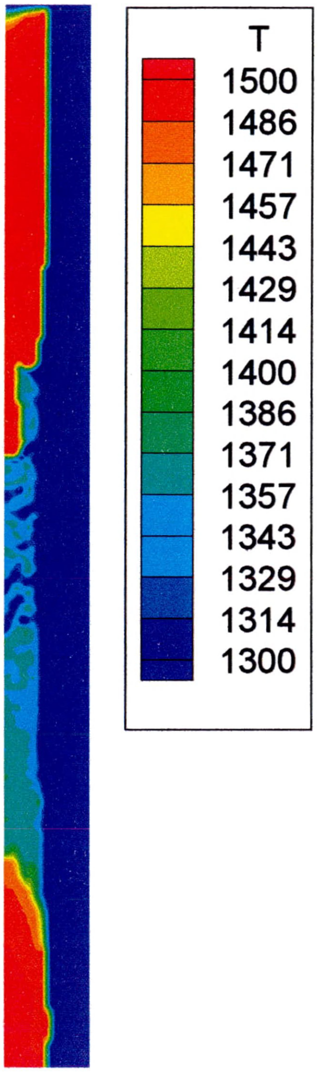

Figure 6.20 Test Case A air/glass temperature (degrees K) contour at a computational run-time of 1.2e^{-5} seconds.

6.6.3 Test Case B

The results of the first two test cases indicate that a decrease in the momentum of the air jet produces an instability similar to the KH instability that indicates potential break-up of the glass filament without noticeable attenuation. In the Industrial Process Test Case the momentum of the air was less than that of the glass and the glass flow fell within the creeping flow regime, which may have biased the results. To further test the air/fiber momentum argument, the ratio was decreased from 2:1 of Test Case A to 0.2:1 as shown in Table 6.5. The momentum of the air jet was decreased by decreasing the density of the air from 10 kg/m^3 to 1kg/m^3. The simulation was completed on a 20x250 computational grid with a resolution of 20 microns. The fiber diameter and length were 400 microns and 5 mm, respectively. The surface tension coefficient was 0.03 N/m and the gravity vector was included in the simulation.

Table 6.5 Test Case B Input Parameters

	density (kg/m^3)	**viscosity (m^2/sec)**	**velocity (m/sec)**	**momentum (kg-m/sec)**
air	1	1.0E-04	400	1.6E-07
glass	100	1.0E-03	20	8.0E-07
air/glass ratio	0.01:1	0.1:1	20:1	0.2:1

The results shown in Figure 6.21 coincide with the momentum prediction. If the air/glass ratio is less than one (i.e. the momentum of the air is less than the momentum of the glass) the glass dominates the flow field and attenuation of the filament is unlikely.

The results of Test Case B indicate the development of an instability similar to the KH instability, which also appeared in the industrial process test case.

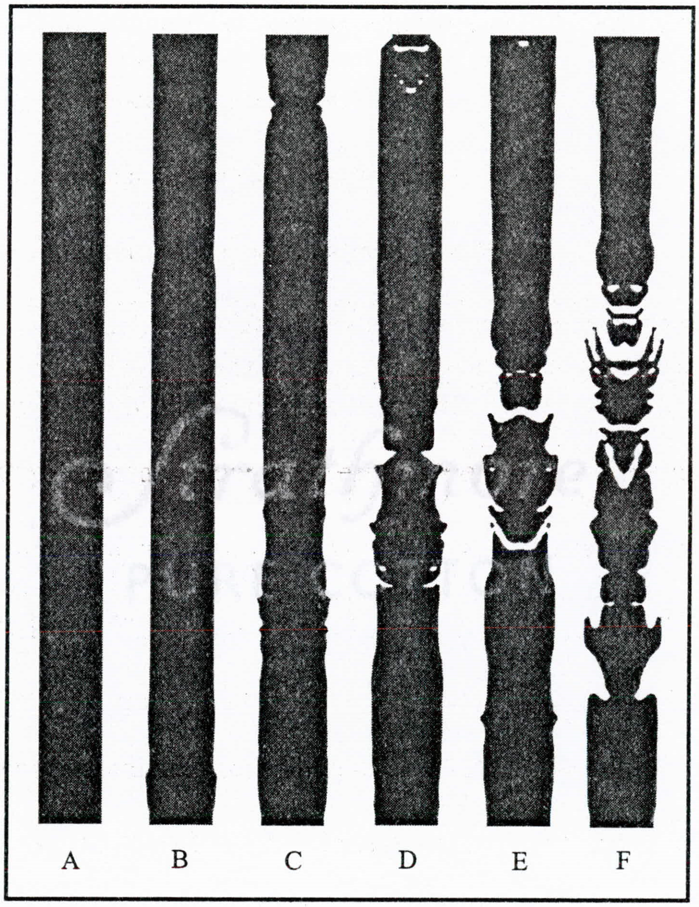

Figure 6.21 Test Case B air/glass simulation results.
Interface represented by VOF contour, Figure 6.21 A, B, C, D, E and F correspond to computational run-times of 0, $2.0e^{-6}$, $6.0e^{-6}$, $8.0e^{-6}$, $1.0e^{-5}$, and $1.3e^{-5}$ seconds.

6.6.4 Test Case C

To further test the momentum prediction, the density of the air was increased, while holding all other input parameters constant. The increase in the air/glass momentum ratio was 10 times greater than the momentum ratio of Test Case A. The input parameters of Test Case C are shown in Table 6.6.

Table 6.6 Test Case C Input Parameters

	density (kg/m^3)	**viscosity (m^2/sec)**	**velocity (m/sec)**	**momentum (kg-m/sec)**
air	100	1.0E-04	400	1.6E-05
glass	100	1.0E-03	20	8.0E-07
air/glass ratio	1:1	0.1:1	20:1	20:1

The results of the simulation are shown in Figure 6.22. The glass filament begins to attenuate and necking occurs slightly before that shown in Test Case A (see Figure 6.19). A comparison of the results from Test Case A and C indicate that the onset of necking occurs slightly before that shown in Test Case A due to the increase in momentum of the air jet.

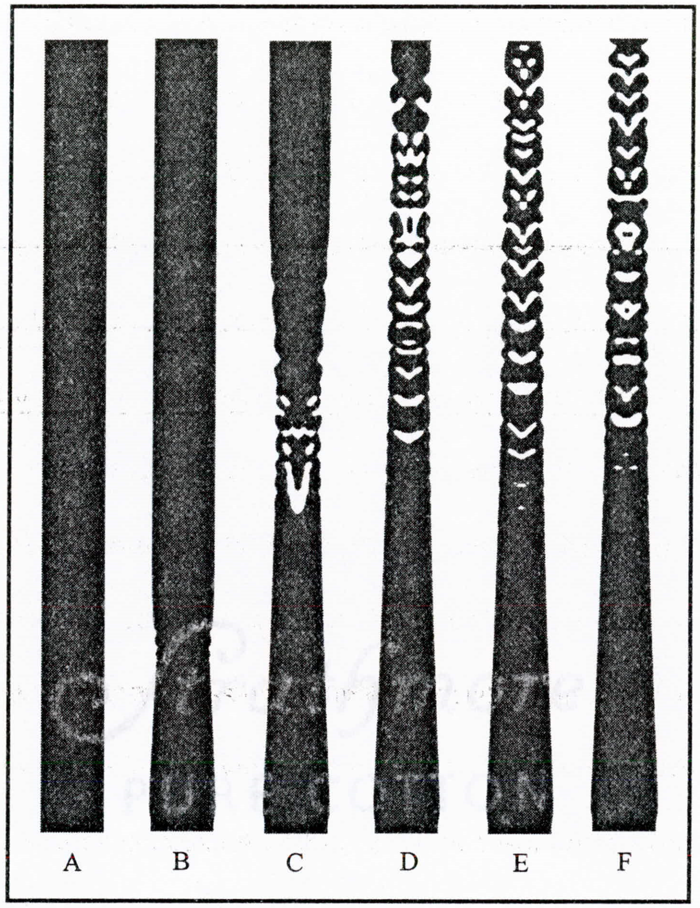

Figure 6.22 Test case C air/glass simulation results.
Interface represented by VOF contour, Figure 6.22 A, b, C, D, E and F correspond to computational run times of 0, $4e^{-6}$, $1.2e^{-5}$, $2.0e^{-5}$, $3.6e^{-5}$, and $5.0e^{-5}$ seconds.

Given the results of the four previous test cases (i.e. Industrial Process, A, B and C) the effects of the air/glass momentum ratio greatly influence the shear interaction between the two fluids. For air/glass momentum ratios greater than one the onset of necking is likely to occur, while air/glass ratios less than one produce a phenomenon similar to the KH instability that results in potential break-up of the glass filament without measurable attenuation. Although the CFD model is capable of predicting attenuation and necking of the glass filament, further characterization is required to determine the exact break-up mechanism of the filament. The portion of the simulation results that indicate potential break-up remain questionable. The model is capable of predicting the behavior of the glass filament from the inlet of the computational domain to the first point of potential break-up, but following that the model must be refined to accurately characterize the break-up phenomenon. Each previous test cases has provided valuable information for predicting attenuation of the glass filament, however the simulations do not specifically target the degree of attenuation and necking of the glass filament.

In practice, industrial rotary spinning processes that operate under conditions similar to those listed in Table 6.3, produce fibers of various lengths and diameters. In this process the fibers are extruded from exit holes in the spinning disk sidewall, which vary in size from several hundred microns, resulting in attenuated fibers from 5 to 50 microns. Although necking is present in several of the numerical test cases, it is not as severe as that seen in industrial fiberizers. The discrepancies may attributed to several factors, two of which will be examined in the following test cases. In industrial rotary spinning processes the fibers produced reach lengths nearing 0.05 meters. However, the numerical simulations examined the attenuation of 5 and 10mm fibers. The drag force acting over the length of fiber may not have been sufficient enough to produce the large attenuation and subsequent change in diameter as observed in industrial processes. Several additional effects must be examined to produce the desired attenuation as it occurs in industry. Two primary contributions that are believed to promote fiber attenuation and necking are the integrated change in drag force over fiber length and the centrifugal acceleration of the fiber. Neither are included in the current model, however increasing the drag force (F_d) and adding a body force (F_ω) due to centrifugal acceleration will determine the importance of each in the air/fiber model. The addition of the drag and body forces enables the simulation of much smaller glass filaments without increasing the computational domain and associated run-time associated with simulating a 0.05 meter fiber. The drag and body forces will be substantially modified by increasing the high-speed air jet velocity and adding an additional body force due to the centrifugal acceleration of the molten glass filament. Test Case D will examine the effect of increased air drag on the fiber by increasing the velocity of the air jet while holding all other model parameters constant. Test Case E will examine the effects of adding an additional body force due to the centrifugal acceleration of the glass filament while holding all other input parameters constant.

6.6.5 Test Case D

The fiber drag force (see equation 6.6) is a function of the surface area of the glass fiber, air density and velocity. The drag force can be increased by increasing the density of the air, the surface area of the glass fiber and/or the velocity of the air. Holding the fiber diameter constant, an increase in surface area would require a longer length of fiber. However, an increase in fiber length occurs at the expense of additional computational run-time do to the associated increase in length of the computational domain. If the density of the air remains constant, the alternative to increasing the drag force is to increase the velocity of the high-speed air jet.

$$F_d = \frac{C_f \rho_a A_S V^2}{2} \tag{6.6}$$

The velocity of the ambient air as it passes through the high-speed air jet nozzle is characterized as choked flow. The temperature of the air is assumed to be approximately 293 K, which corresponds to a maximum velocity of approximately 400 m/sec. If the air temperature were increased the maximum velocity of the high-speed air jet could theoretically approach 700 m/sec. If the air flow is choked, the velocity of the air jet cannot exceed 700 m/sec unless the orifice of the jet or the air temperature were increased. However, to examine the effects of air drag (i.e. by increasing air velocity) on the fiber the velocity of the air jet was increased to approximately 1000 m/sec to promote attenuation of the fiber. All other material properties remained constant and are given in Table 6.7.

Table 6.7 Test Case D Input Parameters.

	density (kg/m^3)	**viscosity (m^2/sec)**	**velocity (m/sec)**	**momentum (kg-m/sec)**
air	10	1.0E-04	1000	4.0E-06
glass	100	1.0E-03	20	8.0E-07
air/glass ratio	0.1:1	0.1:1	50:1	5:1

The results of the simulation are shown in Figure 6.23. Increasing the air velocity from 400 m/sec to 1000 m/sec resulted in further necking of the glass filament due to the increased drag force. There was less break-up of the glass filament than in the previous test cases. Although, unlike the previous test cases which demonstrated fiber attenuation, small scale instabilities developed at the interface. The instabilities were similar to the KH instability, but may have been due to disturbances at the interface that developed during the initial phases of the test case. Regardless of the cause, the instabilities eventually dissipated over time.

The addition of the increase in drag force resulted in a final diameter of approximately 256 microns, which corresponded to a 36% decrease in diameter over 5 mm. The simulation computational run-time was approximately 3600 seconds (1 hour).

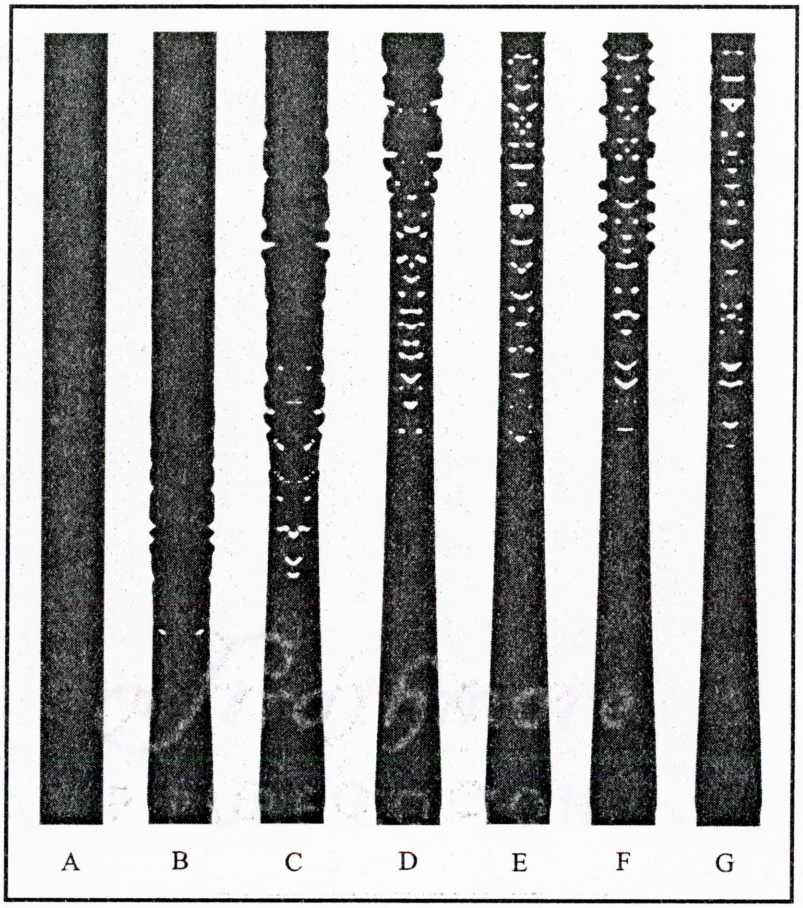

Figure 6.23 Test case D air/glass simulation results.
Interface represented by VOF contour, Figure 6.23 A, B, C, D, E, F and G correspond to computational run-times of 0, $3.0e^{-6}$, $6.0e^{-6}$, $1.0e^{-5}$, $1.2e^{-5}$, $1.4e^{-5}$ and $1.8e^{-5}$ seconds.

6.6.6 Test Case E

Additional attenuation of the molten glass filament was achieved by adding an additional body force due to centrifugal acceleration. The body force (F_{ω}), which is similar to the body force due to gravitational acceleration (g), was added to the Navier-Stokes equations shown in equation 6.7.

$$\frac{\partial \bar{V}}{\partial t} + \nabla \cdot (\bar{V}\bar{V}) = -\frac{1}{\rho}\nabla p + \frac{1}{\rho}\nabla \cdot \tau + \bar{g} + \frac{1}{\rho}\bar{F}_b + \bar{F}_{\varpi} \tag{6.7}$$

The average rotational speed of a 0.508 meter diameter disk in rotary spinning processes is approximately 2000 rpm (150 radian/sec), which results in a centrifugal tangential acceleration or equivalent body force given as

$$F_{\varpi} = \varpi^2 \left(r_{disk} + z\right) \tag{6.8}$$

where ω is the rotational speed of the disk, r_{disk} is the radius of the disk and z is the axial position along the fiber. The results of the simulation are shown in Figure 7.24. It should be noted that initial simulations which included a body force equivalent to a rotation speed of 150 radian/sec did not produce significant attenuation of the 5 mm long fiber. Measurable attenuation of the glass filament was only achieved when the angular rotation of the disk was increased by a factor of 1000 and the glass filament length was increased to 10 mm. The addition of the body force is equivalent to pulling on the glass fiber with approximately 220 N. Although somewhat large, the addition of the body force identifies the importance of centrifugal acceleration in the attenuation process.

The input parameters of the test case are shown in Table 7.6. The density and viscosity ratio remained unchanged, as well as the inlet velocities of the air/fiber system.

The test case was completed on a 20x500 grid with a resolution of 20 microns. The fiber diameter and length were 400 microns and 10 mm, respectively.

The results are shown in Figure 6.24. Aside from the initial surface perturbations that occurred following the initial phases of the simulation, the attenuation was continuous with few variations in the VOF data, as opposed to earlier test cases. After examining the necking of the glass filament, it may be hypothesized that the formation of discrete glass fibers are likely following repeated break-up and necking of the glass filament. On the contrary, this phenomenon may be attributed to the initial conditions of the simulation. The addition of the body force resulted in a final diameter of approximately 288 microns, which corresponds to a 28% decrease in diameter over 10 mm. The simulation computational run-time was approximately 21,600 seconds (6 hours).

Table 6.8 Test Case E Input Parameters

	density (kg/m^3)	**viscosity (m^2/sec)**	**velocity (m/sec)**
air	10	1.0E-04	400
glass	100	1.0E-03	20
air/glass ratio	0.1:1	0.1:1	20:1

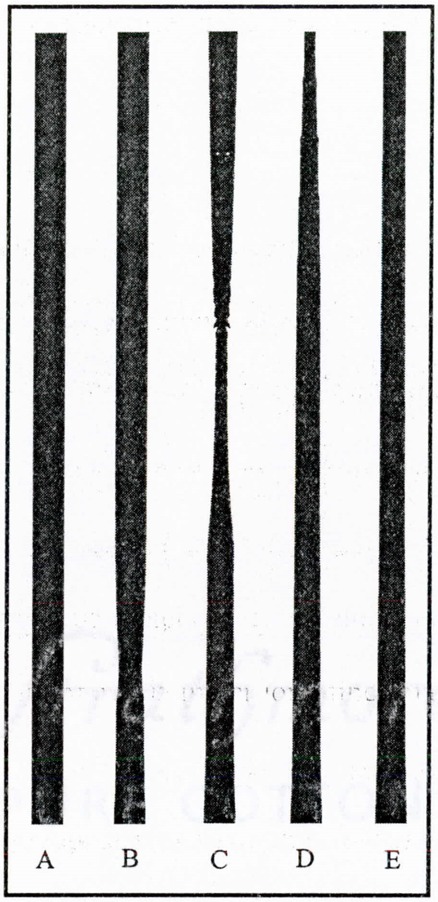

Figure 6.24 Test case E air/glass simulation results.
Interface represented by VOF contour, Figure 6.24 A, B, C, D and E correspond to computational run-times of 0, 1.0e^{-6}, 2.0e^{-6}, 3.5e^{-6} and 9.0e^{-6} seconds.

6.6.7 Test Case F

The final test case examined the cumulative effect of both the drag force (F_d) and body force (F_ω) on fiber attenuation. The input parameters for the test case are shown in Table 6.9. The test case was completed on a 20x500 mesh with a resolution of 20 microns, which corresponded to a fiber diameter and length of 400 microns and 10mm, respectively. The surface tension coefficient was 0.03 N/m and a gravity vector was included in the vertical direction.

Table 6.9 Test Case F Input Parameters

	density (kg/m^3)	**viscosity (m^2/sec)**	**velocity (m/sec)**
air	10	1.0E-04	1000
glass	100	1.0E-03	20
air/glass ratio	0.1:1	0.1:1	50:1

The results of the test case are shown in Figure 6.25 and are similar to those reported in Test Case E. The glass filament experiences constant necking following initial interface perturbations which eventually dissipate with time. As discussed previously, the observed necking may be an artifact of the initial conditions of the simulation. The addition of both body and drag forces resulted in a final diameter of approximately 320 microns, which corresponds to a 20% decrease in diameter over 10 mm. The computational run-time was approximately 16,200 seconds (4.5 hours).

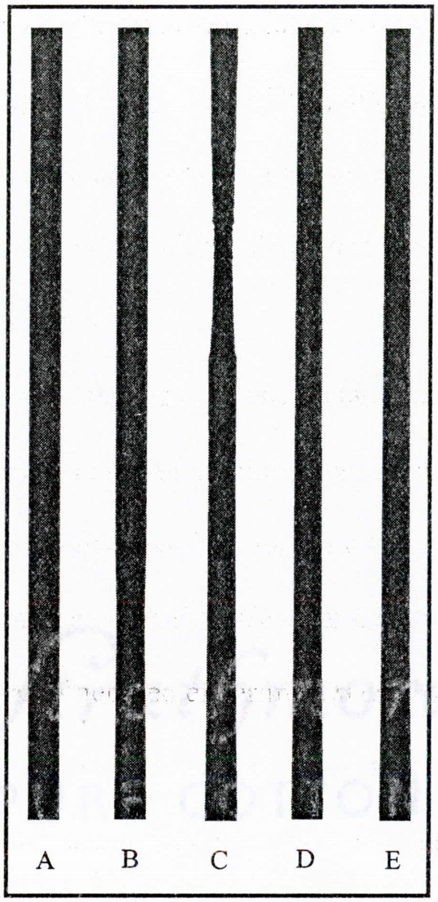

Figure 6.25 Test case F air/glass simulation results.
Interface represented by VOF contour, Figure 6.25 A, B, C, D and E
correspond to computational run-times of 0, 1.0e^{-6}, 2.0e^{-6}, 3.5e^{-6} and 7.5e^{-6} seconds.

6.6.8 Discussion of Results

The initial industrial process estimate of fiber formation indicates that further development of the CFD code Vi^3S-FLOW is necessary before accurate results can be achieved when modeling the process as is occurs in industry. Several difficulties arose during the simulation which included extreme density and viscosity gradients on the fiber micro-scale, which ultimately provided excessive resistance to the flow field. Vi^3S-FLOW is not capable of simulating creeping flows. Thus, the material properties and process parameters were modified to ensure laminar flow within the glass filament, while attempting to maintain model parameters similar to those that occur near the critical softening temperature of the glass filament.

Once the flow parameters were modified to ensure laminar flow of the molten glass, and the density and viscosity gradients were decreased, Vi^3S-FLOW was able to identified localized regions of filament attenuation and break-up. The utility of Vi^3S-FLOW lies in its ability to characterize the shear air/fiber interaction on a micro-scale. Identifying the specific mechanisms attributed to filament break-up requires additional development on a much more refined scale in order to accurately resolve the break-up phenomenon.

The balance of momentum within the air/fiber system is critical to predicting fiber necking and attenuation. As Test Cases A, B and C indicate, air/glass momentum ratios greater than one ultimately lead to attenuation and necking of the molten glass filament. On the contrary, if the momentum of the glass is greater than that of the air, the glass will dominate the flow and a phenomenon similar to the Kelvin-Helmholtz instability will develop resulting in significant break-up of the VOF data on the mesh.

As the drag force of the fiber was increased the onset of necking and attenuation occurred earlier in the simulation. The increased drag force also produced a more stable interface with little break-up of the VOF data. The increased drag force resulted in small interface perturbations that eventually dissipated over time. The addition of the body force also produced continuous necking, more so than each of the previous simulations. The addition of both the increased drag and body force to the final test case produced a 20% decrease in filament diameter over the length of 10 mm. The air/fiber system showed continuous necking and attenuation over the length of the fiber. Initial surface disturbances arose but dissipated over time. The addition of the drag and body forces may not have been required if the length of fiber simulated could have been increased to match the lengths of fibers produced in industry. The discontinuous glass fibers produced in industry approach 0.05 meters in length and vary in diameter from 5 to 50 microns. The additional length of a 0.05 meter long fiber may have provided the additional surface area resulting in a drag force that was sufficient enough to achieve the degree of necking observed in industry, without the addition of the drag of body forces. On average a discontinuous glass fiber produced in industry experiences a 98 % decrease in diameter over a length of approximately 0.05 meters. The results of the test cases, which include the elevated drag and body forces, predicted an average of 25% decrease in fiber diameter over 10 mm.

The addition of the body force and increase in drag force examined the importance of each on attenuation and necking of the glass filament. The addition of other modules such as these may be required to accurately access filament attenuation, necking and break-up. Although there is a difference between the numerical results obtained from the fiber test cases and the results observed in industry, the numerical model development completed over the course of the research is the most comprehensive and extensive CFD code development completed to date that focuses on the shear air/fiber interaction similar to that occurring in industry. The results represent the first attempt toward a complete characterization of the shear air/fiber interaction of discontinuous fiber manufacturing.

CHAPTER SEVEN

CONCLUSIONS & RECOMMENDATIONS

7.1 Conclusions

As a result of the completed research, the shear air/fiber interaction that occurs during the process of discontinuous glass fiber manufacturing is better understood. An improved understanding of the fundamental mechanism attributed to fiber attenuation has been obtained through the use of detailed experimental drag force measurements and numerical model simulations.

The development of the novel piezoelectric force transducer enabled the drag force to be measured for discrete glass microfibers within a well characterized turbulent air flow. Although the force sensor measured the average drag force of glass fibers ranging from 10 to 50 microns in diameter and 0.2 to 0.4 meters in length, the sensor did not possess sufficient dynamic response or sensitivity to measure the smallest fluctuations in drag force.

The initial examination of the fiber natural frequency, using high-speed video, estimated the fundamental frequency of the fiber to be approximately one half of the natural frequency of the force transducer. However, further examination of the turbulent driving frequency using autocorrelation data and grid scaling estimates, indicated a higher frequency than expected. Given the natural frequency of the force sensor and the higher than expected driving frequency of the system, the frequency ratio (ω/ω_n) approached unity with increasing Reynolds number. The natural frequency of the force transducer could not be increased due to limitations of the piezoelectric film and the etching process. Thus, a dynamic correction factor was implemented which compensated for the large driving frequency and relatively low piezoelectric film frequency. The correction factor did compensate for frequency ratios approaching unity, however it also reduced the sensitivity of the device by collapsing the scatter in the force sensor data for a range of Reynolds numbers and fiber sizes.

The force sensor is suited to adequately measuring the small amplitude fluctuations of the fiber, but as the driving frequency approaches the natural frequency of the force sensor, the amplitude correction factor masks the measurement variations and reduces the data scatter. As a result, the force sensor is capable of measuring average trends of the drag force, but does not possess the desired frequency response or sensitivity to resolve the force differences between fibers of differing diameters, lengths and modulus.

The process of discontinuous glass fiber manufacturing is enormously complex. Only recently have efforts been made to develop two-dimensional, CFD models to simulate the process of fiber formation. Those models, however, neglect the air/fiber interaction, turbulent nature of the process and non-Newtonian behavior of the molten glass. Currently, there exists no commercially available CFD models that addresses these complexities. Developing a CFD code, such as Vi^3S-FLOW, has provided the means to simulate the shear air/fiber interaction which is believed to play a critical role in the attenuation of molten glass filament in rotary spinning processes. The fundamental insight obtained as a result of the numerical simulations has greatly enhanced the understanding of industrial fiberizing, ultimately providing the necessary intuition to improve control of fiber diameter and length during production.

The CFD code Vi^3S-FLOW, based on the one fluid version of RIPPLE, has been developed and tested. The code has simulated process scenarios similar to those that occur in industry. Although Vi^3S-FLOW is not capable of simulating creeping flows, simplifying assumptions were made that enabled the simulation of the shear air/fiber interaction similar to that believed to occur in industry. The CFD model initially included a fully integrated fluid/thermal solver, however Reynolds number restrictions due to elevated viscosities that occur as the glass rapidly cools, required the decoupling of the two modules. Although the fluid and thermal modules were decoupled, due to the non-Newtonian behavior of the glass, each provides valuable information regarding localized fiber attenuation.

Following the extensive numerical modifications detailed in Chapter 5, Vi^3S-FLOW was implemented to simulate several air/fiber test cases. The simulation test cases identified Vi^3S-FLOW's creeping flow limitation. The dependence of fiber necking on the air/fiber momentum ratio was also examined. The results predict fiber attenuation for air/fiber momentum ratios greater than one and a behavior similar to the

Kelvin-Helmholtz instability for air/fiber momentum ratios less than one. The development of the instability at the fluid interface ultimately leads to potential break-up of the filament without noticeable attenuation. The importance of drag and body forces were also examined in the development of the CFD model. Fibers in industry approach 0.05 meters in length while those simulated in the industrial fiber test cases are less than 10 mm. As a result, the addition of elevated drag and body forces were required to produce attenuation of the test case glass filaments. The addition of the drag and body forces may not have been required if fiber lengths similar to those that occur in industry could have been simulated in a reasonable amount of computational run-time. The additional surface area of the 0.05 meter fiber may have provided a sufficient increase in drag and body force to produce necking in the numerical model.

The results of the CFD simulations are the first known models which examine the shear air/fiber interaction on the micro-scale of the fiber. The insight gained from these simulations has provided the background needed to pursue the development of additional, more complex CFD models that will further explore the critical interactions that occur during discontinuous fiber manufacturing. The development and continued improvement of CFD models such as Vi^3S-FLOW is required if the phenomenon of discontinuous fiber spinning is to be well understood.

7.2 Suggestions for Future Research

Although a great deal of valuable information has been gained from the investigation into the process of discontinuous glass fiber manufacturing, the research represents the first step toward achieving a complete understanding of the industrial process and critical interactions that are attributed to fiber attenuation and formation. To fully understand the spinning process, additional numerical models and experimental techniques must be developed.

The experimental techniques that are readily adaptable to the process of fiber spinning are extremely limited. The focus of experimental methods should be devoted to non-intrusive techniques such as laser doppler velocimetry (LDV) to measure fiber size, speed, orientation and possibly fiber strain rates. Simplified, experimental rotary spinners should be constructed that examine the extrusion of several glass filaments rather than the hundreds and thousands of fiber streams that are produced in industrial spinners. High-speed video imaging should be used to gain insight into the extrusion process. Heated wind tunnel experiments should be initiated to examine fiber attenuation and fracture. Process environments should be well characterized by taking temperature and velocity measurements within critical flow regions of the industrial process.

The concurrent development and improvement of Vi^3S-FLOW must be pursued. The focus should remain on the further development of research codes such as Vi^3S-FLOW, allowing the researcher to target specific interactions and process scenarios unlike commercially available CFD codes which are ill-suited for specific research topics. Specific CFD code development objectives should include the following.

- The completion of a comprehensive parametric study that examines the influence of density, viscosity, velocity, temperature and geometric spinner configuration on fiber attenuation and necking.
- The development of improved interface tracking algorithms which minimize interface diffusion in two fluid cases.
- Apply or develop a three-dimensional CFD code to the process of discontinuous fiber spinning. It is likely that critical insight into the complex process of fiber formation exists in the third dimension.
- Improve the CFD code's ability to accurately model larger density and viscosity gradients on the micro-scale of the fiber.
- Investigate adaptive mesh schemes that are able to rapidly adapt to the extreme axial and radial attenuation of the fiber as it occurs in industrial processes.
- Develop a fully integrated fluid/thermal solver that solves both fluid and energy equations in each fluid domain.
- Develop a temperature dependent viscosity module that enables the simulation of creeping flow as the glass temperature reaches the critical softening temperature.
- Optimize Vi^3S-FLOW's data structure to increase CPU run-time efficiency.
- Develop additional modules that characterize the turbulent and break-up mechanism within the fiber spinning process.

Pursuing and implementing suggestions such as those listed above into current CFD code development will enable researchers to simulate the process of discontinuous glass fiber spinning in more detail than ever before. However, a significant amount of experimental and numerical development is required before the fundamental air/fiber interaction is well understood.

REFERENCES

Anderson, J.D. Computational Fluid Dynamics, McGraw-Hill, 1995.

Akatuska, T. and Furumatsu, N., “Modeling and Simulation of Combined Continuous and Discrete Systems: Case study of Spinning Process”, Journal of Chemical Engineering of Japan, Vol. 30, No. 6, p.867, 1997.

Ashgriz, N. and Poo, J.Y., "FLAIR: Flux Line-Segment Model for Advection and Interface Reconstruction". Journal of Computational Physics, Vol. 93, pp.449-468, 1991.

Balci, O., “Principles of Simulation Model Validation, Verification and Testing”, Transactions of the Society for Computer Simulation International, vol. 4, no. 1, pp. 3-12, 1997.

Brackbill, J.U., Kothe, D.B., and Zemach, C. "A Continuum Method for Modeling Surface Tension". Journal of Computational Physics, 100, 335-354, 1992.

Brackbill, J.U. and Saltzman, J.S. “Adaptive Zoning for Singular Problems in Two Dimensions”, Journal of Computational Physics ,vol. 46, pp. 342-368, 1982.

Bruun, B.B., Hot-Wire Anemometry; Principles and Signal Analysis, Oxford University Press, 1995.

Burget, K. M. and Advani, S.G., “An Experimental Investigation of Fiber Motion Near Solid Boundaries,” ASME Fluids Eng. Div., Conference on Liquid-Solid Flows, v. 189, 1994.

Cai, Y., *Personal Communication*, November, 1995, 1997.

Cai, Y., Modeling Fiber Formation by the Spinning Process, Ph.D. Dissertation, Material Science, Colorado School of Mines, July, 1994.

Cai, Y.; Munoz, D.R.; DePorter, G.; and Martin, P., "Modeling Fiber Formation by the Spinning Process", Developments in Non-Newtonian Flows, FED-Vol. 206/AMD-Vol. 191, ASME, pp. 89-96, 1994.

Chandrasekhar, S. Hydrodynamic and Hydromagnetic Instability, Oxford University Press, 1961.

Choudhury, S.R., Jaluria, Y., "Practical Aspects in the Drawing of an Optical Fiber", J. Material Research., vol. 12, no. 2, pp. 483-493, 1998.

Choudhury, S.R., Jaluria, Y., "Thermal Transport due to Material and Gas Flow in a Furnace for Drawing an Optical Fiber", J. Material Research., vol. 13, no. 2, pp. 494-503, 1998.

Choudhury, S.R., Jaluria, Y., Vaskopoulos, T., Polymeropoulos, C.E., "Forced Convective Cooling of Optical Fiber During Drawing Process", Transactions of ASME, vol. 116, pp. 790-794, 1994.

Choudhury, S.R., Jaluria, Y. and Lee, S.H.K., "A Computational Method for Generating the Free Surface Neck-Down Profile for Glass Flow in Optical Fiber Drawing", Nuemrical Heat Transfer, Part A., vol. 35, pp. 1-24, 1999.

Comte-Bellot, G., Corrsion, S., "The use of a contraction to improve the isotropy of grid generated turbulence", J. Fluid Mech., vol. 25, part 4, pp. 657-682, 1966.

Daily, B.J. "Numerical Study of the Effects of Surface Tension on Interface Instability", Physics of Fluids, vol. 12, no. 7, 1969.

Dantec Measurement Technology, Kim Daugberg, President, *Personal Communication*, 1998.

DeBar, R. Fundamentals of the KRAKEN Code, Technical Report UCIR-760, LLNL (1974).

Delplanque, J.P. and Rangel, R.H., "Numerical Simulation of Liquid Jet Overflow in Droplet Deposition Processes", Acta Materialia, vol. 47, pp. 2207-2213, 1999.

Delplanque, J.P., Lavernia, E.J., and Rangel, R.H., "Multi-Directional Solidification Model for the Description of Micro-Pore Formulation in Spray Deposition Processes", Numerical Heat Transfer, Part A:Applicatios, vol.30., pp.1-18, 1996.

Doebelin, E.O., Measurement Systems Application and Design, 4th Edition, McGraw-Hill, Inc., 1990.

DuPont, P. and Morrill, J., Residential Indoor Air Quality and Energy Efficiency. ACE 3 Publishers, Washington, D.C., 1989, p.134.

Eastes, Walter, Editor, Man-Made Vitreous Fibers: Nomenclature, Chemistry and Physical Properties, by the Nomenclature Committee of TIMA Inc., 1993.

Fox, R.W., McDonald, A.T., Introduction to Fluid Mechanics, Wiley and Sons, 1992.

Forest, G.M., Wang, Q. and Bechtel, S.E., "One-Dimensional Isothermal Spinning Models for Liquid Crystalline Polymer Fibers", Journal of Rheology, 41(4), July/August, 1997.

Frota, M.N., Moffat, R.J., "Effects of Combined Roll and Pitch Angles on Triple Hot-Wire Measurements of Mean and Turbulence Structure", DISA Information, pp.15-23, 1981.

Frota, M.N., Moffat, R.J., Honami, S., "Flow Disturbance Induced by the DISA Triaxial Hot-Wire Probe 55P91", DISA Information, pp.24-26, 1981.

Grant, H.L. and Nisbet, C.T., "The inhomogeneity of grid turbulence", J. Fluid Mech., vol. 218, pp. 263-272, 1956.

Gross, Steve (personal communication), Johns Manville, 1997.

Gupta, K.G., Schultz, W.W., Arruda, E.M., and Lu, X., "Nonisothermal Model of Glass Fiber Drawing Stability", Rheol. Acta., vol .35, pp.584-596, 1996.

Harlow, F.H. and Welch, J.E., "Numerical Calculation of Time-Dependent Viscous Incompressible Flow of Fluid with Free Surface", Physics of Fluids, Vol. 8, 1965, pp.2182-2189.

Higuchi, K. and Katsu, T., Sen-I Kikai Gakkaishi, 13, 1 (1960).

Hinze, J. O., Turbulence, McGraw-Hill, 1959.

Hirt, C.W. and Nichols, B.D. "Volume of Fluid (VOF) Method for the Dynamics of Free Boundaries". Journal of Computational Physics, 39, 201-225, 1981.

Hirt, C.W., Cook, J.L. and Butler, T.D., "A Lagrangian Method for Calculating the Dynamics of an Incompressible Fluid with Free Surface", Journal of Computational Physics, Col. 5, 1970, pp.103-24.

Horowitz, P. and Winfield, H., The Art of Electronics, 2nd Edition, Cambridge University Press, 1989.

Incropera, F.R. and DeWitt, D.P., Fundementals of Heat and Mass Transfer, John Wiley and Sons, 1990.

Jenkins, G.M., Watts D.G., Spectral analysis and Its Applications, Holden-Day, San Francisco, 1968.

Johnson, S., Masters Thesis, (in progress), Colorado School of Mines, 2001.

Jorgnesen, F.E., “Directional Sensitivity of Wire and Fibe-film Probes”, DISA Information, pp.31-37, 1970.

Kase, S. and Matsuo, T., Sen-I Kikia Gakkaishi, 18, 188, 1965.

Kershaw, D.S., "The Incomplete Cholesky-Conjugate Method for the Iterative Solution of Systems of Linear Equations". Journal of Computational Physics, 26, 43-65, 1978.

Kistler, A. L., Vrebalovich, T., “Grid turbulence at large Reynolds numbers”, J. Fluid Mech., vol. 26, part 1, pp. 37-47, 1966.

Kothe, D.B, Personal Communication, October 1999.

Kothe, D., Mjolsness, R.C., Torrey, M.,D., RIPPLE: A Computer Program for Incompressible Flows with Free Surfaces (User's Manual), Los Alamos National Laboratory, Los Alamos, New Mexico, 1991.

Kothe, D.B. and Rider, W.J., "Reconstructing Volume Tracking", Journal of Computational Physics, 141, 112-152, 1998.

Libby, P.A., Introduction to Turbulence, Taylor and Francis, 1996.

Lord Rayleigh, Proc. Lond. Math. Soc. 10, 4, 1879.

Mansour, N.G. and Lundgren, T.S., Physics of Fluids, A2, 1141, 1990.

Matsui, M., Trans. Soc. Rheol., 20, 465, (1976).

McLellan, G.W. and Shand, E.B. Glass Engineering Handbook, McGraw-Hill, 1984.

McComb, W.D., The Physics of Fluid Turbulence, Oxford University Press, 1990.

Mohamed, M.S. and LaRue, J.C, "The decay power law in grid generated Turbulence", J. Fluid Mech., vol. 219, pp. 195-214, 1990.

Munson, B.R., Young, D.F., Okiishi, T.H., The Fundamental of Fluid Mechanics, Wiley & Sons, New York, 1990.

Mydlarski, L., Warhaft, Z., "On the onset of high-Reynolds number grid generated wind tunnel turbulence", J. Fluid Mech., vol. 320, pp. 331-368, 1996.

Noh, W.F. and Woodward, P.R., SLIC(simple line interface method), in Lecture Notes on Physics., Vol. 59, p. 330, 1976.

Oberkampf, W.L. and Blottne, F.G., "Issues in Computational Fluid Dynamics Code Verification and Validation", AIAA Journal, vol. 6, no. 5, pp. 687-695, 1998.

Owens Corning Web Site, www.cmog.org, 2000.

Patankar, S.V. Numerical Heat Transfer and Fluid Flow, Hemisphere Publishing Corporation, 1980.

Pelanne, C.M., Neal, J.E., and Filarowicz, D.J., Johns-Manville, "Refractory Products; Heat Flow Principles and Heat Flow Practice," IND-3288, 1981.

Price, G.R., Reader, G.T., Rowe, R.D., and Bugg, J.D., "A Piecewise Parabolic Interface Calculation for Volume Tracking", 1999.

Ridel, V.V. and Il'gamov, M.A., "Non-Linear Waves in an Absolutely Flexible Fiber", Journal of Applied Mechanics and Technical Physics, Vol. 38, No. 6, 1997.

Ross, F.R. and Klingenberg, D.J., "Dynamic Simulation of Flexible Fibers Composed of Linked Rigid Bodies", Chemical Physics, Vol. 107 (7), Feb. 1997.

Rudman, M., "A Volume Tracking Method for Incompressible Multifluid Flows with Large Density Variations", International Journal for Numerical Methods in Fluids, vol. 28, pp. 357-378, 1999.

Sakiadis, B.C., AIChE Journal, vol. 7, p. 467, 1961.

Sakai, Y, Nakamura, I., Sakai, M., and Kushida, T., “An Experimental Study of the Ineraction Between Grid Generated Turbulence and a Two-Dimensional Bluff Body”, JSME International Journal, Series B, v.41, no.1, pp.115-122, 1998.

Schlichting, H., Boundary-Layer Analysis, McGraw-Hill, 1951.

Silverman, L., Billings, C.E., and First, M.W., Particle Size Analysis in Industrial Hygiene, Academic Press, New York, 1971.

Simpkins, P.G. and Blythe, P.A., “Laws for Fiber Temperature Prediction During Drawing”, Transactions of ASME, vol. 119, pp. 652-655, 1997.

Skjetne, P., Ross, R.F. and Klingenberg, D.J., “Simulation of Single Fiber Dynamics”, Journal of Chemical Physics, Vol. 107 (6), Aug. 1997.

Stump, D.M. and Fraser, W.B., “Dynamic Bifurcations of the Ring-Spinning Balloon”, Math. Engng. Ind., Vol. 5, No. 2, pp. 161-186, 1995.

Sussman, P., Smereka, P. and Osher, S., “A Level Set Approach for Computing Solutions to Incompressible Two Phase Flow”, Journal of Computational Physics, vol. 114, pp. 146-159, 1994.

Taylor, G.I., “Statistical Theory of Turbulence”, Proc. Roy. Soc. London A, pp. 151-421, 1935.

Tennekes, H. and Lumley, J.L., A First Course in Turbulence, Massachusetts Institute of Technology Press, 1972.

Tryggvason, G. and Unverdi, D.D., "Computations of Multi-Fluid Flows", Physica D, vol. 60, pp. 70-83, 1992.

Tresso, R., Masters Thesis, Three-Dimensional Statistical and Cross Moment Methods for Identifying and Characterizing Isotropic, Homogeneous Turbulent Flow Regions Downstream of a Square Mesh, Colorado School of Mines, Dec. 1998.

Tresso, R. and Munoz, D., "Homogeneous, Isotropic Flow in Grid Generated Turbulence", J. of Fluids Eng., vol. 122, pp.51-56, March 2000.

Tresso, R. and Munoz, D., “Measurement of Friction Drag Force on Discontinuous Glass and Polymer Fibers”, Review of Scientific Instruments, vol. 71, no. 9, pp.3587-3594, Sept. 2000.

White, F.M., Fluid Mechanics, McGraw-Hill, Inc., 1994.

White, F.M., Viscous Fluid Flow, McGraw-Hill, Inc., 1974.

Wingaard, J.C., "The Effects of Probe-Induced Dlow Distortion on Atmosphereic Turbulence Measurements", Journal of Applied Meterology, v.20, pp784-794, 1981.

Wu, Tien T. and Shambaugh, Robert L., "Characterization of the Melt Blowing Process with Laser Doppler Velocimetry", Ind. Eng. Chem. Res., v.31, pp.379-389, 1992.

Yarin, A.L., Gospodinov, P., Gottieb, O. and Graham, M.D., "Newtonian Glass Fiber Drawing: Chaotic Variation of the Cross Section Radius", American Institute of Physics, vol. 11, no. 11, pp.3201-3208, 1999.

Youngs, D.L., Time dependent multi-material flow with large fluid distortion, in Numerical Methods for Fluid Dynamics, Academic Press, New York, p.273, 1982.

Zahorski, Stefan, Necking in Non-Isothermal High Speed Spinning as a Problem of Sensitivity to External Disturbances", Journal of Non-Newtonian Fluid Mechanics, 63 pp. 33-43, 1996.

Ziabicki, Andrzej, Fundamentals of Fibre Formation, John Wiley and Sons, New York, 1976.

Ziabicki, Andrzej and Kawai, H., High-Speed Fiber Spinning, Krieger Publishing Company, Malabar, Florida, 1991.

Ziabicki, A., Jarecki, L., and Wasiak, A., "Dynamic Modeling of Melt Spinning", Comp. and Theor. Polymer Science, Vol 8, Number ½, 1998.

Ziabicki, A. and Kedzierska, K., Kolloid-Z., 171, 52, 1960.

APPENDIX A

THE NUMERICAL SCHEME

RIPPLE is a program for modeling transient, two-dimensional, incompressible fluid flows with surface tension on free surfaces of general topology. The incompressible Navier-Stokes equations are solved using a finite difference solution on a Eulerian, rectilinear mesh in Cartesian or cylindrical coordinates. A two-dimensional axisymmetric coordinate was selected for this study. Volume-of-fluid (VOF) data on a mesh represents the free surface. Surface tension is modeled as a volume force derived from the continuum surface force (CSF) model. A two-step projection method is used for the incompressible fluid flow solutions, aided by an incomplete Cholesky conjugate gradient (ICCG) solution technique for the pressure Poisson equation (PPE). Momentum advection is estimated with a second order, up-wind method of Van Leer. The following sections succinctly discuss the model equations and numerical methods. Additional details may be found in the work completed by Kothe *et. al.* (1991,1998).

A.1 Governing Equations

RIPPLE's numerical scheme is based on a finite difference solution to a coupled set of partial differential equations that govern all incompressible fluid flows. The basic governing equations of motion are the continuity equation, given as

$$\nabla \cdot \vec{V} = 0 \tag{A.1}$$

and the momentum equations, given as

$$\frac{\partial \vec{V}}{\partial t} + \nabla \cdot (\vec{V}\vec{V}) = -\frac{1}{\rho}\nabla p + \frac{1}{\rho}\nabla \cdot \tau + \vec{g} + \frac{1}{\rho}\vec{F}_b \tag{A.2}$$

where V is the fluid velocity, ρ is the fluid density, p the pressure, τ viscous stress tensor, F_b a body force, and g the acceleration of gravity. The nonlinear advection term ($\nabla \cdot (VV)$) is written in conservative form. In addition to the velocity and pressure, VOF data (i.e. fractional fluid volume defined as F) is used to describe the distribution of fluid in each computational cell. The advection of the VOF data on the mesh along with the velocity field is given as

$$\frac{\partial F}{\partial t} + \nabla \cdot (VF) = 0 \tag{A.3}$$

where F is the scalar quantity referred to as the "color" function, which varies between zero and one.

The viscous stress tensor is given as

$$\tau = 2\mu S \tag{A.4}$$

$$S = \frac{1}{2}\left[\left(\nabla \vec{V}\right) + \left(\nabla \vec{V}\right)^T\right] \tag{A.5}$$

where S is the rate of strain tensor and μ is the coefficient of dynamic viscosity.

Figure A.1 depicts a force balance about an element (dA) at the interface between fluids *a* and *b*.

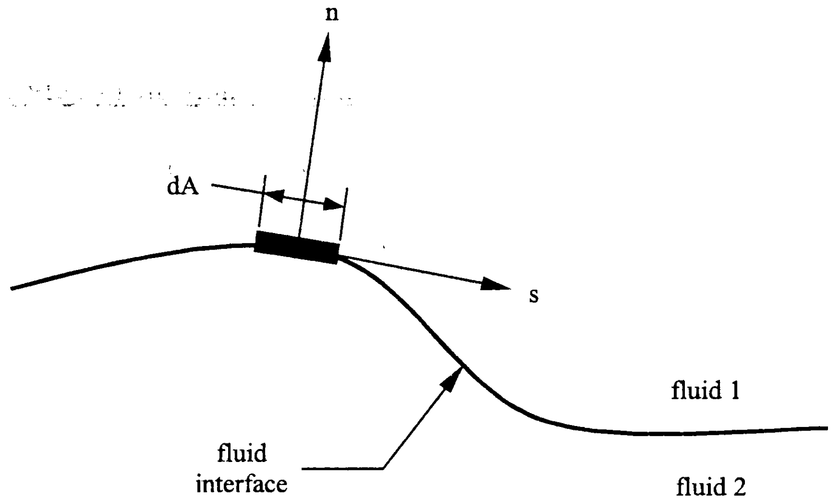

Figure A.1 Force balance about fluid interface element (dA).

Summation of the forces in the normal (n) and tangential (s) directions results in The exact surface stress boundary condition at the fluid free surface written in terms of the normal and tangential boundary conditions is given as

$$\left(\tau_{1,nn} - p_1\right) = \left(\tau_{2,nn} - p_2\right) + \sigma\kappa \tag{A.7}$$

$$\tau_{1,nt} = \tau_{2,nt} + \frac{\partial\sigma}{\partial s} \tag{A.8}$$

where σ is the fluid surface tension coefficient, p is the pressure, n is the unit normal to the surface and κ is the local free surface curvature.

In the original one fluid, RIPPLE source code, viscous effects are neglected in fluid 1 and equation (A.7) and the surface tension coefficient is assumed to be constant which reduces the normal stress boundary condition to Laplace's formula given by

$$p_1 - p_2 = \sigma\kappa \tag{A.9}$$

where the p_1-p_2 is the surface tension induced pressure jump across the fluid interface. A re-formulation of Laplace's equation into a volume force is used in the continuum surface force (CSF) model developed by Brackbill *et. al.* (1992). In the CSF model, surface tension is reformulated as a volume force (body force) given as

$$F_b = \sigma\kappa(\bar{x})\nabla F(\bar{x}) \tag{A.10}$$

A.2 Finite Difference Scheme

RIPPLE implements a 2nd order, central difference approximation of the governing equations based on the Taylor series expansions of the flow variables, which is second order accurate in space and first order accurate in time. The two dimensional fluid domain in RIPPLE is divided into a rectilinear mesh made up of cells with a variable height and width. Each computational cell (see Figure 5.3) is centered at the point (x_i, y_j) and the cell vertices are located at $x_{i+1/2}, y_{j+1/2}$ (top right), $x_{i+1/2}, y_{j-1/2}$ (bottom right), $x_{i-1/2}, y_{j-1/2}$ (bottom left) *and* $x_{i-1/2}, y_{j+1/2}$ (top left). Boundary conditions are applied to a single row of ghost cells that surround the fluid domain. Therefore, the real computational mesh begins with cell (2,2) and ends with the cell (i_{bar+1}, j_{bar+1}) where i_{bar} and j_{bar} are the number of real cells in the x and y directions.

The finite difference method locates x and y velocity components at cell face centers and pressure, density, viscosity and VOF functions at cell centers, as shown in Figure 5.3.

A staggered grid is used to offset pressures, densities, and velocities so that second-order, central differences can be implemented without allowing checker board or "zig-zag" pressure or velocity distributions within the flow field (Anderson, 1995). This also offsets mass and momentum control volumes with the mass control volume centered at the cell center and the x-momentum control volume centered at the cell edge $x_{i+1/2,j}$ also shown in Figure A.2.

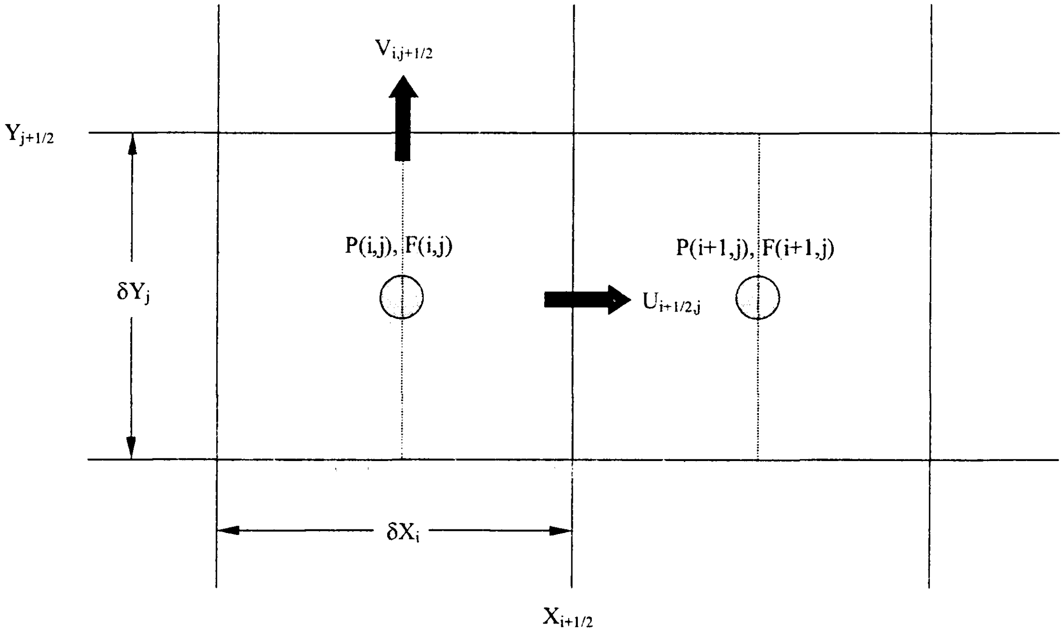

Figure A.2 Computational mesh for cell *(i,j)* and *(i+1,j)*. The x-momentum control volume is shown by a dashed line. Pressure and VOF data are cell centered. The *x* and *y* velocities are located on the vertical and horizontal cell edges, respectively.

An example of the central difference scheme used to discretize the continuity equation is shown below for the continuity equation in two dimensions given as

$$\frac{\partial U}{\partial x}+\frac{\partial V}{\partial x}=0 \tag{A.11}$$

the resulting second order, central difference is given as

$$\frac{U_{i+1,j} - U_{i-1,j}}{2\Delta x} + \frac{V_{i+1,j} - V_{i-1,j}}{2\Delta y} = 0 \qquad \text{(A.12)}$$

A straight forward central difference discretization can be applied to the continuity equation, the same cannot be said for the Navier-Stokes equations, which present a much more formidable task. A central difference scheme is used throughout RIPPLE. The Navier-Stokes equations are characterized as mixed parabolic/elliptic, which results in a mixed implicit/explicit solution with the appropriate stability constraints (i.e. the time step, Δt, must be less than the viscous, Courant or surface tension time step limit) (Patankar, 1980 and Anderson, 1985).

A.3 The Two-Step Projection Method

The numerical solution of the continuity and momentum equations is based on a two-step projection method given by equation A.13 and A.14.

$$\vec{V}^{*} = \vec{V}^{n} + \partial t\left[-\nabla\cdot(\vec{V}\vec{V})^{n} + \frac{1}{\rho^{n}}\nabla\cdot\tau^{n} + \vec{g}^{n} + \frac{1}{\rho^{n}}\vec{F}_{b}^{n}\right] \qquad \text{(A.13)}$$

$$\vec{V}^{n+1} = \vec{V}^* - \frac{\delta t}{\rho^n} \nabla p^{n+1} \qquad \text{(A.14)}$$

$$\nabla \cdot \vec{V}^{n+1} = 0 \qquad \text{(A.15)}$$

In the first step of the two-step projection method, the velocity field is calculated from incremental changes in the current velocity field (V^n) due to advection, gravitational and viscous accelerations and body forces. In the second step, the velocity is projected into a zero divergence vector field. The two equations in the second step are combined into a single pressure Poisson equation (PPE) for the pressure given as

$$\nabla \cdot \left[\frac{1}{\rho^n} \nabla p^{n+1} \right] = \frac{\nabla \cdot \vec{V}^*}{\delta t} \qquad \text{(A.14)}$$

The resulting system of linear equations formulated from the finite difference expressions of the PPE is solved using the incomplete Cholesky conjugate gradient (ICCG) solution technique developed by Kershaw (1977). The ICCG method returns the time t^{n+1} pressure within each cell of the computational domain regardless if the cell represents fluid, void, interface or obstacle.

A.4 Time Integration

The solution method used by RIPPLE to determine the pressure and velocity field at time $n+1$, given all values are known at time n, is summarized in the following steps.

1. Determine (initialize) the position of the fluid interface.
2. Initialize the velocity and pressure fields and set the boundary conditions.
3. Evaluate the surface tension and fluid acceleration due to body forces.
4. Estimate new velocity field based on pressure at previous time step.
5. Solve the pressure Poisson equation (PPE), using the implicit (ICCG) method (see Section 5.1.7 Pressure Poisson Equation).
6. Update the velocity field with the new pressure field.
7. Advect the VOF data.
8. Apply boundary conditions.
9. Begin new cycle.

A.5 Momentum Advection

The non-linear advection term in equation A.2 is written in conservative or divergence form. RIPPLE can approximate the advection term either conservatively $(\nabla\cdot(VV))$ in the body of the fluid and nonconservatively $(V(\nabla\cdot V))$ near the surface or nonconservatively everywhere in the fluid. The method is conservative because the finite control volume used to develop the partial differential or integral equations is fixed in space. In the conservative approximation momentum can only enter or exit the control volume at the boundaries. In short, what goes in must come out. On the contrary, the nonconservative momentum approximation is developed from a control volume that moves with the fluid and implements cell centered flux velocities. The nonconservative estimate is more consistent with the VOF advection algorithm since both use cell face flux velocities to estimate momentum fluxes (see Figure A.2). The conservative momentum advection was implemented in each of the simulations completed during the course of the research.

A.6 Viscous Stress Tensor

The viscous stress tensor in equation 5.2 is given as

$$\nabla \cdot \tau = \left[\frac{1}{r^{\delta}} \frac{\partial}{\partial x} \left(r^{\delta} \tau_{xx} \right) + \frac{\partial \tau_{yx}}{\partial y} \right] i + \left[\frac{1}{r^{\delta}} \frac{\partial}{\partial x} \left(r^{\delta} \tau_{xy} \right) + \frac{\partial \tau_{yy}}{\partial y} \right] j \qquad \text{(A.17)}$$

where δ is a constant equal to 1 in cylindrical geometry and 0 in Cartesian geometry. In RIPPLE the viscous stresses are centered in the momentum control volumes, where τ_{xx} and τ_{yy} are located at cell centers and τ_{xy} is located at cell vertices. The viscous stress tensor is evaluated using the velocity field at the previous time step, thus it is subject to a stability time step constraint.

A.7 Pressure Poisson Equation

In RIPPLE, a two step projection method is used for the incompressible fluid flow solutions, aided by ICCG technique for the pressure Poisson equation (PPE). Recall the PPE equation shown in equation A.18.

$$\nabla \cdot \left[\frac{1}{\rho^n} \nabla p^{n+1} \right] = \frac{\nabla \cdot \vec{V}^*}{\delta t} \qquad \text{(A.18)}$$

The finite difference expression for this equation results in a system of linear equations, which are solved by the implicit ICCG solution technique. The diffusion operator on the left-hand side of equation A.18 is mapped into computational coordinates (ξ, η). A matrix of geometric coefficients is constructed which includes the fluid density in each of the surrounding cells of an *n*-point matrix. RIPPLE uses a 9-point stencil to determine the new pressure field. The ICCG routine uses the geometric coefficients which include computational mesh and fluid density data along with the current pressure field at time t^n to return the time t^{n+1} pressure in each computational cell by matrix inversion. The ICCG routine is a quick and robust method that converges faster than other methods, such as a successive over-relaxation solution. The disadvantage of the ICCG routine is its memory requirements, which increase with the complexity of the geometric coefficient matrix [M] (see section 5.4, equation 5.35). The disadvantage of increased memory is offset by the methods robustness and speed (Kothe *et. al.* 1991). The ICCG method has two advantages over point Gauss-Seidel, alternating direction implicit and over-relaxation methods. The first is that the algorithm is vectorizable with a vector length equal to the full dimension of the system of linear equations. Secondly, it can be applied for any solution of implicitly differenced, partial differential equations. The only restriction is that the matrix to be inverted must be symmetric and positive definite (Kershaw, 1978).

A.8 Free Surface

In RIPPLE the location of the fluid free surface is represented with VOF data on a mesh (Hirt and Nichols, 1981). In the VOF method, specifically the SLIC method used in RIPPLE, an accurate representation of the free surface is not needed. Unlike Lagrangian interface tracking algorithms (i.e. MAC and level set methods) which depend on an accurate reconstruction of the free surface (or interface in the two fluid case), Eulerian interface tracking algorithms (i.e. PLIC and SLIC methods) utilize the free surface to advect the fluid within each computational cell. As a result the Eulerian methods require a less accurate determination of the free surface than Lagrangian methods. The VOF function, *F*, is advected according to

$$\frac{dF}{dt} = \frac{\partial F}{\partial t} + (\vec{V} \cdot \nabla)F = 0 \tag{A.19}$$

In the original version of RIPPLE, *F* is equal to one in the fluid, zero in the void and $0 \leq F \leq 1$ at the free surface. The VOF data provides the only information regarding the free surface. The algorithm currently used is the Simple Linear Interface Calculation (SLIC), whereby vertical or horizontal lines approximate the free surface within a cell based on the appropriate volume fraction of fluid within each particular cell. The surface tension effects are not derived from a reconstruction of the free surface and the CSF model is not dependent on the type of interface reconstruction method. The free surface is only needed to advect the fluid within each computational cell.

A.9 Surface Tension

Surface tension is modeled as a localized volume force using the continuum surface force (CSF) method developed by Brackbill *et. al.* (1992). The interface between two fluids of different properties or "colors" is represented as a transition region of finite thickness, thus negating the need for an accurate reconstruction of a fluid's free surface. The "color" function within this transition region varies continuously. A force density at every point within the transition region is defined from the local free surface curvature of constant "color". The "color" function is nothing more than the VOF weighted average density of the fluid at each point within the computational domain. The utility of the CSF method is that it greatly simplifies the surface tension calculation by eliminating the need to apply a pressure boundary condition to an accurately reconstructed fluid free surface (or interface in the two fluid case). In addition, the CSF method enables accurate modeling of two and three dimensional flows driven by surface forces, and does not place any restrictions on the complexity of the fluid interfaces that have surface tension (Brackbill *et. al.* 1992). The CSF method is easy to implement computationally by calculating and applying an additional body force in the momentum equation. Alternative reconstruction methods suffer from modeling topologically complex interfaces having surface tension, such as Lagrangian interface tracking algorithms that apply pressure boundary conditions to an accurately reconstructed free surface. The CSF method redefines surface tension as a continuous effect across an interface, rather than a boundary value condition on the interface, which can introduce numerical error due to the graininess of the reconstructed interface.

The surface stress boundary condition (both normal and tangential directions) at the fluid free surface (or fluid interface in the two fluid case) are shown in equations A.7 and A.8. In the original RIPPLE, one fluid source code, viscous effects are neglected and the surface tension coefficient is assumed to be constant, thus reducing the stress boundary conditions to Laplace's equation, shown in equation A.9. The resulting pressure jump across the interface is proportional to the surface curvature (κ). In a two fluid case, near the interface, where fluid 1 changes to fluid 2 discontinuously, a continuous transition replaces the pressure jump induced by surface tension. In the CSF model, surface tension contributes a surface pressure that is the normal force per unit interfacial area, which is also equivalent to a volume force given as

$$\lim_{h\to 0}\int_{\Delta V}\vec{F}_{sv}(\vec{x})d^3x = \int_{\Delta S}\vec{F}_{sa}(\vec{x}_s)dS \qquad (A.20)$$

where *h* is the transition region width (see Figure A.3). The area integral is over the length ΔS of the interface surface that lies within the volume of integration ΔV.

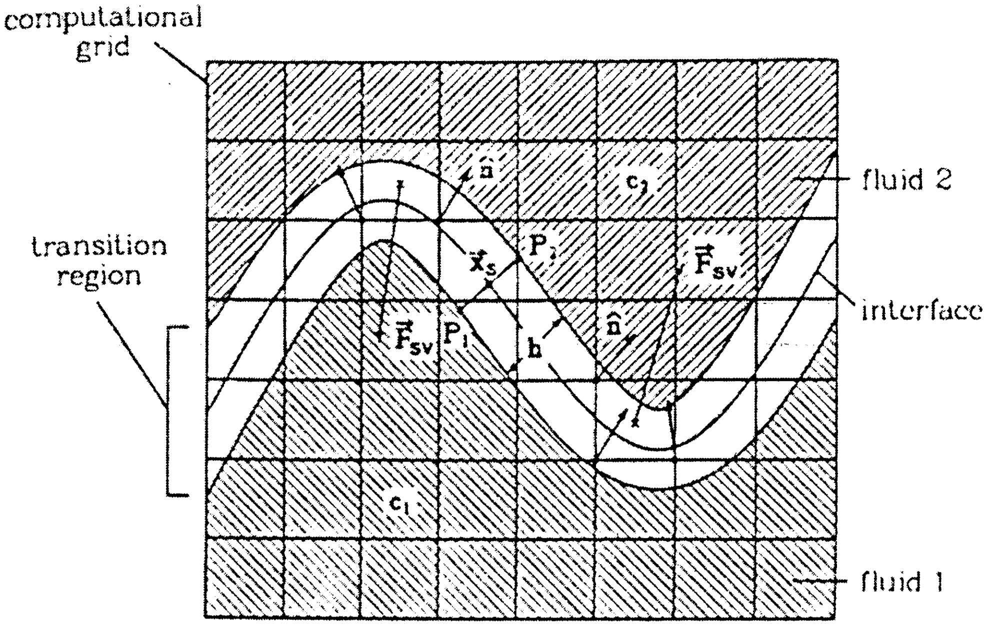

Figure A.3 Transition region between fluids c1 and c2. Interface normals are calculated from $n=\nabla c/|\nabla c|$ at cell vertices within the interface region. Surface tension forces are calculated at cell centers from the divergence of *n* (Brackbill *et. al.*, 1991)

The surface force (shown in equation A.21) is determined using the interface normal (n) calculated at each cell vertex within the transition region.

$$\vec{F}_{sa} = \sigma k(\bar{x})\hat{n}(\bar{x}) \tag{A.21}$$

The surface tension force is nonzero only within the free surface transition region. The interface normal is calculated from gradients of the "color" function. The CSF model places normal vectors at the cell vertices and the curvature (κ) at the cell centers, as shown in Figure A.4. The curvature is determined from divergence of the unit normal

$$\kappa = -(\nabla \cdot \hat{n}) \tag{A.23}$$

where the unit normal is given as

$$\hat{n} = \frac{\vec{n}}{|\vec{n}|} \tag{A.24}$$

and is derived from the unit vector

$$\vec{n} = \nabla F \tag{A.25}$$

which is the gradient of the VOF function.

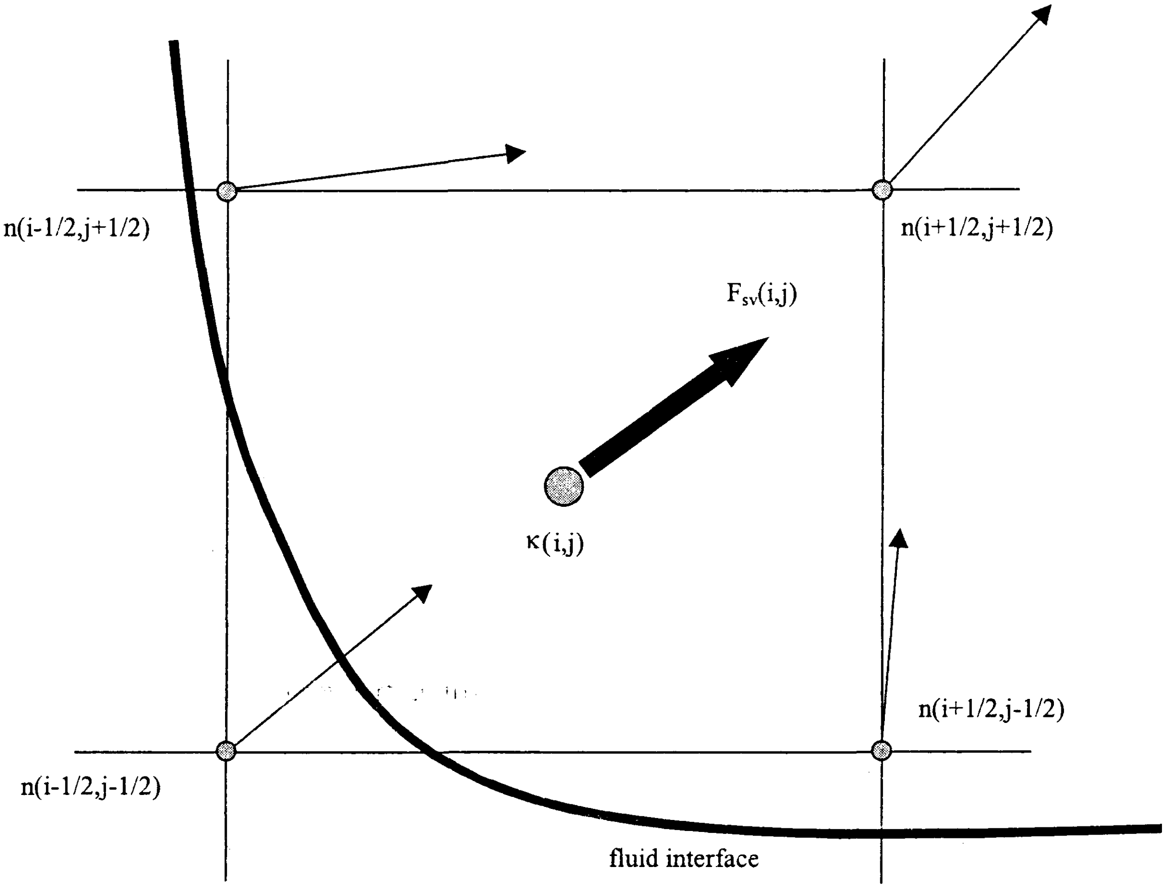

Figure A.4 Determination of the body force derived from the surface curvature (κ) at the cell center and unit normals at the cell vertices.

Thus, surface tension volume force (body force) is calculated at the cell center by taking the gradient of F, given as

$$\vec{F}_{sv} = \sigma k(\bar{x})\nabla F(\bar{x}) \tag{A.26}$$

The volume force is added as a body force to the momentum equation.

The basic equations that govern all incompressible, viscous fluid flow have been presented and briefly discussed in the previous sections. Additional information regarding the implementation and solution of these equations as included in the one fluid version of RIPPLE may be found in Kothe *et. al.* (1991).

APPENDIX B

ERROR ANALYSIS

B.1 Experimental Error

The method of Kline and McClintock (Doebelin, 1990) was used to estimate the uncertainty in the experimentally measured quantities. Table B.1 illustrates the individual components included in the uncertainty analysis.

Table B.1. Uncertainty Analysis Parameters.
Glass Fiber, dia.=27 μm, Length=0.2032 m, Re_d=11.5.

Parameter	Error(Δ)	Units
V (velocity)	0.001	m/sec
L (length)	0.0015	m
d (diameter)	$5.0e^{-7}$	m
ω (frequency)	0.30	Hz
ω_n (nat. frequency)	0.30	Hz
k (stiffness)	$1.0e^{-6}$	N/mm
ζ (damping coeff.)	0.001	dimensionless
A (amplitude)	0.0001	m

Possible sources of error may be attributed to resonant vibration of the airfoil structure and piezoelectric film. Resonance occurs when the measured (or fundamental) frequency of the fiber approaches the natural frequency of the measurement device. The natural frequency of the airfoil structure was measured to be approximately 900 Hz and the natural frequency of the piezoelectric force sensor is approximately 940 Hz. Both natural frequencies are near the fundamental frequency of the turbulent driving force, which may contribute to resonance of the system. Ideally, the natural frequency of the of the force sensor should be at least two to three times the driving frequency of the system.

The effects of temperature on the performance of the piezoelectric film are also of importance in determining potential sources of error and repeatability of the results. Many of the properties of piezoelectric films change with excitation frequency and temperature. There is a small decay in the piezo film strain constant following long-term exposure to elevated temperatures. For example, after 10,000 days at 100°C the strain constant decreases less than 3%. After reaching a stabilizing temperature the material properties remain constant with time and decay only slightly. In the specific application of the dynamic force transducer, the effects of temperature are assumed to be negligible.

B.2 Numerical Error

Throughout each step of the numerical development the model was verified, validated and tested (VV&T) to minimize the effects of numerical error on the final result. Validation is substantiating that a model within its domain acceptably behaves with satisfactory accuracy within the study objectives (Balci, 1997). Model validation is building the right model. Verification transforms a model from a formulation into a model specification, such as converting a flowchart (heuristic) to a computer program

(Balci, 1997). Verification deals with building the model right. Testing demonstrates that inaccuracies exist in the model. The goal of testing is to subject the model to analytical and/or experimental test data to gain agreement between that and the numerical results.

Inherent to all numerical models are the errors associated with modeling continuous quantities (i.e. the partial differential, integral or conservation equations) with discontinuous, discretized approximations. Regardless of the care or method applied in discretizing any continuous model there exists numerical error that is repeatedly generated over the course of a given calculation sequence, from one step to the next. The numerical solution to a set partial differential equations contains two types of errors, discretization and round-off errors (Anderson, 1995). Discretization solution errors are all the errors caused by conversion of the original partial differential, integral or conservation equations representing the physical process to algebraic equations and their computational solution (Oberkampf *et. al.* 1998). A discretization error is the difference between the analytical solution and the numerical approximation of the corresponding difference equation. More simply, the discretization error is the truncation error of the difference equation and any additional error introduced by the boundary conditions. Round-off error is the error introduced after a number of repetitive calculations have been completed to some significant figure, which is determined from the difference between the numerical solution and the exact solution of the difference equation.

Oberkampf *et. al.* (1998) identifies several topics in CFD VV&T that must be considered as fundamental sources of error and inconsistency. The first are physical modeling error, which include the various assumptions used to simplify the formulation of the governing PDE's. Similar attention should be given to the auxiliary physical models, such as the equations of state and thermodynamic properties. Often overlooked sources of error are the application of boundary conditions, which can have a significant impact on the numerical model.

Another common error in all CFD applications and a large contributor to inaccurate numerical solutions are grid resolution errors. The subject of mesh generation in CFD models has plague developers since the inception of CFD in the early 1960's. Mesh generation is often limited by time and financial resources, neither of which encourages the use of mesh sensitivity studies that are often critical factors in CFD development and optimization.

The modified version of RIPPLE was subject to a wide range of test cases following the addition of each module. Although the CFD code was rigorously tested, complete simulation model testing is not possible. The purpose of testing is to increase model confidence and credibility of the numerical results. Balci (1997) provides and summarizes fifteen principles to VV&T all numerical models. However, successfully testing each sub-model does not imply overall model credibility and model credibility can only be claimed for the prescribed condition for which the model was tested (Balci, 1997).

Most CFD solutions address significantly more complex mathematical issues than the analytical methods used in testing the numerical models. In general, the analytical solutions address a much narrower range of fluid dynamics than the computational methods. Thus, special attention must be used when selecting and applying an appropriate test case to verify and validate the numerical model.

Each of the sources of error, as discussed above, has been considered throughout the development of the CFD code RIPPLE. The appropriate test cases have been applied to VV&T the addition of each module to the RIPPLE source code. Both qualitative and quantitative analyses were completed for each test case to ensure numerical agreement with well-founded experimental and analytical data.

APPENDIX C

TWO FLUID PIPE FLOW TEST CASE

A comprehensive characterization of the shear stress interaction occurring at the fluid interface has been attained with the addition of the complete viscous stress tensor and variable viscosity model discussed in Section 5.3. The addition of the modified 9-point pressure template used in the ICCG routine (see Appendix A, section A.7) has also been integrated and provides a more robust method for determining the pressure field over the two fluid domain. A two fluid, laminar pipe flow test case was used to evaluate the viscous stress tensor and PPE modifications. The pipe flow test case was chosen due to its well-founded analytical solution which fully describes the velocity profile of two dissimilar fluids along a pipe cross section (Schlichting, 1951).

The pipe flow test case was modeled using a two-dimensional axisymmetric configuration as shown in Figure C.1. The left axis was the axis of symmetry, with a free-slip boundary condition and the right axis was defined as rigid, no-slip to simulate a wall boundary condition. The top boundary of the computational domain was defined as continuous outflow. At the bottom boundary, an inlet jet provided a continuous source of fluid replenishment of fluids one and two. The inlet velocity of both fluids was identical to avoid the development of a mixing layer. The length of the computational domain was divided in half with fluid 2 on the right and fluid 1 on the left. The dimensions of the domain were chosen appropriately to ensure fully developed laminar flow. The density of each fluid was constant (1000 kg/m^3) with no surface tension or gravity forces present in the simulations. The viscosity of the two fluids was 0.005 m^2/sec and 0.05 m^2/sec. The resulting Reynolds number (Re_d) varied between 12 and 120 for a pipe diameter of 0.4 meters and a length of 5.0 meters. The fully developed length was estimated to be between 0.24 and 2.4 meters depending on the Reynolds number. Initially two viscosity ratios were tested, 1:1 and 10:1, for mesh densities of 10x200, 20x400 and 40x800. In addition to examining the influence of viscosity on fluid motion, a mesh density versus computational run-time comparison was also intended to be completed.

The first simulation was examined the development of the velocity profile for two fluids that possessed identical fluid properties, which is similar to simulating a one fluid pipe flow. The results of a one fluid pipe flow simulation and a two fluid pipe flow simulation with two identical, immiscible fluids should produce similar fully developed, laminar, parabolic velocity profiles. However, the results of the two fluid pipe flow test case were different enough to raise several questions about the development of the two fluid CFD model. The numerical and analytical results of the two fluid pipe flow test case differed by more than 50%.

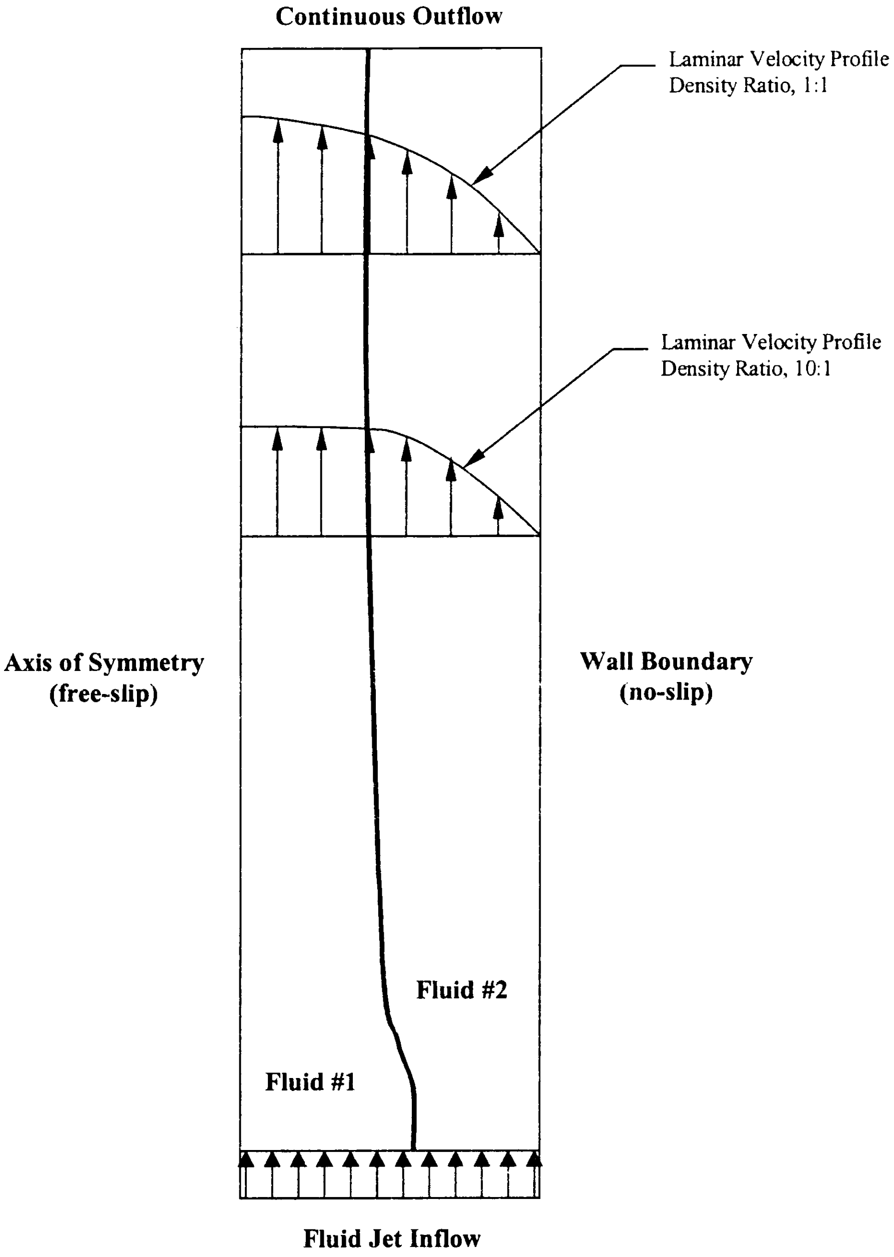

Figure C.1. Illustration of the variable viscosity pipe flow test case.

The results of the two fluid test case show the development of a parabolic velocity profile, due to the no-slip condition on the right wall. However, the velocity magnitude, particularly along the centerline is significantly less than that predicted by the analytical solution, as shown in Figure C.2.

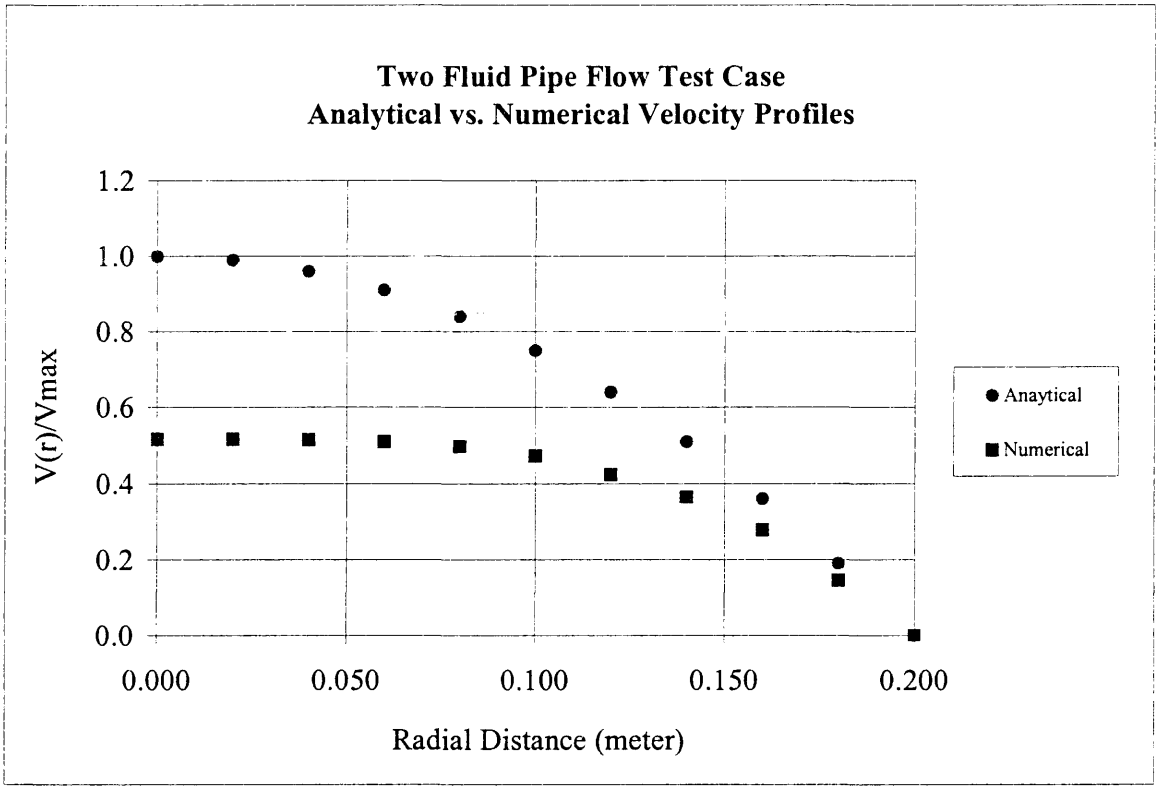

Figure C.2 Analytical vs. numerical velocity profiles.

The resulting numerical data was approximately one half of what was expected from the analytical predication. The numerical profile looks as if the flow may not be fully developed, with the flatness of the curve occurring near the center of the computational domain. However, great care was taken to ensure that the correct input values were specified and that data was recorded within the fully developed flow region. Additional sources of error may be due to a possible overshoot in the velocity profile near the right (no-slip) boundary of the computational domain.

The mesh near the boundary may have also been too coarse to accurately resolve the velocity profile near the wall where the velocity gradients are the largest. Given the cylindrical geometry of the pipe, the mass flow is greater near the wall. Thus, an over-estimate of the velocity profile at this point would result in a decrease in velocity magnitude near the centerline of the pipe due to mass conservation principles. An obstacle in all numerical computations is reconstructing a continuous quantity (in this case the parabolic velocity profile) with a discrete numerical quantity. Regardless of the density of the computational cells, a continuous profile is not attainable as graininess will always exists on the smallest scale. In an attempt to improve the estimate of the velocity profile near the no-slip wall, the mesh density was increased by a factor of four. The simulation results were identical, indicating no difference between the coarse and fine computational grids and the velocity deficit remained near the centerline of the pipe.

In addition to refining the mesh near the boundary, the velocity boundary conditions as well as the implementation of the viscous stress tensor were also re-examined for potential inaccuracies. No obvious sources of error could be found that explain the velocity deficit along the centerline of the pipe.

The velocity deficit and inability to conserve mass are shown in Figure C.3 and C.4. Figure C.3 depicts the velocity profile downstream of the pipe inlet taken at a given instant in time. The fully developed region has not been reached, but the loss of mass occurs soon after the flow has entered the pipe. At each axial position, the mass flow was determined and is summarized in Figure C.4. Ideally the slope of the line in Figure C.4 should be zero (i.e. indicating conservation of mass).

Evident from the simulation results, as the flow of the two fluids progresses from the pipe entrance, the fluid along the centerline begins to expand as if being pulled toward the right (no-slip) wall boundary, eventually causing the flow to plug.

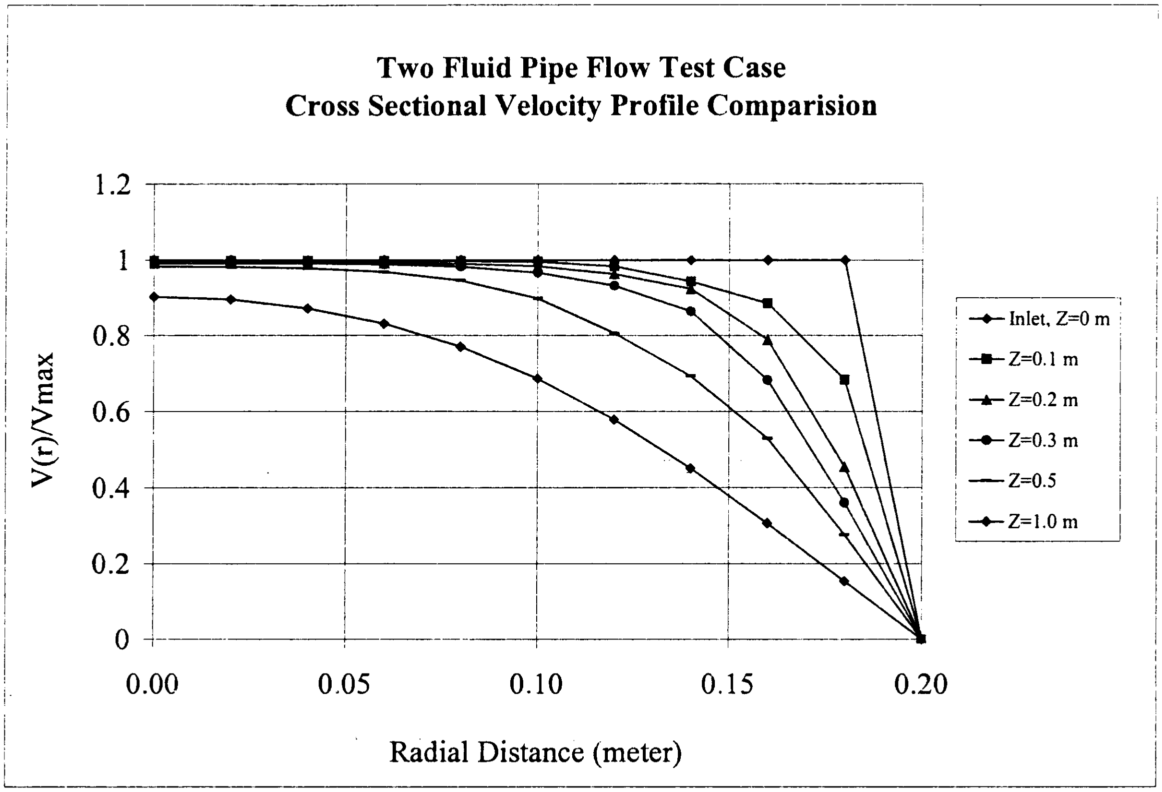

Figure C.3 Two fluid velocity profile results. Fluid properties are identical, interface occurs at r=0.10 meter.

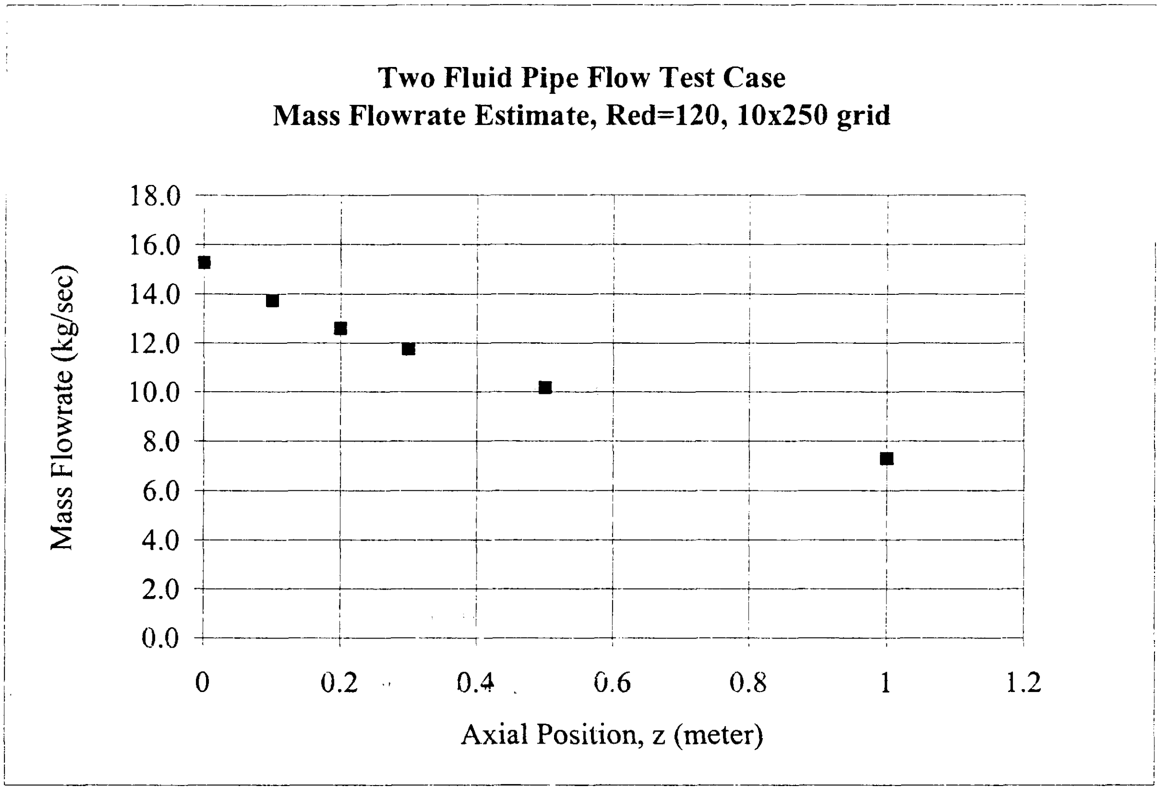

Figure C.4 Two fluid pipe flow mass flowrate summary.

One final check was made to verify that the problem could not be attributed to the addition of the second fluid. The original, one fluid, RIPPLE code was used to simulate a one fluid pipe flow problem identical to that described above. The result is shown in Figure C.5. As expected the numerical results are in good agreement with the analytical predictions. Once the results of the one fluid test case were examined, it was determined that the addition of the second fluid to the code or the boundary conditions associated with a no-slip condition at the pipe wall may be the source of the discrepancy.

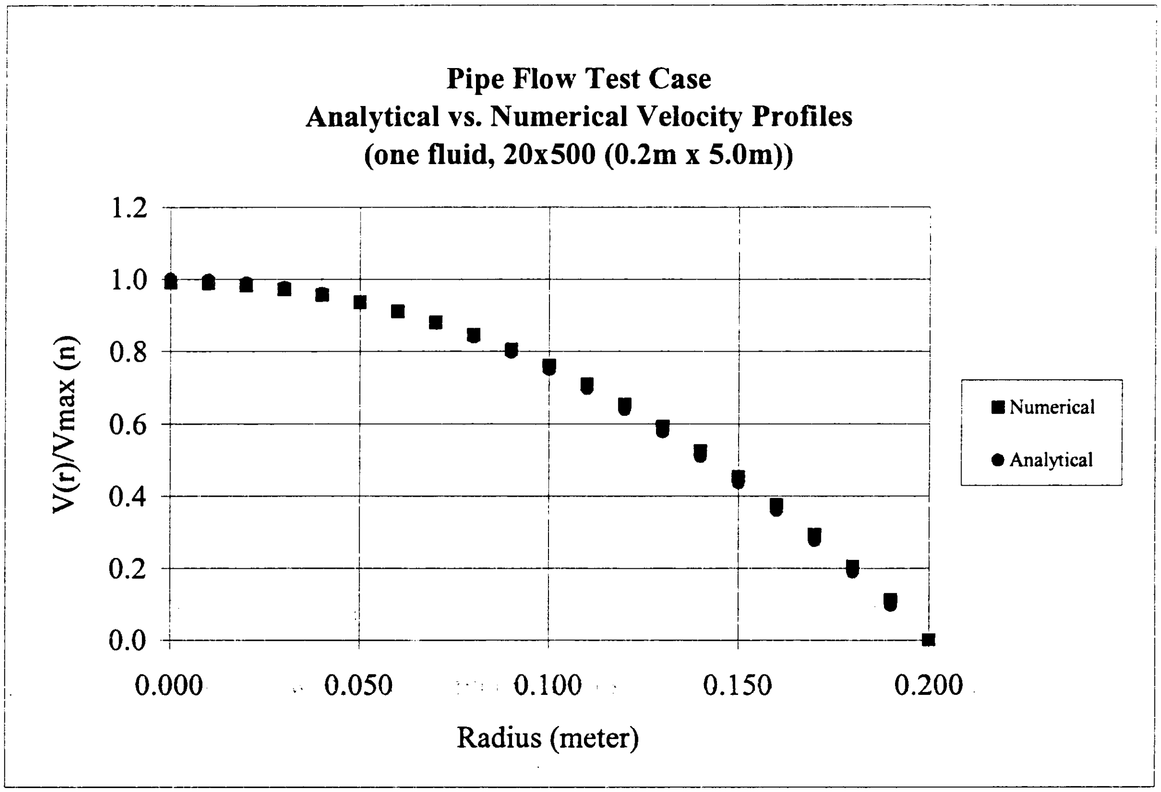

Figure C.5 One fluid pipe flow test case velocity profile comparison.